NUMERICAL STUDIES OF NONLINEAR SCHRÖDINGER AND KLEIN-GORDON SYSTEMS: TECHNIQUES AND APPLICATIONS

by

DAE-IL CHOI, B.S.

DISSERTATION

Presented to the Faculty of the Graduate School of

The University of Texas at Austin

in Partial Fulfillment

of the Requirements

for the Degree of

DOCTOR OF PHILOSOPHY

THE UNIVERSITY OF TEXAS AT AUSTIN

December 1998

NUMERICAL STUDIES OF NONLINEAR SCHRÖDINGER AND KLEIN-GORDON SYSTEMS: TECHNIQUES AND APPLICATIONS

APPROVED BY
DISSERTATION COMMITTEE:

Supervisor: _____

_____

_____

_____

_____

To my mother, Moonhee Chung and my father, Myung Choi

Acknowledgements

First of all, I would like to thank my thesis advisor, Matt Choptuik, for all his guidance and encouragement. I am grateful for all the discussions and advice on numerical aspects of this dissertation.

I would also like to thank Richard Matzner for all his support. It was he who gave me a chance to join the Center for Relativity and start learning General Relativity.

I would like to thank my collaborators, Qian Niu, Will Chism, and Linda Reichl, for many helpful discussions.

I also wish to thank the members of the Center for all their support and helpful discussions, and in particular, Mijan Huq for many useful discussions.

Special thanks to Dr. Takeshi Udagawa for all his support while I was preparing for a qualifier under his guidance.

I also wish to thank my friends for all their support and friendship.

Finally, I thank my parents and my sister for all their love, encouragement and support.

Soli Deo Gloria

NUMERICAL STUDIES OF NONLINEAR SCHRÖDINGER AND

KLEIN-GORDON SYSTEMS: TECHNIQUES AND APPLICATIONS

Publication No. _____

Dae-Il Choi, Ph.D.
The University of Texas at Austin, 1998

Supervisor: Matthew W. Choptuik

The continuing proliferation of computational resources makes it more and more powerful to conduct numerical studies on physics problems for which either analytic methods fail, or well-controlled experiments are very difficult, if not impossible. In particular, a finite-difference based numerical approach has been an indispensable tool in the three areas of physics that I study in this thesis: numerical relativity (boson stars), Bose-Einstein condensates, and atomic hydrogen in strong laser fields.

Numerical relativity (NR) enables us to tackle problems of astrophysical interest which are difficult or impossible to study using analytic methods. Many of these problems involve strong and dynamical gravitational fields, and many involve the dynamics of one or more gravitationally compact objects such as black holes, neutron stars or, more speculatively, boson stars. A long term goal of NR, then (and of this research) is the accurate simulation of the dynamics of one or more compact objects. Here, as a step in that direction, I present some of the first results for a fully coupled Einstein/Klein-Gordon system in 3D, wherein I attempt to evolve a static relativistic boson star using the full equations of motion.

A key motivation for the study of self-gravitating bosonic matter (in both the Newtonian and Einsteinian regimes) is the observation that, even though any direct physical relevance has yet to be demonstrated, boson star systems provide excellent numerical laboratories in which to develop techniques for NR. Specifically, the boson star model provides an ideal vehicle with which to implement and evaluate (1) various coordinate conditions in the context of the ADM formalism and (2) multi-dimensional adaptive mesh refinement techniques which appear crucial for many problems in 3D numerical relativity. Again, as a step towards studying the fully relativistic problem, I first consider boson stars in the Newtonian

regime, which are described by the solutions of Schrödinger-Poisson equations. In particular, I study the dynamics of stationary stars, stars with linear momentum, and binary star systems.

The recent discovery of Bose-Einstein condensates (BEC) in dilute atomic gases has led to renewed experimental and theoretical interest in the study of quantum degenerate gases. These condensates provide a new testing ground for atomic and many-body physics, and there are many unanswered questions in this emerging field. I present methods for manipulating the condensates by an optical lattice generated by laser light and study the effect of atomic interaction on the quantum transport properties. I also study Bloch oscillations and Landau-Zener tunnelings in an accelerating optical lattice.

The study of hydrogen atoms interacting with ultra-intense laser light in the non-perturbative regime has gained attention as a surprising new phenomena in nonlinear atomic physics. Particularly noteworthy are high harmonic generation (HHG) and stabilization, which provide interesting new physics. I use a 2D model to study stabilization behavior for an arbitrary polarization. As a first step, I studied circular and linear laser polarizations. In the circular case, I found spiral wave functions with strong stabilization. In the linear case, I found dichotomous wave functions with weaker stabilization. I have also observed the related HHG signatures.

Finally, adaptive mesh refinement (AMR) techniques are crucial for the numerical solution of problems which have large dynamical range. I present results from the implementation and testing of some general algorithms for use in AMR work, including 2D and 3D clustering routines.

Table of Contents

List of Tables

List of Figures

Chapter 1

Introduction

In this thesis, I discuss numerical solutions of the Schrödinger-Poisson equation and the Einstein-Klein-Gordon equation.

The Schrödinger-Poisson equation is given by

$$i\hbar\frac{\partial\phi(\mathbf{x},t)}{\partial t} = -\frac{\hbar^2}{2m}\nabla^2\phi(\mathbf{x},t) + mc^2V(\mathbf{x},t)\phi(\mathbf{x},t) \tag{1.1}$$

$$\nabla^2 V(\mathbf{x},t) = 4\pi G(\frac{m}{\hbar c})^2\phi(\mathbf{x},t)\phi^*(\mathbf{x},t) \tag{1.2}$$

where ϕ is a complex scalar field, V is a Newtonian potential, and m is the mass of the scalar field.

The Schrödinger equation is the fundamental equation of motion for quamtum mechanics and has been one of the most celebrated and successful equations in the history of modern physics. Even if there are some limitations, such as the facts that the equation holds only in the nonrelativistic limit and that generic solutions are prohibitively difficult to obtain for many body systems, it has been the most important equation for many physicists, chemists and engineers.

Analytic solutions of the equation have been successful in explaining many physical phenomena such as atomic energy levels, scattering problems, and atom-light interaction–all of which are well documented in most standard quantum mechanics textbooks [1]. However analytic solutions have generally been limited to special geometries, or to perturbative, linear and/or time-independent situations. Therefore, many interesting nonperturbative, nonlinear or time-dependent problems have been left out of active research efforts. With the increasing power of supercomputers and supporting resources, numerical studies became an alternative approach which holds strong promise to unlock still-hidden secrets of quantum mechanics.

In principle, the Schrödinger equation can be applied to any quantum mechanical system. However, the numerical approach I take is also useful for a larger class of problems which have *Schrödinger-like* equation of motions, but may not necessarily be truly quantum-mechanical. I am particularly interested in dynamic, nonperturbative and nonlinear problems

such as the nature of Newtonian boson stars, stabilization in 2D hydrogen atoms, Bose-Einstein condensation, simulation of quantum devices, plasma physics, pattern formation and nonlinear optics. Here, I present results from numerical studies of Newtonian boson stars, Bose-Einstein condensates, and the interaction of atomic hydrogen with ultra-intense laser fields. In all cases, I solve the Schrödinger equation directly using a finite-difference method.

The Einstein-Klein-Gordon (EKG) system is given by

$$G_{\mu\nu} = 8\pi T_{\mu\nu} \tag{1.3}$$

$$g^{\mu\nu}\phi_{;\mu\nu} - m^2\phi - \lambda|\phi|^2\phi = 0 \tag{1.4}$$

where the stress energy tensor $T^{\mu\nu}$ for the massive complex scalar field, ϕ, is

$$T^{\mu\nu} = \frac{1}{2}(\phi^{*,\mu}\phi^{,\nu} + \phi^{,\mu}\phi^{*,\nu}) - \frac{1}{2}g^{\mu\nu}(\phi^*_{,\lambda}\phi^{,\lambda} + m^2|\phi|^2 + \frac{\lambda}{2}|\phi|^4) \tag{1.5}$$

Here, m and λ are the scalar field mass and self-interaction coupling constants, respectively. (I use Planck units, $G = \hbar = c = 1$ throughout the thesis). Stationary solutions of the EKG equation describe boson stars in the context of Einstein's theory of General Relativity (GR). My goal is to develop a stable full 3D GR code that can handle boson stars for a long time. GR boson star systems can be used to study generic dynamics of strong gravitational fields. For example, rapidly spinning boson stars with self-interactions may have astrophysical relevance, and a binary star system can be used for the study of gravitational waves.

Unfortunately, there are some unsolved problems which hamper progress towards a stable evolution of relativistic boson stars. One of these problems involves the specification of coordinate conditions which, in the context of the "3+1" formalism in which I work, are described by a lapse function, α, and a shift vector, β^i. In GR, coordinate systems themselves can be strongly coupled to the dynamics of the gravitational field. Bad choices of coordinates will result in the development of coordinate singularities, and such singularities will eventually (and usually quickly) "crash" a simulation. In particular, a suitable coordinate condition for binary star systems is still a topic of much debate. As a first step towards the solution of this coordinate problem (and following work by Balakrishna *et al* [64]), I have implemented and tested the maximal slicing condition for the lapse function. Other coordinate conditions will be tested in the future.

Another current stumbling block in 3D numerical relativity is the treatment of outer boundaries. In the "3+1" Cauchy problem, computational grids do not stretch out to infinity. Therefore, even though there are no physical boundary conditions at the edge of the *finite* computational domain, some kind of special conditions will necessarily need to be imposed there. This is a decidedly non-trivial problem, and currently my evolutions seem at least partly limited by instabilities arising around the outer boundary.

The outline for this dissertation is as follows:

In Chapter 2, I begin with theoretical matters and briefly discuss the "3+1" Arnott-Deser-Misner(ADM) formalism [2].

In Chapter 3, I go over some of the finite-difference numerical techniques I have developed and used [3], and discuss my treatment of boundary conditions. I have used two updating schemes for the Schrödinger equation; an Alternating Direction Implicit (ADI) method [3] and a Multigrid (MG) method [4, 5, 6]. Multigrid is also used to solve the elliptic Poisson equation in my studies of Newtonian boson stars. Following Guenther [118], an annihilation boundary condition is implemented for the Schrödinger equation. This condition damps out all frequency components in an attempt to minimize unphysical reflections off the boundary of the computational domain.

In Chapter 4, I give a brief introduction to boson stars [7, 8, 9, 10, 11, 12, 13, 14, 15, 16, 17, 18, 19, 20, 21, 22, 23, 24, 25] and present results for Newtonian boson stars. To set up initial conditions, I impose a spherically-symmetric, stationary *ansatz*, then solve the resulting ordinary differential equations (ODEs). This data can then be interpolated to a 3D domain on which the evolution is carried out. Results for a single stationary star, a single moving star, and binary star systems are presented.

In Chapter 5, I discuss the initial value problems (IVP), coordinate conditions, boundary conditions in GR. For a single stationary boson star, IVP reduces a set of ODEs as in Newtonian case using the 1D spherical grids. For more general situations, solutions of the full 3D constraint equations are necessary. Then I present some preliminary results for a single stationary star.

In Chapter 6, I give brief introductions to Bose-Einstein condensates (BEC) [69, 70, 71], optical lattices [82], and nonlinear Schrödinger equations. The manipulation of a BEC using optical lattices is demonstrated. I show how to boost a stationary condensate into motion or stop a moving condensate. I observe Bloch oscillations and Landau-Zener tunnelings of the condensate in an accelerating optical lattice. I show how atomic interactions affect these processes and discuss conditions for possible experimental realization.

In Chapter 7, I review the "soft-core" atomic model [116] and discuss the equation of motion for hydrogen atoms interacting with ultra-intense laser light. I use a 2D model problem which includes arbitrary laser polarizations and allows transverse diffusion of the wavefunction. I present results for circular and linear laser polarizations. I observe stabilization and related High Harmonic Generations (HHG).

In Chapter 8, I review the Berger and Oliger [121] Adaptive Mesh Refinement (AMR) scheme and discuss regridding procedure and clustering algorithms in some detail. I also review Choptuik's shadow hierarchy scheme [126] for truncation error estimation.

Finally, in Chapter 9, I conclude and discuss a few directions for further work.

Chapter 2

Theoretical Framework

2.1 Schrödinger Equation

The Schrödinger equation can be derived from the classical energy momentum relation,

$$E = \frac{p^2}{2m} + V \tag{2.1}$$

through the formal transformation:

$$E \to i\hbar \frac{\partial}{\partial t} \tag{2.2}$$

$$p_i \to -i\hbar \frac{\partial}{\partial x_i} \tag{2.3}$$

For the non-relativistic case of the motion of a particle of mass m in a potential field $V(r)$, the Schrödinger equation can be written in the form

$$i\hbar \frac{\partial \phi}{\partial t} = -\frac{\hbar^2}{2m} \nabla^2 \phi + V\phi \tag{2.4}$$

As is well-known, free particle solutions ($V = 0$) of this equation are given by spreading wavepackets. In general though, the potential field V can be function of time, t, and space, x, y, z. In the case of Newtonian boson stars (see Chapter 4), V is a solution of a Poisson equation which has a $\phi-$dependent source (i.e. there is a gravitationally-induced non-linearity). For Bose-Einstein condensates, V has contributions from an external trap potential, self-interactions, and spatially periodic functions from optical lattices. Finally, in the case of atom-laser interactions, V is an explicitly time-dependent function. In all cases, I solve Eq (2.4) using numerical techniques which are discussed in Chapter 3.

A typical boundary condition for a closed quantum system is that the potential at the edge of the domain is infinite. In practice, this condition is usually implemented by demanding that $\phi = 0$ on the boundary.

For open systems, there are no *physical* boundary conditions at the edge of the computational domain. Nonetheless, a certain boundary condition has to be imposed in

any simulation. In this thesis, I use a variety of such conditions on the Schrödinger fields I evolve. These include: an *annihilation* condition, periodicity (no boundary conditions), and *outgoing radiation* conditions. The annihilation boundary condition [118] is similar to the usual absorbing boundary condition [37]. It applies to situations where the system is isolated and incoming waves are not expected. It works by damping out all frequency components of the wavefunction around the computational boundaries. More details are given in Chapter 3

2.2 Klein-Gordon Equation

The Klein-Gordon equation for a massive scalar field with mass m is

$$g^{\mu\nu}\phi_{;\mu\nu} - m^2\phi - \lambda|\phi|^2\phi = 0 \tag{2.5}$$

where λ is a self-interaction coupling constant.

The corresponding stress energy tensor, $T^{\mu\nu}$, is given by

$$T^{\mu\nu} = \frac{1}{2}(\phi^{*,\mu}\phi^{,\nu} + \phi^{,\mu}\phi^{*,\nu}) - \frac{1}{2}g^{\mu\nu}(\phi^*_{,\lambda}\phi^{,\lambda} + m^2|\phi|^2 + \frac{\lambda}{2}|\phi|^4) \tag{2.6}$$

and the Lagrangian is

$$L = \left[\frac{R}{16\pi G} - \frac{1}{2}\left(g^{\mu\nu}\partial_\mu\phi^*\partial_\nu\phi + m^2\phi^*\phi + \lambda(\phi^*\phi)^2\right)\right] \tag{2.7}$$

One can obtain the Klein-Gordon equation by a variation of the action,

$$I = \int d^4x\sqrt{-g}L \tag{2.8}$$

with respect to ϕ^*.

Another way to derive Klein-Gordon equation (without considering gravitation) is by using the (special) relativistic energy momentum relation, $E^2 = p^2 + m^2$. Specifically, one gets the KG equation through the formal transformation,

$$E \to i\hbar\frac{\partial}{\partial t} \tag{2.9}$$

$$p_i \to -i\hbar\frac{\partial}{\partial x_i} \tag{2.10}$$

As in the Schrödinger equation, a boundary conditions are needed for the simulation of both open and isolated systems. In the weak gravitational-field and high frequency limit, the characteristic speed of the equation asymptotes to 1 and the metric, $g_{\mu\nu} \sim 1$. Therefore, if the edges of a computation grid are put far away from the central region where the matter

is distributed, an outgoing radiation boundary condition (wherein the field is assumed to be massless) provides fairly good results. Specifically, we have

$$(r\phi)_{,t} + (r\phi)_{,r} = 0 \tag{2.11}$$

In a 3D cartesian coordinate system, we can reexpress this last condition as

$$x\phi_{,t} + \frac{x}{r}\phi + r\phi_{,x} = 0 \tag{2.12}$$

$$y\phi_{,t} + \frac{y}{r}\phi + r\phi_{,y} = 0 \tag{2.13}$$

$$z\phi_{,t} + \frac{z}{r}\phi + r\phi_{,z} = 0 \tag{2.14}$$

2.3   Einstein Equation: ADM formalism

The Einstein equation for a massive complex scalar field is given by

$$R_{\mu\nu} - \frac{1}{2}g_{\mu\nu}R = 8\pi G T_{\mu\nu} \tag{2.15}$$

$$T_{\mu\nu} = \frac{1}{2}\left(\phi^*_{,\mu}\phi_{,\nu} + \phi_{,\mu}\phi^*_{,\nu} - g_{\mu\nu}(g^{\alpha\beta}\phi^*_{,\alpha}\phi_{,\beta} + m^2|\phi|^2)\right) \tag{2.16}$$

In general relativity, the spacetime structure is represented by a 4-dimensional differentiable manifold M endowed with a 4-metric ${}^{(4)}g_{\mu\nu}$. Even if there are no *a priori* preferred ways to view spacetime, it is helpful to consider a spacetime as a foliation of spacelike hypersurfaces. This allows us to cast the problem as a general relativistic Cauchy problem and helps manifest the dynamical nature of the gravitational field. Here I adopt the "3+1" decomposition or ADM formalism [2, 26] named after Arnowitt, Deser, and Misner who first worked out the approach.

In the "3+1" ADM formalism, a spacetime is sliced into a stack of Cauchy surfaces (spacelike hypersurfaces), Σ_τ, parameterized by a time variable, τ. τ is defined through a vector field t^μ on M which satisfies $t^\mu\nabla_\mu\tau = 1$. Let n^μ be the unit normal vector field to the hypersurfaces Σ_τ. Then the spacetime metric, ${}^{(4)}g_{\mu\nu}$, induces a spatial metric $g_{ij} = {}^{(4)}g_{ij} + n_i n_j$ on the spacelike hypersurfaces. One decomposes t^μ into pieces normal and tangential to Σ_τ by defining the lapse function, α, and the shift vector, βi, with respect to t^μ by

$$\alpha = -t^\mu n_\mu = (n^\mu\nabla_\mu\tau)^{-1} \tag{2.17}$$

$$\beta_i = h_{ij}t^j \tag{2.18}$$

t^μ is then given by $\alpha n^\mu + \beta^i$ as in Fig. 2.1.

The lapse, α encodes the proper time measured by a freely falling observer who is moving orthogonally to the hypersurface. β^i describes the "shift" in spatial coordinates from Σ_τ to a nearby hypersurface, relative to normal propagation.
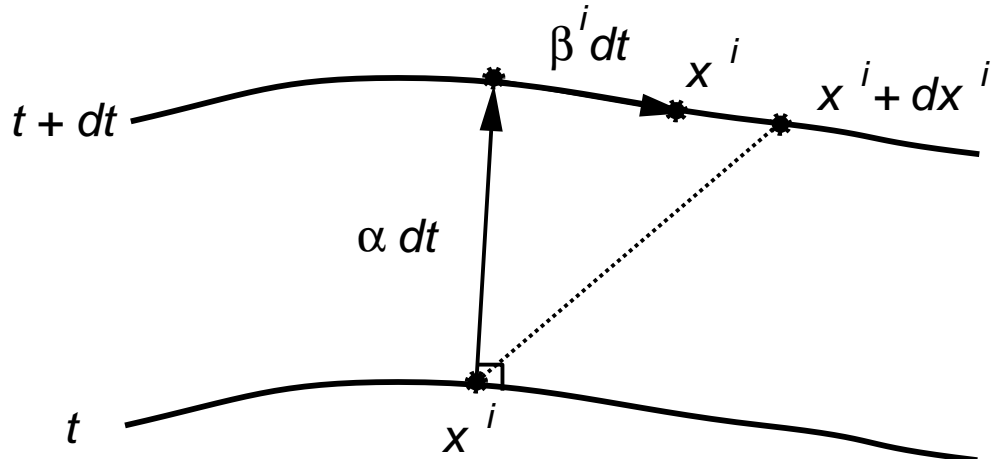
Figure 2.1: This figure shows two spacelike hypersurfaces at time t and $t + dt$. αdt is the proper time measured between the two slices by a freely falling observer who travels along the timelike *normal* vector. β^i is the shift vector and represents the *spatial* coordinate transformation between the two slices. $\alpha n^\mu + \beta^i$ is the tangent-vector (four-velocity) of a coordinate-stationary observer.

Given the foliation of a spacetime, one must identify appropriate dynamical variables which completely characterize a single slice and the way it is embedded in 4-spacetime. Once these dynamical variables are specified on some initial hypersurface, the Einstein equation yields the time development of the corresponding variables on future hypersurfaces. In the ADM formalism, the 3-metric and extrinsic curvature, g_{ij}, K_{ij} constitute an appropriate set of variables. g_{ij} is simply the intrinsic 3-metric of the hypersurface, whereas K_{ij} describes how the hypersurface is embedded in the 4-spacetime. One definition of the extrinsic curvature is

$$K_{ij} = K_{ji} = -\nabla_j n_i \tag{2.19}$$

It can be shown that Eqn. (2.19) implies

$$K_{ij} = -\frac{1}{2}\mathcal{L}_n g_{ij} \tag{2.20}$$

where $\mathcal{L}_n g_{ij}$ is the Lie derivative of the 3-metric along the time-like normals. This also clearly shows that the extrinsic curvature is the rate of change of the 3-metric in time; that is, K_{ij} may be viewed as a "velocity" of the 3-metric.

The detailed derivation of Einstein equation in ADM formalism will not be repeated here since the calculation is well documented in [26, 27]. In the ADM formalism the Einstein equation splits into 4 constraint equations and 12 first order (in time) evolution equations. The constraint equations do not contain second time derivatives of the metric and must

be satisfied by the geometric and matter variables on every hypersurface. They are the Hamiltonian constraint equation

$$R + K^2 - K_{ij}K^{ij} = 16\pi\rho \tag{2.21}$$

and the momentum constraint equation

$$D^i K_{ij} - D_i K = 8\pi j_i \tag{2.22}$$

where D_i is a covariant derivative within a hypersurface. Here I have introduced various projections of the stress tensor which are useful in the ADM formalism:

$$\rho \equiv n_\mu n_\nu T^{\mu\nu} \tag{2.23}$$

$$j_i \equiv g_{ik} j^k \equiv -n_\mu T_i^\mu \tag{2.24}$$

$$S_{ij} \equiv T_{ij} \tag{2.25}$$

ρ is the energy density, j_i the 3-momentum density, and S_{ij} spatial stress tensor *as measured by observers moving orthogonally to the hypersurfaces.*

In addition to the constraints, there are 12 first-order-in-time equations of evolution for the metric, g_{ij}, and the extrinsic curvature, K_{ij}.

$$\partial_t g_{ij} = -2\alpha K_{ij} + D_i \beta_j + D_j \beta_i \tag{2.26}$$

$$\partial_t K_{ij} = -D^i D_i \alpha + \alpha(R_{ij} + K K_{ij} - 2K_{il}K^l{}_j) + \mathcal{L}_\beta K_{ij}$$
$$-8\pi\alpha(S_{ij} - \frac{1}{2}g_{ij}(S - \rho)) \tag{2.27}$$

where $\mathcal{L}_\beta K_{ij}$ is the Lie derivative of the K_{ij} along β^i.

The basic strategy for ADM formalism is as follows. First, an initial hypersurface is chosen and a spatial coordinate system on that initial hypersurface is specified. Then the initial data for $g_{ij}, K_{ij}, \rho, j_i$ is determined by solving the constraint equations with appropriate matter sources. Most multi-dimensional numerical relativity codes use York's conformal formalism [28, 29] to construct initial data. A more detailed discussion of this topic is given in Chapter 5.

Once the initial data is set, the evolution equations are used to evolve data from one slice to the next. This requires the specification of coordinate conditions via a lapse function, α, and a shift vector, β^i. In this thesis, I use the maximal slicing condition

$$K = 0 = \frac{\partial K}{\partial t} \tag{2.28}$$

to fix α, and I set $\beta^i = 0$ (normal spatial coordinates). More details can be found in Chapter 5. Given α and β^i it is, in principle, a straightforward matter to evolve the geometrical variables, g_{ij}, K_{ij} using Eqn (2.26) and (2.27).

Before I close this chapter, I would like to mention a recent preprint that came out while I was preparing this dissertation. Following Shibata and Nakamura [31], Baumgarte and Shapiro [30] suggested a modification of the original ADM equations which "factors out" a conformal factor and introduces auxiliary spatial connection functions. Baumgarte and Shapiro made a direct comparison of the numerical performance of the modified equations with the standard "3+1" ADM equations and found that, in conjunction with a pure Sommerfeld outer boundary condition, the modified form exhibits much improved stability. I feel that this method certainly deserves attention from the numerical relativity community and I wish to try this new formalism for the evolution of relativistic boson stars particularly since it may provide a route to stabilizing my currently unstable code.

Chapter 3

Numerical Methods

3.1 Finite Difference Techniques

I use finite difference methods [3, 32] to solve the equations introduced in Chapter 1. Given partial differential equations (PDEs) to solve, one replaces differential operators by finite difference (FD) operators, and then solves the (algebraic) finite difference equations using direct methods or iterative methods. In FD methods, one has to construct finite difference operators so that the solutions to the FD equations provide correct approximate solutions to the original PDEs. Here I define some FD operators which will be used throughout this thesis.

$$\Delta_t f_{i,j,k}^{n+\frac{1}{2}} = (f_{i,j,k}^{n+1} - f_{i,j,k}^n)/dt \tag{3.1}$$

$$\Delta_{xx} f_{i,j,k}^n = (f_{i+1,j,k}^n - 2f_{i,j,k}^n + f_{i-1,j,k}^n)/dx^2 \tag{3.2}$$

$$\Delta_{yy} f_{i,j,k}^n = (f_{i,j+1,k}^n - 2f_{i,j,k}^n + f_{i,j-1,k}^n)/dy^2 \tag{3.3}$$

$$\Delta_{zz} f_{i,j,k}^n = (f_{i,j,k+1}^n - 2f_{i,j,k}^n + f_{i,j,k-1}^n)/dz^2 \tag{3.4}$$

There are two important concepts for any accurate numerical solutions of time dependent problems using FD techniques: stability and convergence.

Stability addresses the issue of whether or not generated numerical solutions have a tendency to blow up at some finite time. Thus, stability analysis is concerned with the conditions under which the difference between the analytic and numerical solutions of the difference equation remains bounded as $t \to \infty$. To examine the stability of a finite difference calculation, one typically use the von Neumann method, the matrix method, and/or the energy method [3].

The basic idea is that for a time-dependent finite difference solution, $\mathbf{U}^n$ (where n indicates the discrete time-step), the totality of difference equations can be written in matrix form,

$$\mathbf{U}^{n+1} = C_n \mathbf{U}^n \tag{3.5}$$

Then, in general, the spectral radius condition

$$\rho(C) \leq 1 \tag{3.6}$$

is necessary for stability and the norm condition

$$||C|| \leq 1 \tag{3.7}$$

is sufficient for stability [3].

For the finite difference method used for the Schrödinger equation (Crank-Nicholson scheme), we have $||C|| = 1$. Thus it preserves unitarity.

The concept of convergence testing, an other important idea from numerical analysis which I will use below, involves verification that our numerical solutions *do* converge to the exact solution in the limit where the mesh-spacing approaches zero [33]. For sufficiently smooth solutions of our PDEs, we can expect that the solution error will vanish as rapidly as the truncation error, and demonstration of a converging solution is a vital step in assessment of the quality of any FD results.

However, there may be cases where convergence testing may need to be supplemented with "independent residual evaluation". To ensure consistency of the FD solution with the original continuum PDE, one constructs an independent finite difference approximation to the original differential equation, $\tilde{L}$. Then one computes the convergence factor (see below) of $\tilde{L}\hat{u}$, where $\hat{u}$ is the FD solution. By demonstrating that these independent residuals converge, one can produce convincing evidence that the FD is converging to the continuum solution.

I define a convergence factor, c_h, as

$$c_h \equiv \frac{f_h - f_{\frac{h}{2}}}{f_{\frac{h}{2}} - f_{\frac{h}{4}}} \tag{3.8}$$

Assuming the ansatz

$$\hat{u} = u + O(\Delta x^2 + \Delta t^2) \tag{3.9}$$

where u is an analytic solution, $\hat{u}$ a numerical solution, the convergence testing will ensure that the numerical solution remains always within the second order errors by checking the numerical value of c_h even in the case one does not know the exact solutions. For a second order scheme, c_h tends to 4 as $h \to 0$.

Fig. 3.1 shows a convergence factor for the solution of a 1D Schrödinger equation in an periodic optical lattice. One of the things one can see from this plot is that a breakdown of the convergence factor signals the breakdown of the numerical solution. Fig. 3.2 shows corresponding quantum mechanical currents computed from the solutions to the 1D
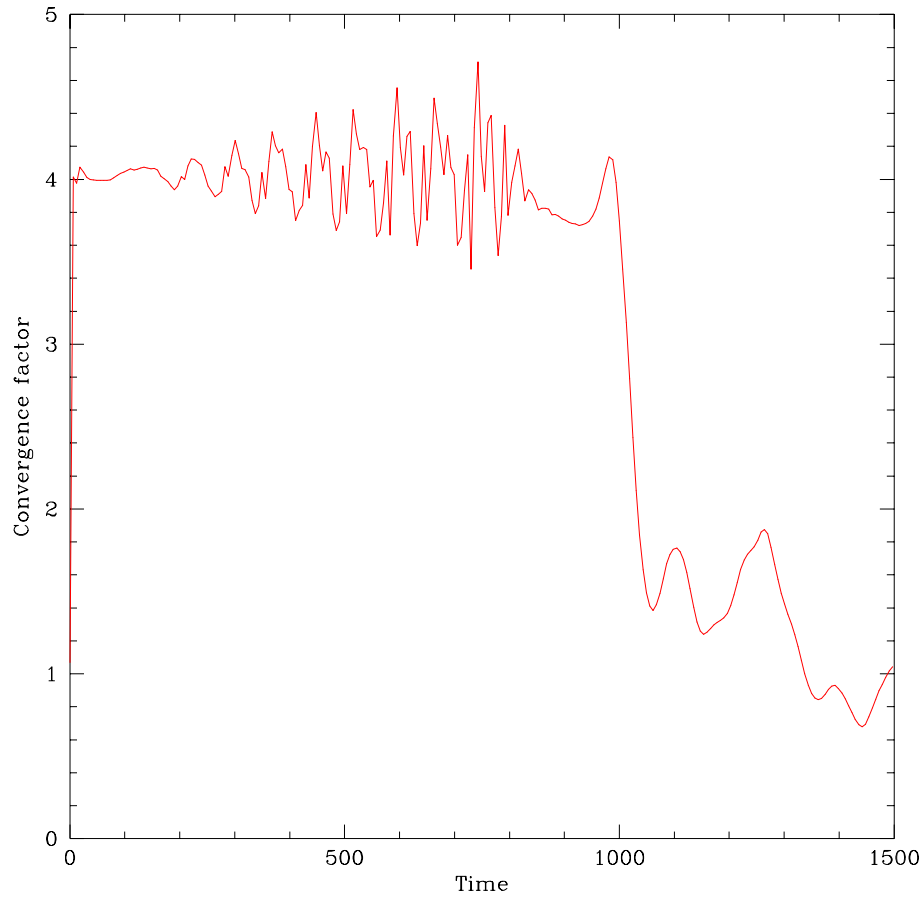
Figure 3.1: Convergence factor for a 1D Schrödinger solver as a function of time

Schrödinger equation as a function of time. The currents starts to behave "chaotically" when the convergence breaks down.

The most commonly used FD technique for the Schrödinger equations is the Crank-Nicholson (CN) scheme [32]. For linear problems, the CN scheme is unconditionally stabile–i.e. stable for any timestep. The scheme is second order accurate in both space and time, and has the further property (already noted above), that it maintains unitarity of the solution. Although this scheme is stable for all Δt, one does not generally want to choose Δt too large, since then the local truncation error may become unacceptably large. To solve the CN finite-difference equations, I have used the Alternating Direction Implicit (ADI) method (Sec. 3.2) and a MultiGrid (MG) method (3.3). The MG method is also used to solve the Poisson equations for the Newtonian gravitational potential.
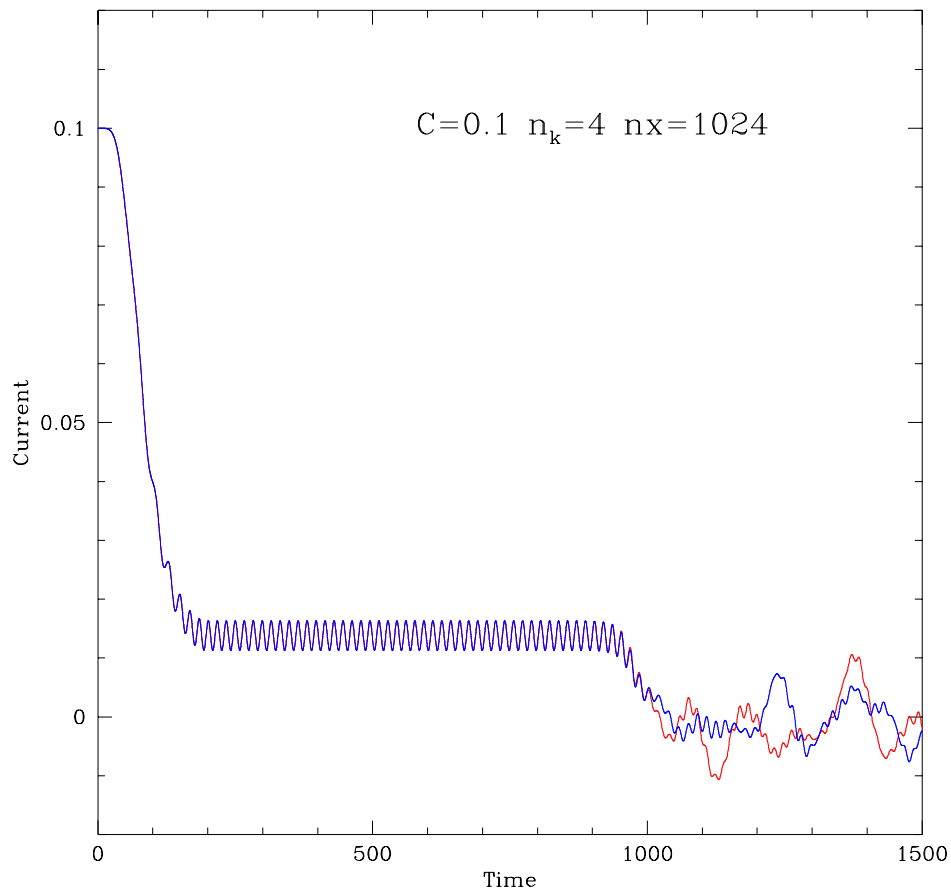
Figure 3.2: Quantum mechanical current $j = (\frac{\hbar}{m})\text{Im}(\phi^* \frac{d\phi}{dx})$ as a function of time.

Considering now the Einstein equations, a similar CN scheme is employed, but with one distinction. Instead of using a tridiagonal solver (or a MG solver), a so-called "CN-iterative" approach is adopted. The CN-iterative approach can be summarized as follows: the difference equations are of the form

$$u^{(n+1)} = u^n + (\Delta t)\mathbf{R}^{(n+\frac{1}{2})} \tag{3.10}$$

where $\mathbf{R}^{(n+\frac{1}{2})}$ is the right-hand-side evaluated at time-level $n + \frac{1}{2}$. The update scheme is carried out by the following procedure.

1 copy the grid functions at the current time-level (u^n) to the next time-level $(u^{(n+1)})$.

2 compute the intermediate level $(u^{n+\frac{1}{2}})$ by taking the average between n level and $n + 1$ level.

3   compute the right-hand-sides(RHS) $\mathbf{R}^{(n+\frac{1}{2})}$ of the equations using $u^{n+\frac{1}{2}}$.

4   update $u^{(n+1)}$, $u^{(n+1)} = u^n + (\Delta t)\mathbf{R}^{(n+\frac{1}{2})}$

5   compute the norm of the difference between thea newly updated $u^{(n+1)}$ and the previous estimate.

6   repeat steps (2) through (6) until the norm of the changes of the advanced values meet some stopping criteria.

This stepping scheme is the only one that has been reasonably successful so far [34].

3.2   Alternating Direction Implicit Method

Explicit difference methods are rarely used to solve initial boundary value problems in multi-dimensional problems [3]. Implicit methods with their superior stability properties are almost always used (NR is somewhat of an exception). However, an implicit method in multi-dimensions results in huge sets of algebraic equations which are not always easy to solve directly.

Alternating direction implicit (ADI) methods are three-step methods involving the solution of tridiagonal sets of equations along lines parallel to the x-, y-, and z-axes at the first, second and third steps respectively. They are two-step methods when restricted to 2D; solving tridiagonal sets of equations along x-, and y-axes at the first and second steps. For linear problems, the ADI method is unconditionally stable and requires $O(N)$ steps to solve where N is the total number of (spatial) grid-points.

For example, the Crank-Nicholson type equation for a 2D Schrödinger equation can be written in the form [118],

$$(1 - \frac{i}{2}\Delta t H)\phi^{(n+1)} = (1 + \frac{i}{2}\Delta t H)\phi^{(n)} \tag{3.11}$$

where $H = \frac{1}{2}(\Delta_{xx} + \Delta_{yy}) - V_{ij}^{n+\frac{1}{2}}$. Then, the equation can be broken up into three equations:

$$(1 - \frac{i}{4}\Delta t \Delta_{xx})S = (1 + \frac{i}{4}\Delta t \Delta_{xx})\phi^{(n)} \tag{3.12}$$

$$(1 - \frac{i}{4}\Delta t \Delta_{yy})T = (1 + \frac{i}{4}\Delta t \Delta_{yy})S \tag{3.13}$$

$$(1 + \frac{i}{2}\Delta t V_{ij}^{n+\frac{1}{2}})\phi^{(n+1)} = (1 - \frac{i}{2}\Delta t V_{ij}^{n+\frac{1}{2}})T \tag{3.14}$$

These are the difference evolution equations of Eqn. (3.11) in ADI form—given ϕ_{ij}^n, one can use a tridiagonal solver to find the updated function ϕ_{ij}^{n+1}.

3.3 Multigrid Method

Traditional iterative methods for elliptic-type equations such as successive over-relaxation (SOR) techniques have serious drawbacks [6]. Even though SOR is easy to implement and memory-efficient, it usually converges very slowly, and the amount of computational work required per grid point increases rapidly as $h \rightarrow 0$, i.e., as the resolution is increased. Over the past two decades, the Multigrid (MG) method [4, 5] has proven to be very powerful for elliptic-type equations and has been used extensively by numerical relativists [6, 35].

A basic idea of the MG method is the use of coarse grids to speed up the convergence process on fine grids. Fine-grid relaxation is used only to remove high frequency error components from fine grid unknowns. Thus, once the FD solution has been *smoothed* on the fine grid, a related finite difference problem is defined and solved on a coarse grid. The solution is then interpolated back to the fine grid. This idea can be naturally extended to multi-level grid structures. Again, relaxation is used solely to smooth residuals, except at the coarsest grid where the actual solutions are often (but not always) fully computed using relaxation.

For example, a problem given on a grid, Ω^h with a grid spacing h,

$$L^h u^h = f^h \tag{3.15}$$

where L^h is a linear operator, can be recast in the following form,

$$L^h(\tilde{u}^h + v^h) = f^h \tag{3.16}$$

where $\tilde{u}^h$ is an initial estimation and v^h a correction term. By defining a residual,

$$r^h \equiv L^h \tilde{u}^h - f^h \tag{3.17}$$

the equation to solve becomes

$$L^h v^h = -r^h \tag{3.18}$$

If there were some way of representing Eqn. (3.18) accurately on a coarser grid, Ω^H, then an estimate of v^h could be obtained on Ω^H and then interpolated to Ω^h. Again, the idea is that we use a coarse grid to accelerate the convergence of a fine grid problem. One can also use a coarse grid to estimate initial $\tilde{u}^h$,

$$\tilde{u}^h \equiv \Pi_H^h u^H \tag{3.19}$$

I will not go into any more details since there are a number of excellent reviews and papers on this topic [4, 5, 6, 35].

I have implemented both linear correction schemes (LCS) and full approximation schemes (FAS). In a LCS, one computes for a correction term v^h whereas in FAS one directly approximates the solution, u^h on all levels of the multigrid hierarchy [35].

The multigrid solver used in this thesis has been tested extensively for 2- and 3-dimensional problems. Fig. 3.3 shows the convergence of a typical MG solve, in which one case see the rapid convergence characteristic of the technique.
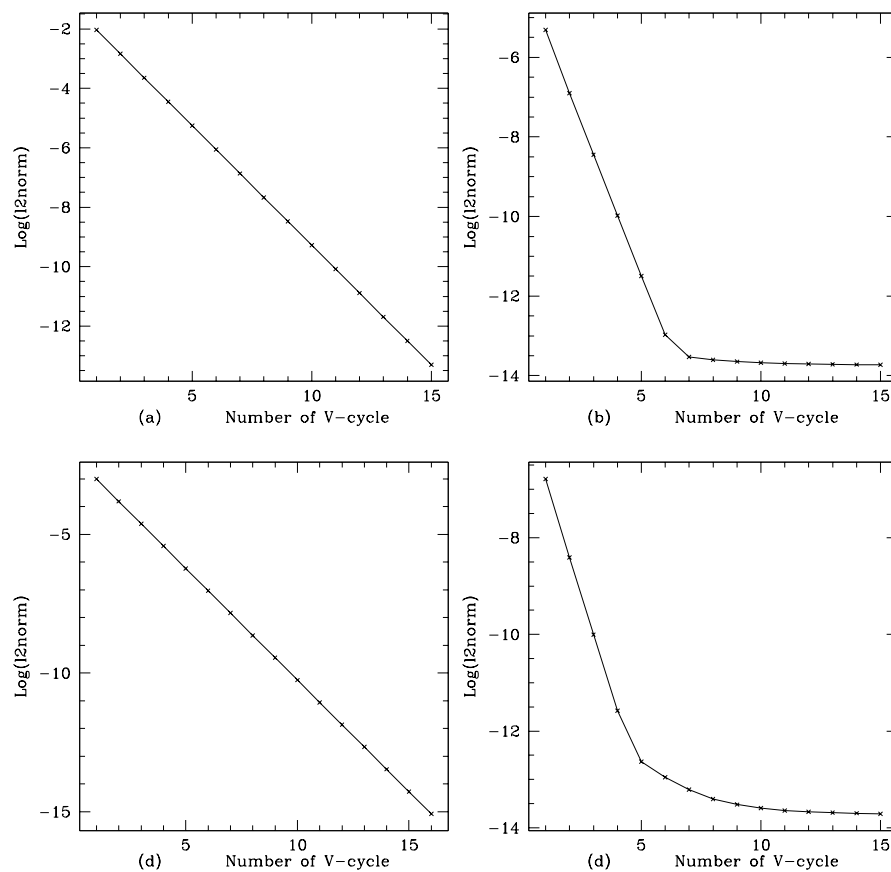
Figure 3.3: Convergence of MultiGrid solvers. (a) and (c) are for the Schrödinger equation and (b) and (d) are for the Poisson equation. (a) and (b) are for an initial data generator and (c) and (d) are for an evolution routine.

I have found that three V-cycles are enough to drive the residual down below 10^{-8} for a Poisson MG solver and it takes about 6 to 7 V-cycle for the Schrödinger equation with Robin-type boundary conditions. For Dirichlet-type boundary conditions, a smaller number

of V-cycle is usually needed to achieve the same-sized residuals. The Schrödinger MG solver converges somewhat more slowly than the Poisson solver, but both solvers converge pretty quickly.

3.4   Annihilation Boundary Condition

Imposing a proper outer boundary condition at the edge of the computational grids is extremely important for a stable numerical evolution of the finite difference equations, and for correct extraction of physical results from the simulations. Very often what one experiences in practice is either an unstable evolution at or around the computational boundaries, or a reflection of unphysical modes off the boundaries. Often the amount of work being put to make a stable evolution at the boundaries is of the same order as the effort needed to stabilize an interior evolution.

A major stumbling block for a stable evolution with the Schrödinger fields or the Klein-Gordon fields is a reflection of outgoing waves off the boundaries. These *unphysical* reflections can distort physical information in the interior, and, in fact, can render numerical solutions meaningless after the reflected waves have propagated inward to the regions of interest. For hyperbolic systems such as Klein-Gordon equations, some sort of outgoing radiation conditions can be used to remove some of the outgoing modes, and an approximate outgoing boundary condition for the KG field is explained in Sec. 5.5. This specific approach may not work for parabolic systems like the Schrödinger equation, but our concern is still to minimize spurious reflections. Several boundary conditions which attempt to do this have been reported in the literature.

For example, Baskakov and Popov [36] found a method for computing the boundary condition at a finite point for the 1D Schrödinger equation:

$$i\frac{\partial \phi}{\partial t} = -\frac{\partial^2 \phi}{\partial x^2}\phi - V(x,t)\phi \tag{3.20}$$

in a region where the potential $V(x,t)$ is nearly zero. Using a Green's function technique, they found that at $x = \pm a$:

$$i\frac{\partial \phi(\pm a, t)}{\partial x} = \mp\frac{e^{-i\pi/4}}{\sqrt{\pi}}\frac{\partial}{\partial x}\int_0^t \phi(\pm,\xi)\frac{d\xi}{\sqrt{t-\xi}} \tag{3.21}$$

where it is assumed that $V(\pm a, t) = 0$. This can be generalized to 3D, but one cannot assume that the potential will be zero at the computational boundaries for the time-dependent Schrödinger problem.

Another and more popular outer boundary condition for the Schrödinger equation is the "absorbing boundary condition" of Israeli and Orszag [37]. They suggest equating the

Schrödinger equation with the wave equation in the operator form:

$$\frac{\partial^2 \phi}{\partial x^2} = (-i\frac{\partial}{\partial t} + V)\phi \equiv L^2\phi \tag{3.22}$$

where the operator L is given formally by

$$L = \sqrt{(-i\frac{\partial}{\partial t} + V - \omega_0) + \omega_0} \tag{3.23}$$

and is approximated by

$$L \simeq \frac{1}{2}\sqrt{\omega_0} + \frac{1}{2\sqrt{\omega_0}}(-i\frac{\partial}{\partial t} + V) \tag{3.24}$$

This approximation of L can be used to provide boundary conditions:

$$(\frac{\partial}{\partial x} \pm L)\phi = 0 \quad \text{at} \quad x = \pm a \tag{3.25}$$

which allow only the outgoing parts of ϕ to propagate. The absorbing boundary condition also has drawbacks. It is effective only for the component of outgoing wave whose oscillation frequency is near ω_0, and, in multiple space dimensions, only those waves with normal, or near-normal, incidence are absorbed effectively.

The annihilation boundary condition discussed here has been found to perform better than the absorbing boundary condition. Basically, the annihilation condition damps out all frequency components and extends easily to multiple dimensions [118].

The basic idea can be seen as follows. Consider the 1D Schrödinger equation with $V = 0$,

$$\frac{\partial \phi}{\partial t} = i\frac{\partial^2 \phi}{\partial x^2} \tag{3.26}$$

Given the initial data,

$$\phi(x, t = 0) = \sum_{k=-\infty}^{\infty} A_k e^{ikx} \tag{3.27}$$

this equation has the solution

$$\phi(x, t) = \sum_{k=-\infty}^{\infty} A_k \exp[-ik^2 t + ikx] \tag{3.28}$$

The annihilation boundary condition is implemented by adding an imaginary potential to the equation. Specifically, we add a term $-\nu(x)\phi$, yielding

$$\frac{\partial \phi}{\partial t} = i\frac{\partial^2 \phi}{\partial x^2} - \nu\phi \tag{3.29}$$

where $\nu(x) \geq 0$ for all x.

Given the same initial data, the solutions of the above equation are given by

$$\phi(x,t) = \sum_{k=-\infty}^{\infty} A_k \exp[(-ik^2 - \nu)t + ikx] \tag{3.30}$$

Clearly then, the solution is damped exponentially in time. Therefore by setting $\nu(x)$ to be non-zero only in the vicinity of computational boundaries, one can effectively remove outgoing modes and prevent any significant reflection off the edges of the grids. In the case where $V \neq 0$, the analysis is more complicated, but the basic idea of the exponential decay of the wavefunction still applies.

Fig. 3.4 shows the time evolution of the exact and numerical solutions for a 1D Schrödinger equation with no potential. The annihilation boundary condition is imposed in the region $40 \leq x \leq 50$. It is clear that the numerical solution is completely damped away without significantly changing the solution in the region interior to the annihilation layer.

3.5   Periodic Boundary Condition

Periodic boundary conditions are often used in quantum mechanical systems where solutions and potentials are often required to be periodic.

A common example is crystals in solid state physics, where a periodic structure of the atomic potential naturally imposes periodicity on the solutions. Another example occurs in the context of cosmological simulations. It is well known that large structure of the universe exhibits a remarkable homogeneity and isotropy. Here, periodic boundary condition are fairly accurate if the scales of interests are smaller than the scale of homogeneity [38].

Implementation of periodic boundary conditions can be done in various way. My implementation involves the addition of an extra grid point at the end of the grid in each coordinate direction, and the identification of grid points at boundaries as well as the grid points right next to the original boundaries at each time-level. For example, consider a 1D grid as shown in Fig. 3.5. The original grid consists of the circled points. To implement the periodic boundary condition, I add extra grid points next to the original boundary points (squares in the Fig. 3.5). I update the solution at the circled points on the $n + 1$ time level from level n data. Note that the original boundary points at the $n + 1$ time level (filled circles) do not have to be treated differently from any other points. After updating all of the circled points at the $n + 1$ time level, I identify the two filled circles and the grid points next to them as indicated by the arrows in the figure.

Fig. 3.6 shows solutions of a 1D nonlinear Schrödinger equation in an accelerating periodic optical lattice (See the chapter 6 for details).

$$i\frac{\partial \phi}{\partial t} = -\frac{1}{2}\frac{\partial^2 \phi}{\partial x^2} + V_0 \cos(x)\phi + C|\phi|^2\phi \tag{3.31}$$

The wavefunction under the periodic lattice potential is also periodic and follows the accelerating potential.
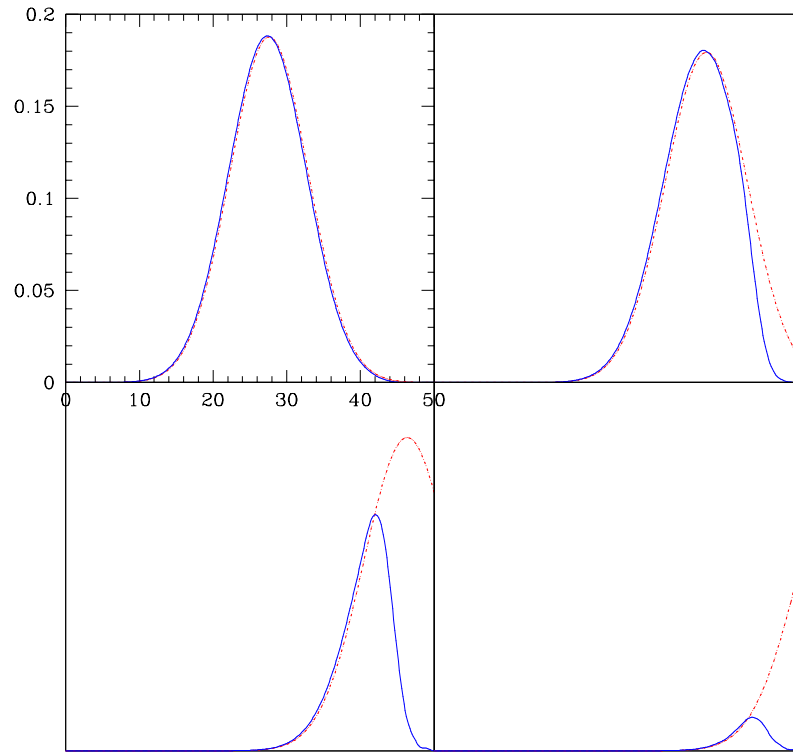
Figure 3.4: Time evolution of exact and numerical data for a 1D Schrödinger equation with an annihilation boundary condition. Initial data for the wavefunction is a moving Gaussian pulse. Dotted and solid lines represent exact and numerical solutions respectively.
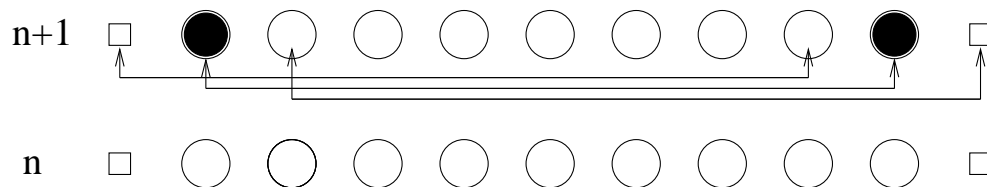
Figure 3.5: Schematic diagram for my 1D implementation of the periodic boundary condition. Extra grid points (squares) are added next to the original boundary points. After updating the original grid points (circles), identification is made as indicated by arrows to enforce periodicity.
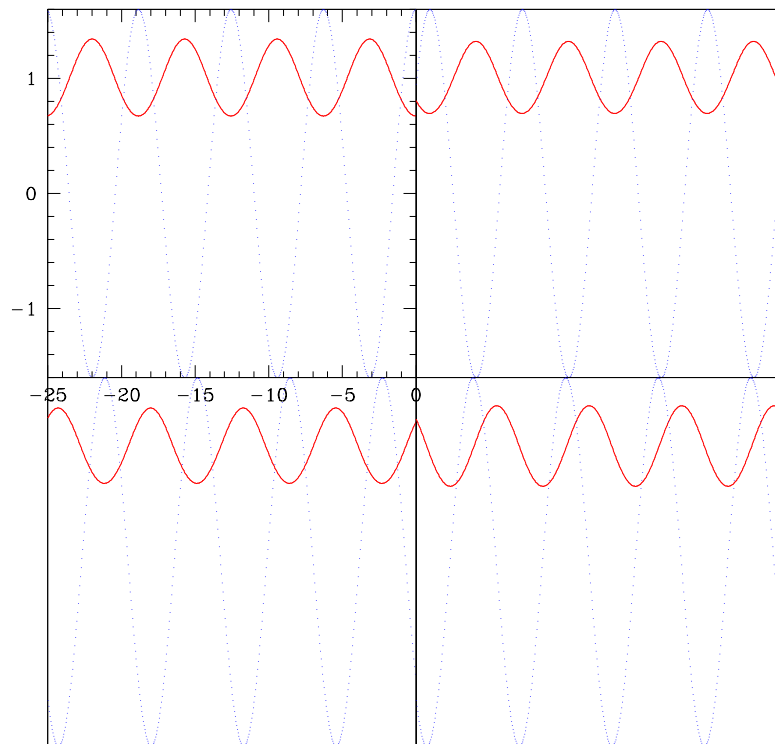
Figure 3.6: Time evolution of a 1D nonlinear Schrödinger equation in an accelerating periodic optical lattice. An acceleration $a = 0.02$ and $C{=}1$. Solid lines represent the wavefunction and dotted lines the periodic optical lattice potential.

Chapter 4

Newtonian Boson Stars

4.1 Introduction

A resurgence of interest in scalar fields in the context of astroparticle physics and quantum cosmology [39] has prompted investigation of their dynamics, particularly since they are possible dark matter candidates [40]. It has been speculated that scalar fields may have played an important role in inflationary theories [41, 42], and in the formation of Q-balls [43], scalar soliton stars [44], and boson stars. Recently, there have been even some speculations about possible observations of boson stars [19, 20, 46] even though the feasibility of those scenarios has yet to be fully examined. Therefore, it is interesting to study formation[45] and stability properties of these objects, as well as other astrophysical roles, such as the possibility that they may act as sources of gravitational radiation.

In this thesis, I am interested in the dynamical study of boson stars in two and three spatial dimensions. Boson stars are macroscopic equilibrium configurations of a self-gravitating massive complex scalar field. These stars are thus nontopological soliton solutions, i.e., they have a finite non-zero mass confined to a finite region of spacetime (compact), and are free of singularities.

Intuitively, boson stars can exist because the attractive gravitational force can be balanced by the tendency of the scalar fields to disperse. Since the number of particle, N, is usually astronomically large, the phenomenology of the scalar fields can be completely described classically without considering any possible–but not yet known–precise connections to the underlying fundamental quantum field.

The typical mass of a boson star can be estimated as follows. The boson momentum is $p \sim (1/\lambda) \sim (1/R)$. If the boson star is moderately relativistic, $p \simeq m$, then $R \simeq (1/m)$. Equating R with the Schwarzschild radius, $(2M/M_{PI}^2)$ $(G \equiv M_{PI}^{-2})$, $M \simeq (M_{PI}^2/m)$. The bosonic matter can be made to couple to itself via, for example, a $\lambda\phi^4$ type self-interaction [9], or the field may be coupled to other types of matter. In the case of a self-interacting field, the typical mass becomes comparable to the Chandrasekhar mass, $M \simeq \sqrt{\lambda}(M_{PI}^3/m^2)$ [9]. For example, for the mass of the particle, $m = 1$ GeV, $M_{BS} \simeq 10^{-19}M_\odot$ for $\lambda = 0$ whereas

$M_{BS} \simeq 0.1 M_{\odot}$ for $\lambda = 0.01$. (A typical mass of a neutron star is $M_{NS} \simeq M_{\odot}$) However, the total mass versus radius curve is similar to that of neutron stars and white dwarfs.

Even though any direct physical relevance has yet to be demonstrated, boson star systems provide excellent numerical laboratories in which to study strong gravitational fields or gravitationally bound compact systems.

Specifically, the boson star model provides an ideal vehicle with which to implement and evaluate (1) various coordinate conditions in the context of the ADM formalism, and (2) multi-dimensional adaptive mesh refinement techniques which appear crucial for many problems in 3D numerical relativity.

In this Chapter, I first consider boson stars in the Newtonian regime. Studying the Newtonian limit is useful because the equations of motion are simpler than in the relativistic case; we simply have a Schrödinger equation coupled to a Poisson equation. These equations are straightforward to solve and do not involve the problems of coordinate choice and constraint equations present in the relativistic case.

In this Chapter, the (numerical) stability of single star systems is demonstrated and the interaction of multiple-star-systems is simulated.

4.2   Equations of Motion

Relativistic boson stars are described by stationary solutions of the Einstein-Klein-Gordon equation:

$$g^{\mu\nu}\phi_{;\mu\nu} - m^2\phi = 0 \tag{4.1}$$

$$G^{\mu\nu} = R^{\mu\nu} - \frac{1}{2}g^{\mu\nu}R = 8\pi G T^{\mu\nu} \tag{4.2}$$

which may be derived from the following Lagrangian:

$$I = \int d^4x \sqrt{-g} \left[\frac{R}{16\pi G} - \frac{1}{2}\left(g^{\mu\nu}\partial_\mu\phi^*\partial_\nu\phi + m^2\phi^*\phi\right) \right] \tag{4.3}$$

When the gravitational field is weak enough to be considered "Newtonian", and the velocity that characterize the system is small compared to the speed of light, the Einstein-Klein-Gordon equation reduces to the Schrödinger-Poisson equation [118]. One can derive the Schrödinger-Poisson equation assuming that the metric takes the form:

$$g_{00} = -(1 + 2V); \quad g_{11} = g_{22} = g_{33} = (1 - 2V) \tag{4.4}$$

$$g_{\alpha\beta} = 0 \quad \text{for} \quad \alpha \neq \beta \tag{4.5}$$

where V is a Newtonian gravitational potential. In the Newtonian limit of general relativity, it can be shown that: [47]

$$\nabla^2 V = 4\pi G T^{00} \tag{4.6}$$

and

$$T^{00} \simeq m^2 \phi^* \phi \tag{4.7}$$

Thus,

$$\nabla^2 V = 4\pi G m^2 \phi^* \phi \tag{4.8}$$

This Poisson equation is, of course, just the field equation for the Newtonian gravitational field.

In addition, substituting the above metric, Eqns. 4.4 and 4.5, into the KG equation, and assuming the positive energy eigenvalue condition, one obtains the Schrödinger equation for ϕ.

Therefore, the equations to solve for Newtonian boson stars are

$$i\frac{\partial \phi}{\partial t} = -\frac{1}{2}\nabla^2 \phi + V\phi \tag{4.9}$$

$$\nabla^2 V = \phi\phi^* \tag{4.10}$$

Again, I am using Planck units ($G = c = \hbar = 1$) and furthermore, all variables have been non-dimensionalized as follows:

$$\mathbf{x}_{\text{phy}} = \frac{\hbar}{mc}\mathbf{x}_{\text{comp}} \tag{4.11}$$

$$t_{\text{phy}} = \frac{\hbar}{mc^2}t_{\text{comp}} \tag{4.12}$$

$$\phi_{\text{phy}} = \frac{c^2}{\sqrt{4\pi G}}\phi_{\text{comp}} \tag{4.13}$$

where "phy" and "comp" denote physical and computational, respectively.

Near the boundaries of the computational domain, I use an annihilation condition as discussed in Chapter 3.4. Thus the Schrödinger equation becomes

$$i\frac{\partial \phi}{\partial t} = -\frac{1}{2}\nabla^2 \phi + (V - i\nu)\phi \tag{4.14}$$

As discussed previously, the annihilation layer minimizes the reflections off the computational boundary by effectively damping the scalar field (in the layer where $\nu(x)$ is non-zero) as $\phi \sim e^{-\nu(\mathbf{x})t}$.

4.3 Numerics

A Crank-Nicholson (CN) scheme is used to solve the Schrödinger equation (4.9). In a CN scheme, spatial derivatives are replaced by finite difference operators centered at a "half time level". Specifically, the Schrödinger equation is differenced as

$$\Delta_t \phi_{ijk}^{n+\frac{1}{2}} = (\frac{i}{2}(\Delta_{xx} + \Delta_{yy} + \Delta_{zz}) - iV_{ijk}^{n+\frac{1}{2}} - \nu_{ijk}^{n+\frac{1}{2}})\phi_{ijk}^{n+\frac{1}{2}} \tag{4.15}$$

where $\phi_{ijk}^{n+\frac{1}{2}}$ is replaced by $\frac{1}{2}(\phi_{ijk}^{n+1} + \phi_{ijk}^n)$ and the operators $\Delta_t, \Delta_{xx}, \Delta_{yy}$ and Δ_{zz} are defined by Eqns. (3.1–3.4).

To solve equation (4.15), I have used two methods: the ADI (Alternating Direction Implicit) method and the MG (multigrid) method.

In the ADI approach, the above difference equation is written in the form:

$$(1 - \frac{i}{4}\Delta t \Delta_{xx})S_{ijk} = (1 + \frac{i}{4}\Delta t \Delta_{xx})\phi_{ijk}^{(n)} \tag{4.16}$$

$$(1 - \frac{i}{4}\Delta t \Delta_{yy})T_{ijk} = (1 + \frac{i}{4}\Delta t \Delta_{yy})S_{ijk} \tag{4.17}$$

$$(1 - \frac{i}{4}\Delta t \Delta_{zz})U_{ijk} = (1 + \frac{i}{4}\Delta t \Delta_{zz})T_{ijk} \tag{4.18}$$

$$(1 + \frac{i}{2}\Delta t V_{ij}^{n+\frac{1}{2}})\phi_{ijk}^{(n+1)} = (1 - \frac{i}{2}\Delta t V_{ij}^{n+\frac{1}{2}})U_{ijk} \tag{4.19}$$

To apply the MG method, terms in Eqn (4.15) are re-arranged so that all advanced $(n+1)$-level terms appear on the left hand side whereas all current (n)-level terms appear on the right. Then, the equation to solve is given by

$$\phi_{ijk}^{n+1} - \frac{i\Delta t}{4}(\Delta_{xx}\phi^{n+1} + \Delta_{yy}\phi^{n+1} + \Delta_{zz}\phi^{n+1}) + \frac{i\Delta t}{2}V_{ijk}^{n+\frac{1}{2}}\phi_{ijk}^{n+1} + \frac{\Delta t}{2}\nu_{ijk}^{n+\frac{1}{2}}\phi_{ijk}^{n+1}$$
$$= \phi_{ijk}^n + \frac{i\Delta t}{4}(\Delta_{xx}\phi^{n+1} + \Delta_{yy}\phi^{n+1} + \Delta_{zz}\phi^{n+1}) - \frac{i\Delta t}{2}V_{ijk}^{n+\frac{1}{2}}\phi_{ijk}^n - \frac{\Delta t}{2}\nu_{ijk}^{n+\frac{1}{2}}\phi_{ijk}^n \tag{4.20}$$

The above equation is of the form $L[\phi^{n+1}] = f(\phi^n)$ where the right hand side $f(\phi^n)$ is already known from the (n)-level unknowns, ϕ^n. The unknowns, ϕ^{n+1}, can then be determined using a MG solver.

The same MG solver is used to solve the elliptic Poisson equation for the Newtonian gravitational potential. The fact that the same solution method is used for both Schrödinger and Poisson equation should simplify the development of my *parallel* version of the code, which is currently under construction.

4.4 Initial Value Problem

In this section, I discuss how to solve for a stationary boson star and how to set up the field configurations which will be used as initial data for the dynamical studies.

Setting up the initial data for 3D numerical relativity is in itself a tremendous problem. (It is discussed in Section 5.3.) However the situation is much simpler in the Newtonian case.

First, to generate a ground state boson star configuration, I assume spherical symmetry and the following *ansatz*:

$$\phi(\mathbf{x}, t) = e^{-i\omega t}\phi(r) \tag{4.21}$$

where ω is an intrinsic oscillation frequency for the complex scalar field. By plugging Eqn. (4.21) in the Eqn. (4.9) and (4.10), one gets the following ordinary differential equations, (in spherical coordinates):

$$\frac{1}{2r^2}\frac{\partial}{\partial r}\left(r^2\frac{\partial\phi}{\partial r}\right) + (\omega - V)\phi \;=\; 0 \tag{4.22}$$

$$\frac{1}{r^2}\frac{\partial}{\partial r}\left(r^2\frac{\partial V}{\partial r}\right) \;=\; \phi\phi^* \tag{4.23}$$

I can further assume that ϕ is a real function without loss of generality. By introducing auxiliary variables, a set of 4 first-order ODEs follows,

$$\frac{\partial\phi}{\partial r} = \phi' \tag{4.24}$$

$$\frac{\partial\phi'}{\partial r} = -\frac{2\phi}{r} + 2(\omega + V)\phi \tag{4.25}$$

$$\frac{\partial V}{\partial r} = V' \tag{4.26}$$

$$\frac{\partial V'}{\partial r} = -\frac{2V'}{r} + \phi^2 \tag{4.27}$$

for r $\neq$ 0 and

$$\frac{\partial\phi}{\partial r} = \Phi \tag{4.28}$$

$$\frac{\partial\Phi}{\partial r} = \frac{2}{3}(\omega + V)\phi \tag{4.29}$$

$$\frac{\partial V}{\partial r} = W \tag{4.30}$$

$$\frac{\partial W}{\partial r} = \frac{1}{3}\phi^2 \tag{4.31}$$

for r = 0. This set of ODEs is subject to four boundary conditions:

$$\Phi(r = 0) \;=\; 0 \tag{4.32}$$

$$W(r = 0) \;=\; 0 \tag{4.33}$$

$$\phi(r \to \infty) \;=\; 0 \tag{4.34}$$

$$V(r \to \infty) \;\propto\; -\frac{M}{r} \tag{4.35}$$

for a Dirichlet-type boundary condition and

$$V \sim -r \frac{\partial V}{\partial r} = -rW, \quad r \to \infty \tag{4.36}$$

for a Robin-type boundary condition.

These equations form an eigenvalue problem for ω. In other words, given $\phi(r = 0)$, the solution exists only for certain values of ω. A ground state boson star solution is a zero-node solution. (Solutions with one or more node correspond to excited states.) A binary search algorithm is used to find the eigenvalues in the ODE solver: for a given value of $\phi(r = 0)$, the code uses a binary search in ω to find a zero-node solution that satisfies the asymptotic conditions.

Solutions for other values of $\phi(r = 0)$ follow immediately thanks to a scaling law based on a property of these particular ODEs [8]. Therefore, I can obtain a solution of an arbitrary value of $\phi(r = 0)$ simply by making an appropriate scale change from an already-known solution for a certain value of $\phi(r = 0)$. Consider two solutions labeled by indices 1 and 2. Then the following scaling relations hold between the solutions:

$$\omega_2 = \omega_1 \left(\frac{N_2}{N_1} \right)^2 \tag{4.37}$$

$$r_2 = r_1 \left(\frac{N_1}{N_2} \right) \tag{4.38}$$

$$\phi_2 = \phi_1 \left(\frac{N_2}{N_1} \right)^2 \tag{4.39}$$

$$V_2 = V_1 \left(\frac{N_2}{N_1} \right)^2 \tag{4.40}$$

where N is the conserved particle number given by

$$N = m \int d^3 x \phi \phi^* \tag{4.41}$$

Let us assume that the solution "2" satisfies the Eqns. (4.22) and (4.23):

$$\frac{1}{2r_2^2} \frac{\partial}{\partial r_2} \left(r_2^2 \frac{\partial \phi_2}{\partial r_2} \right) + (\omega_2 - V_2) \phi_2 = 0 \tag{4.42}$$

$$\frac{1}{r_2^2} \frac{\partial}{\partial r_2} \left(r_2^2 \frac{\partial V_2}{\partial r_2} \right) = \phi_2^2 \tag{4.43}$$

Applying the scaling relstions, Eqns. (4.37), (4.38), (4.39), and (4.40), one gets

$$\left(\frac{1}{2r_1^2} \frac{\partial}{\partial r_1} \left(r_1^2 \frac{\partial \phi_1}{\partial r_1} \right) + (\omega_1 - V_1) \phi_1 \right) \left(\frac{N_2}{N_1} \right)^4 = 0 \tag{4.44}$$

$$\left(\frac{1}{r_1^2} \frac{\partial}{\partial r_1} \left(r_1^2 \frac{\partial V_1}{\partial r_1} \right) \right) \left(\frac{N_2}{N_1} \right)^4 = \left(\phi_1^2 \right) \left(\frac{N_2}{N_1} \right)^4 \tag{4.45}$$

Thus the solution "1" also satisfies the initial value equations.

Fig. 4.1 shows profiles of typical boson stars. The distribution of ϕ^2 forms a compact object: it has an exponential tail.
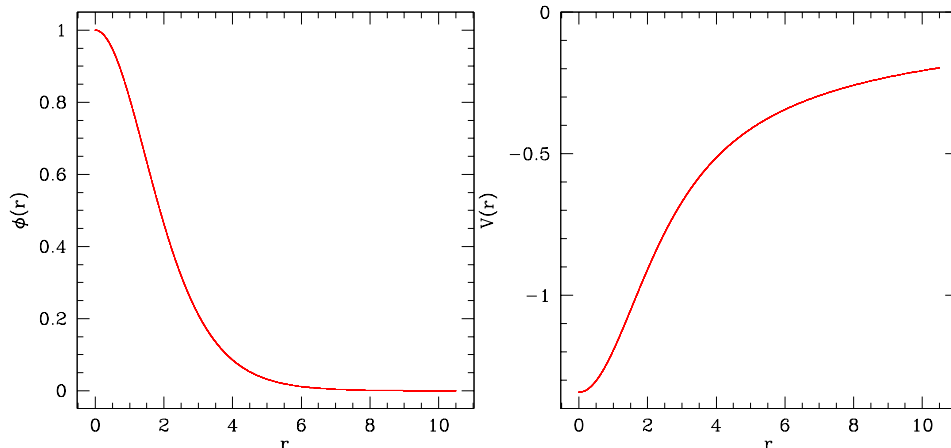
Figure 4.1: This figure shows a Schrödinger field, ϕ, and a Newtonian potential, V, as a function of r for a stationary boson star

To give a boson star linear momentum, one can simply convolve $\phi(\mathbf{x}, t)$ with $e^{i\mathbf{P}\cdot\mathbf{x}}$. To produce spinning stars, one can also give angular momentum in quantized increments to the configuration by convolving $\phi(\mathbf{x}, t)$ with $e^{iN\varphi}$, where φ is an azimuthal angle measured with respect to the axis of rotation. To set up multiple boson star initial data, I simply superimpose the wavefunctions of two or more individual stars, compute the total energy density $\rho_{\text{total}}(\mathbf{x}) = \sum_i \rho_i(\mathbf{x})$ and then re-solve the Poisson equation for the initial gravitational potential. I have tested my codes with each one of these initial data sets.

4.5   2D Stars

I start with 2D boson stars since 2D simulation is computationally less demanding than full 3D calculations. The 2D boson star code has also served as a testbed code for all my subsequent 2D Schrödinger applications.

Here I impose slab symmetry along the z-axis on the spatial domain. This naturally removes z-dependence from the equations. I then examine dynamical evolutions of single and multiple "stars" (which are actually infinite cylinders in this case).

In this case, the equations of motion are the Schrödinger and Poisson equations in the usual (x, y) (cartesian) coordinate system:

$$i\frac{\partial \phi}{\partial t} = -\frac{1}{2}(\frac{\partial^2 \phi}{\partial x^2} + \frac{\partial^2 \phi}{\partial y^2}) + V\phi \tag{4.46}$$

$$\frac{\partial^2 V}{\partial x^2} + \frac{\partial^2 V}{\partial y^2} = \phi\phi^* \tag{4.47}$$

I generate a single stationary boson star initial data using the procedure described in Section (4.4). In 2D, solutions of Laplace's equation go like $V \simeq \log(\rho)$ for large ρ. Therefore a Robin-type boundary condition is given by

$$V = \rho\frac{\partial V}{\partial \rho}\log\rho \tag{4.48}$$

as ρ goes to infinity. The ODEs used to construct initial data also differ from the 3D case:

$$\frac{\partial \phi}{\partial \rho} = \phi^{'} \tag{4.49}$$

$$\frac{\partial \phi^{'}}{\partial \rho} = -\frac{\phi}{\rho} + 2(\omega + V)\phi \tag{4.50}$$

$$\frac{\partial V}{\partial \rho} = V^{'} \tag{4.51}$$

$$\frac{\partial V^{'}}{\partial \rho} = -\frac{V^{'}}{\rho} + \phi^2 \tag{4.52}$$

Fig. 4.2 shows the time evolution of a stationary star. It manifests a characteristic oscillation with a frequency which depends on the total mass of the star, M_{BS}. I used $\phi_0 = 1.0$ for all calculations in this section. The characteristic internal frequency of the complex scalar field ϕ is $\omega = 0.717268$. The stationary star evolves stably and the solution error is estimated to be within 1% over a long period (up to $t = 100$). ($t_{phy} = 1.173 \times 10^{-48}\frac{1}{m}$ g s t_{comp} from Eqn. (4.12). For $m = 1$ GeV, $m = 10^{-54}$g, then $t_{phy} \simeq 10^6 \ t_{comp}$. Thus $t = 100$ corresponds to 10^8 seconds.) The initial jump in the density is due to the fact that the initial data is generated with a higher accuracy than that charteristic of the evolution. After an initial drift, the star oscillates with a characteristic frequency. The short period oscillation is correlated with the intrinsic oscillation of the complex field ϕ, whereas the overall longer oscillation depends on the total mass of the star. If the spatial resolution is increased, the error gets smaller, consistent with the second order accuracy of the numerical scheme.

Fig. 4.3 shows time evolutions of the linear momentum and total mass of boson stars with initial linear momenta defined by

$$l_x = -i\int \phi^* \partial_x \phi \ dxdy \tag{4.53}$$
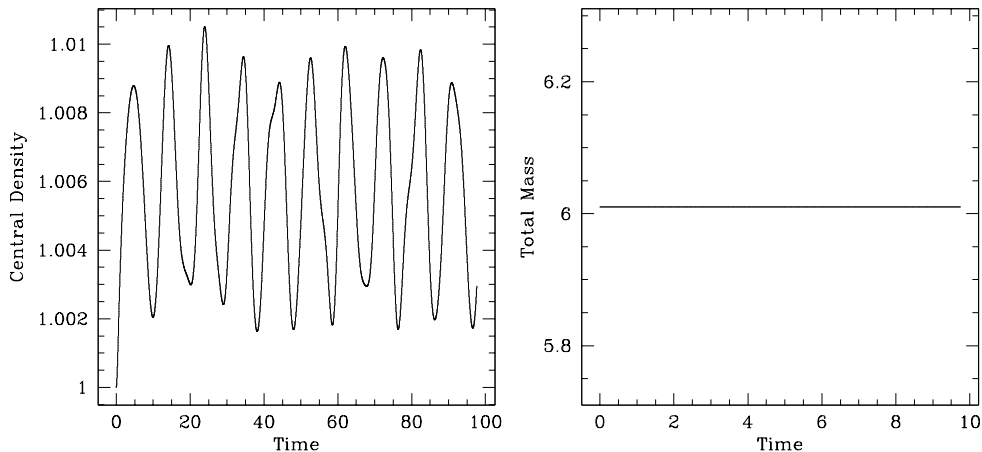
Figure 4.2: This figure shows (a) central density and (b) total mass as a function of time for a single stationary boson star. For this run, $\Delta x = \Delta y = 0.15625$, $\Delta t = 0.1953125$, and the computational domain is $[-20, 20] \times [-20, 20]$

My boson stars show stable evolution for both large and small initial momenta. In all case, total mass is conserved in a manner consistent with the second order accuracy of the difference scheme. The solutions maintain their original profiles very well, but detailed examination of the linear momentum reveals a slight decrease. The reason for this is, in part, due to the fact that I used the Dirichlet-type boundary condition for my MG solution for the gravitational potential, V. My approach fixes values of V at the boundary to the initial values, and thus is only good when the boundary of the computational grid lies at very large r. However, the boundaries of the grid are only modestly far from the origin, $r \simeq 64$ in most of the calculations. In addition, these Dirichlet conditions may also cause some reflections off the boundaries. As a net result, for a long-time run, the star will gradually slow down, eventually stop moving and then will actually reverse direction! However as I will now show, this is clearly a "numerical artifact", and not a physical phenomenon.

Fig. 4.4 shows the same run as Fig. 4.3 (c) and (d) but with the boundary extended to $r \simeq 81$. It can be seen here that the variation in the linear momentum is smaller than the previous case. The total mass is conserved and the overall shape of the stars is kept during the motion.

In the case of periodic boundary conditions, the location of the center-of-mass shows a linear motion, Fig. 4.5. The star passes through the right end and re-appears from the left end. This result confirms that the non-conservation of the linear momenta for the runs with

annihilation boundary conditions, and fixed Newtonian potential at the outer boundary, is indeed a numerical artifact.

Fig. 4.6 shows a time evolution of a head-on collision of a binary star system.

Here one can clearly see a *solitonic* behaviour of the boson stars. The boson stars pass through each other as if a superposition principle holds, even though the interaction is nonlinear. Notice how well the stars keep their identities after the collision. There is a small oscillation after the stars pass through each other, but again, this appears due to problems with the treatment of the boundaries.

Figs. 4.7 - 4.16 show a time evolution of the density profile for a binary star coalescence. Here, initial data is set so that the stars are boosted towards one another with a non-zero impact parameter. In this case, the net linear momentum is zero but the system has a non-zero net angular momentum. In particular, defining the angular momentum operators, L, L_x, L_y and L_z, by

$$\mathbf{L} = \mathbf{r} \times \mathbf{p} = -i\mathbf{r} \times \nabla \tag{4.54}$$

$$L_x = -i(y\frac{\partial}{\partial z} - z\frac{\partial}{\partial y}) \tag{4.55}$$

$$L_y = -i(z\frac{\partial}{\partial x} - x\frac{\partial}{\partial z}) \tag{4.56}$$

$$L_z = -i(x\frac{\partial}{\partial y} - y\frac{\partial}{\partial z}) \tag{4.57}$$

the total (integrated) angular momentum for the 2D configurations being studied is

$$A_z = \int \phi^* L_z \phi \ dxdy \tag{4.58}$$

Fig. 4.17 shows the conservation of this quantity, as well as conservation of the total mass for the binary simulation.

In this evolution, the stars have enough initial momentum to avoid a direct collision, but not enough to escape from each other's gravitational pull so they end up in a mutual orbit. If they were initially closer, the stars would have merged into a single, distorted, rotating star after 1-2 orbits. The "merged star" would radiate some of its energy while settling down to an axisymmetric configuration.

Fig. 4.18 shows results for spinning boson stars with intrinsic angular momenta, $S = 1$ and $S = 2$. Although there is some loss of energy and angular momentum at late times, the evolutions are stable for long times. However, I have found that for $S > 2$, the wave packet rapidly collapses and the subsequent interaction with the boundaries quickly ruins the calculations.

In summary, in this section I have described a 2D boson star code and have demonstrated that the code generates stable evolutions of initially stationary stars, stars with linear momentum, binary star systems and spinning stars.

A modified version of this test-bed code will be used to study interactions of 2D model atoms with strong laser fields in Chapter 7.

4.6 Axisymmetric Stars

The axisymmetric boson star code assumes an axial symmetry about the z-axis. Therefore, the wavefunction and the Newtonian potential do not depend on the azimuthal angle ϕ in the cylindrical coordinate system, and we are again left with a 2D problem. This code also serves as a test-bed for other axisymmetric applications.

In this Section, I study stationary boson stars and binary star systems. The restriction to axisymmetry limits the binary evolutions to head-on collisions.

Fig. 4.19 shows the time evolution of a stationary boson star. As in the 2D calculations, the central density oscillates with a characteristic frequency, but in this case there are two distinctive frequency components, with a ratio of about 5:1.

Fig. 4.20 shows time evolutions of linear momentum and total mass for moving boson stars with linear momentum along the z-axis. Both linear momentum and total mass are well conserved during the evolution. In axisymmetric runs, Dirichlet boundary conditions perform better than in the slab-symmetric runs. This can be attributed to the fact that the Newtonian potential drops off as $1/r$ in this case, whereas for slab symmetry, $V \simeq \log(\rho)$.

In head-on collisions, axisymmetric boson stars sometimes show the same *solitonic* behaviour as in the slab-symmetric case. In particular, for sufficiently large initial momenta, the stars pass through each other as if a superposition principle is in action. For small initial momenta, the stars collide and merge to form a single star. As with the slab-symmetric mergers, after the single star forms, it oscillates, radiating some of its energy in the process.

A modified version of this axisymmetric code will be used in a future study of 3D Bose-Einstein condensates.

4.7 3D Stars

In the preceding two sections, I have dealt with 2D codes. However, development of 3D codes is necessary to study truly generic binary coalescence and merger (i.e. no particular spatial symmetries). Thus far, my 3D runs have been limited to a few simple cases due to a lack of computational resources. However with the help of special techniques such as adaptive

mesh refinement (AMR), I hope I can overcome this limitations to a certain degree in the near future. Currently, development of an AMR program is under way and AMR in general will be discussed in more detail in Chapter 8.

Fig. 4.21 shows a stable evolution of a single stationary boson star and Fig. 4.22 shows a time evolution of the total mass for the same run. I used $\phi_0 = 1.0$ for all the runs in this section. The characteristic internal oscillation frequency for the complex scalar field is computed from the initial value problem: $\omega = 0.649925$. To check long-time stability, I ran a coarse grid evolution of a single stationary boson star, Fig. 4.23. The star remains stable for a fairly long period of time.

Fig. 4.24 shows evolutions of boson stars with linear momenta. For both $v_x = 0.1$ and $v_x = 1.0$, the total mass is well conserved. Linear momentum is well conserved for $v_x = 1.0$ for a short time, $t \sim 20$. For $v_x = 0.1$, conservation is not as good, particularly at late times.

Results for binary star coalescence are given in Fig. 4.25. Initially, the stars are located at $(x_0, y_0, z_0) = (-5.25, 0, 0)$ and $(5.25, 0, 0)$ with linear momenta $p_1 = (0, 0.3, 0)$ and $p_2 = (0, -0.3, 0)$, respectively. The total mass, Fig. 4.25 (a), is conserved for $t \sim 300$ and the linear momentum is conserved up to $t = 220$. It increases for $t \geq 220$. From a careful examination of a full 3D data set (not shown here), it was found that there was mass transfer from one star to the other at $t \sim 180$. In this simulation, the boson stars orbit about each other on trajectories centered on the origin. At the start of the evolution, they attract each other and barely avoid a direct collision. As soon as they separate, gravity pulls them back again. As can be seen from Fig. 4.25 (c) the stars then "skid" through each other periodically.

If the initial separation of the stars is reduced, the two stars quickly merge to form a single rotating star. Fig. 4.26 shows results from a run where the stars start at $(x_0, y_0, z_0) = (-5.0, 0, 0)$ and $(5.0, 0, 0)$, with linear momentum $p_1 = (0, 0.3, 0)$ and $p_2 = (0, -0.3, 0)$. In this case the stars merge before completing a single orbit. In the process, they radiate some of the energy (mass), Fig. 4.26 (a), and oscillate after they have merged at $t \sim 60$, Fig. 4.26 (c). Linear momentum violation increases with time, Fig. 4.26 (b), and this drift eventually moves the final star away from the origin.

Currently, all of the 3D runs are severely restricted by lack of resolution. For more accurate calculations, an AMR version of the code should be implemented, and I will continue to work towards that goal.
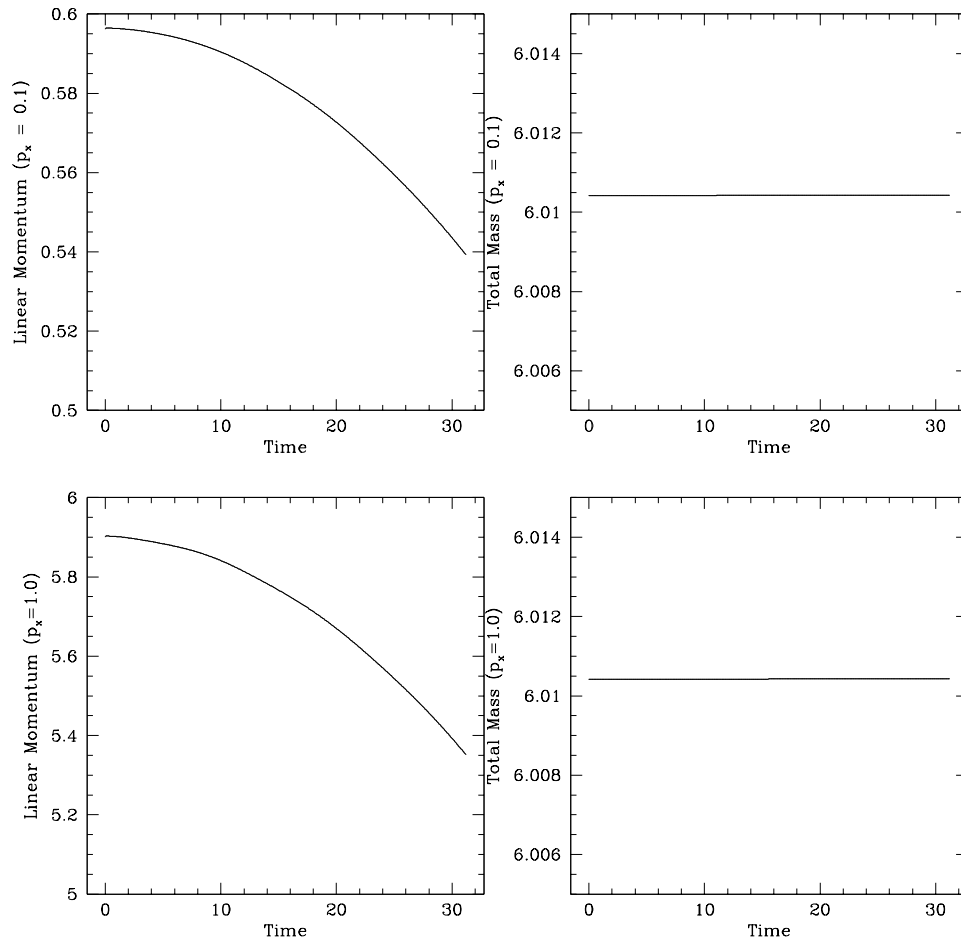
Figure 4.3: This figure shows time evolutions of linear momentum and total mass for a single boson star with initial linear momentum. (a),(b) Initial position x =-3.2 and initial momentum $p_x = 0.1$; (c),(d) Initial position x =-20.25 and initial momentum $p_x = 1.0$. For these runs, computational parameters are $\Delta x = \Delta y = 0.25$, $\Delta t = 0.0625$, and the computational domain is $[-64, 64] \times [-64, 64]$.
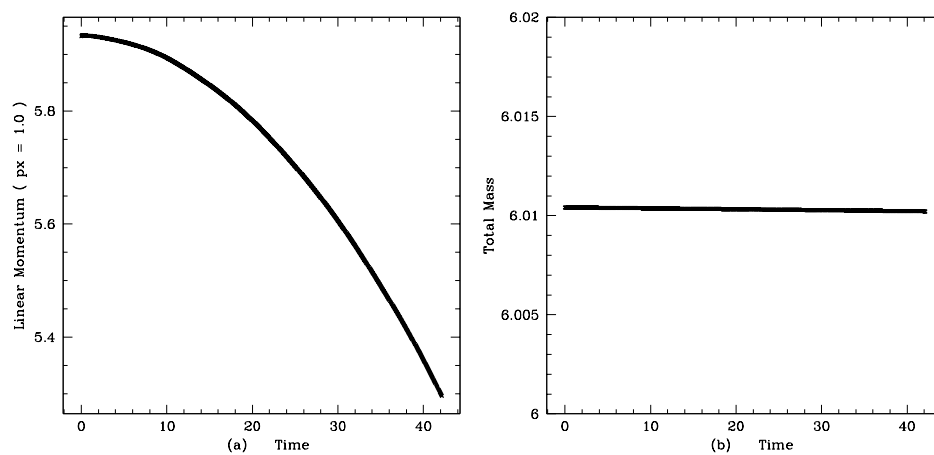
Figure 4.4: This figure shows time evolutions of (a) linear momentum and (b) total mass for a single boson star with an initial linear momentum $p_x = 1.0$ computed in an extended grid. Here $\Delta x = \Delta y \simeq 0.21$, $\Delta t \simeq 0.0527$, and the computational domain is $[-81, 81] \times [-81, 81]$.
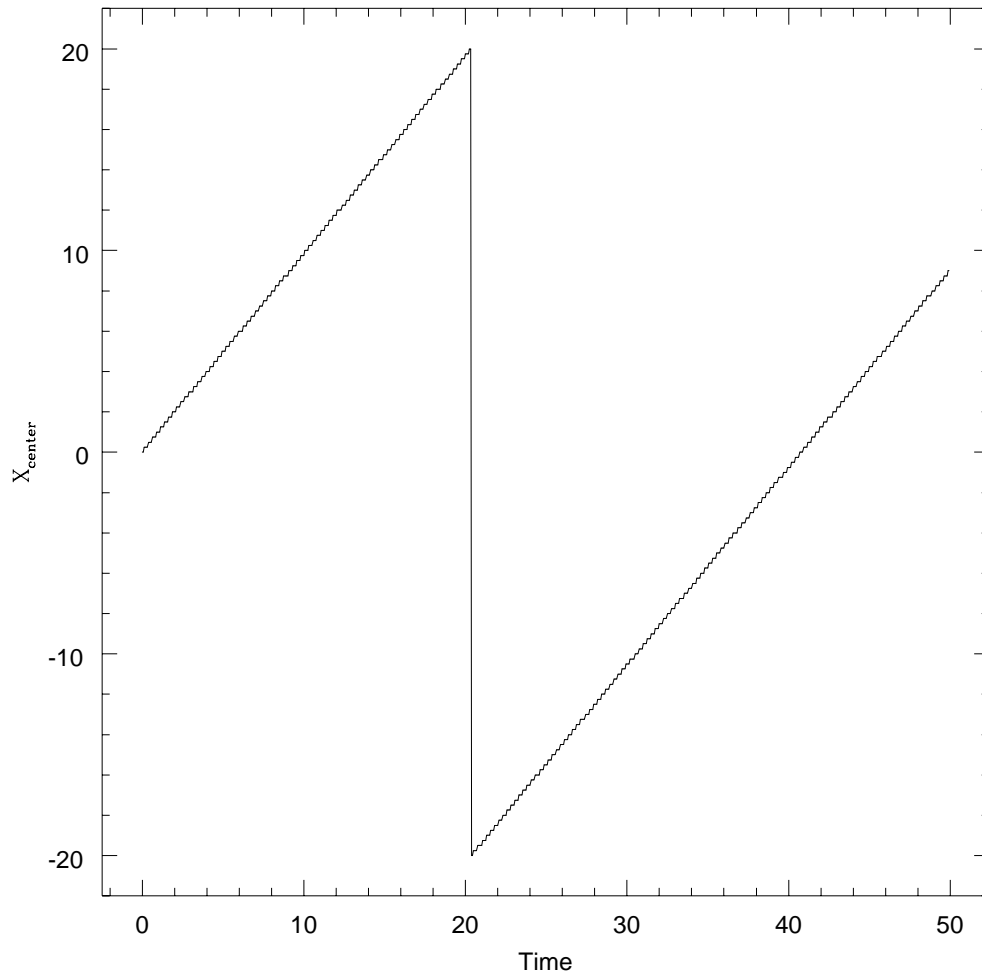
Figure 4.5: This figure shows the location of the center-of-mass of the boson star as a function of time. Periodic boundary conditions are used, with $x = -20$ and $x = 20$ identified. The initial momentum is $p_x = 1.0$. The boson star passes through the "boundary" at $t \sim 20$. $\Delta x = \Delta y = 0.25$, $\Delta t = 0.0625$, and the computational domain is $[-20, 20] \times [-20, 20]$.
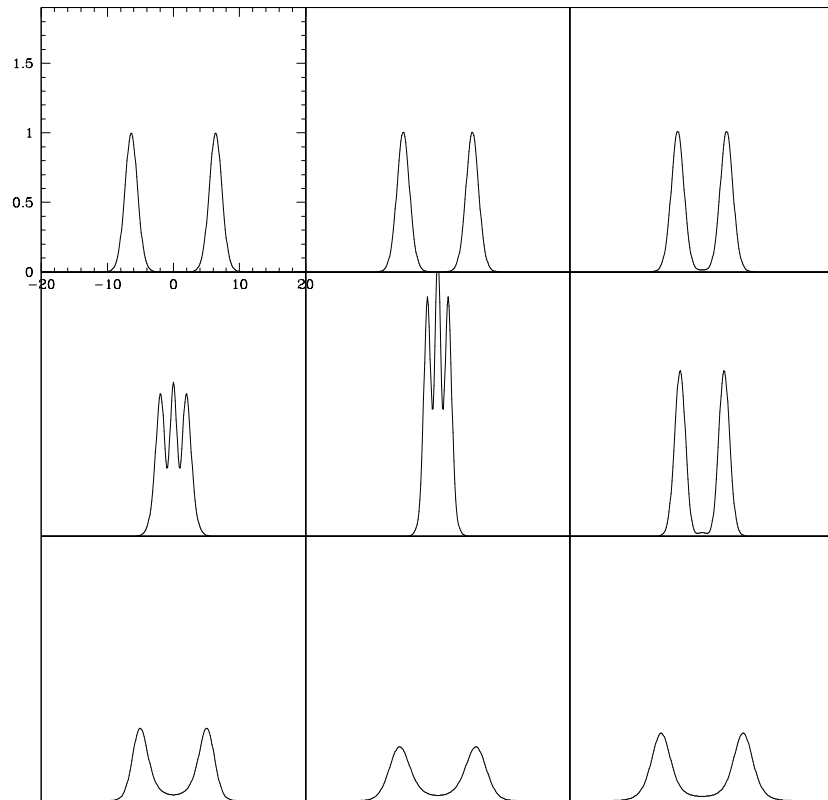
Figure 4.6: Binary boson stars– head-on collision: Time evolution of the density along the x-axis. $\Delta x = \Delta y \simeq 0.1429$, $\Delta t \simeq 0.0357$, and the computational domain is $[-64, 64] \times [-64, 64]$.
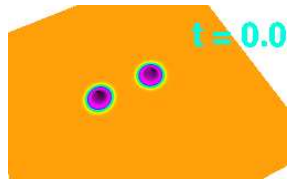
Figure 4.7: Binary star coalescence: Time evolution, $t = 0$
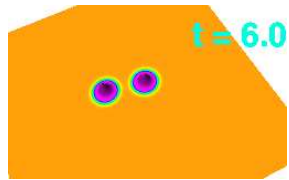
Figure 4.8: Binary star coalescence: Time evolution, $t = 6$
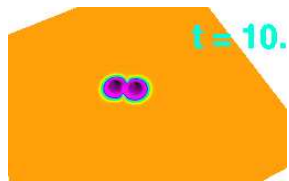
Figure 4.9: Binary star coalescence: Time evolution, $t = 10$
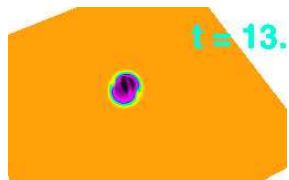
Figure 4.10: Binary star coalescence: Time evolution, $t = 13$
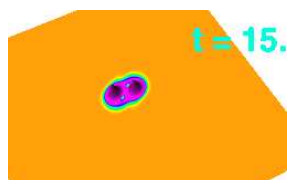
Figure 4.11: Binary star coalescence: Time evolution, $t = 15$
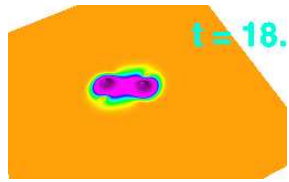
Figure 4.12: Binary star coalescence: Time evolution, $t = 18$
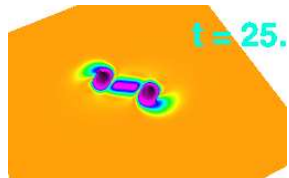
Figure 4.13: Binary star coalescence: Time evolution, $t = 25$
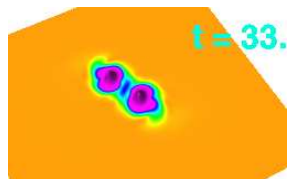
Figure 4.14: Binary star coalescence: Time evolution, $t = 33$
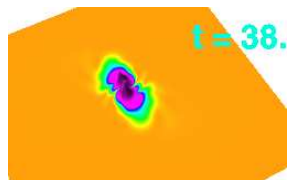
Figure 4.15: Binary star coalescence: Time evolution, $t = 38$
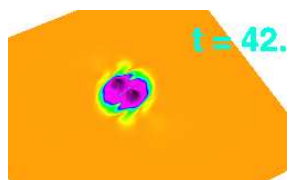
Figure 4.16: Binary star coalescence: Time evolution, $t = 42$
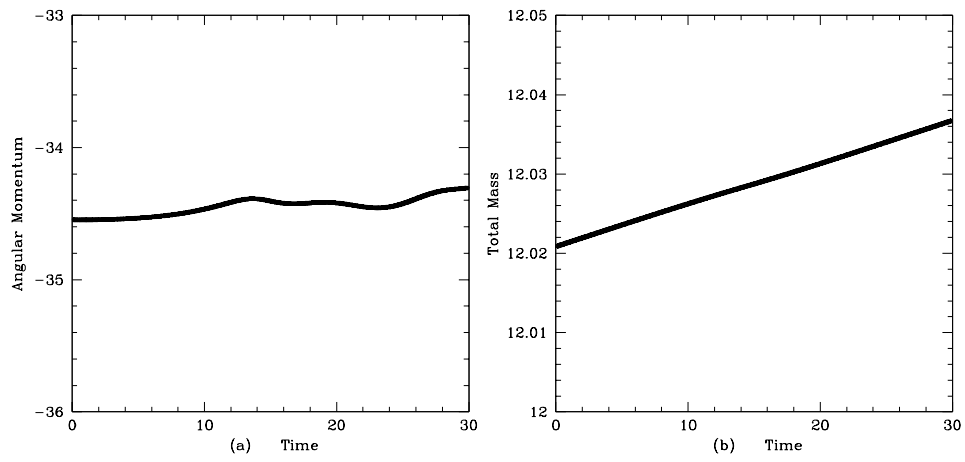
Figure 4.17: This figure shows time evolutions of (a) angular momentum and (b) total mass for a binary star coalescence. $\Delta x = \Delta y = 0.125$, $\Delta t = 0.03125$, and the computational domain is $[-48, 48] \times [-48, 48]$.
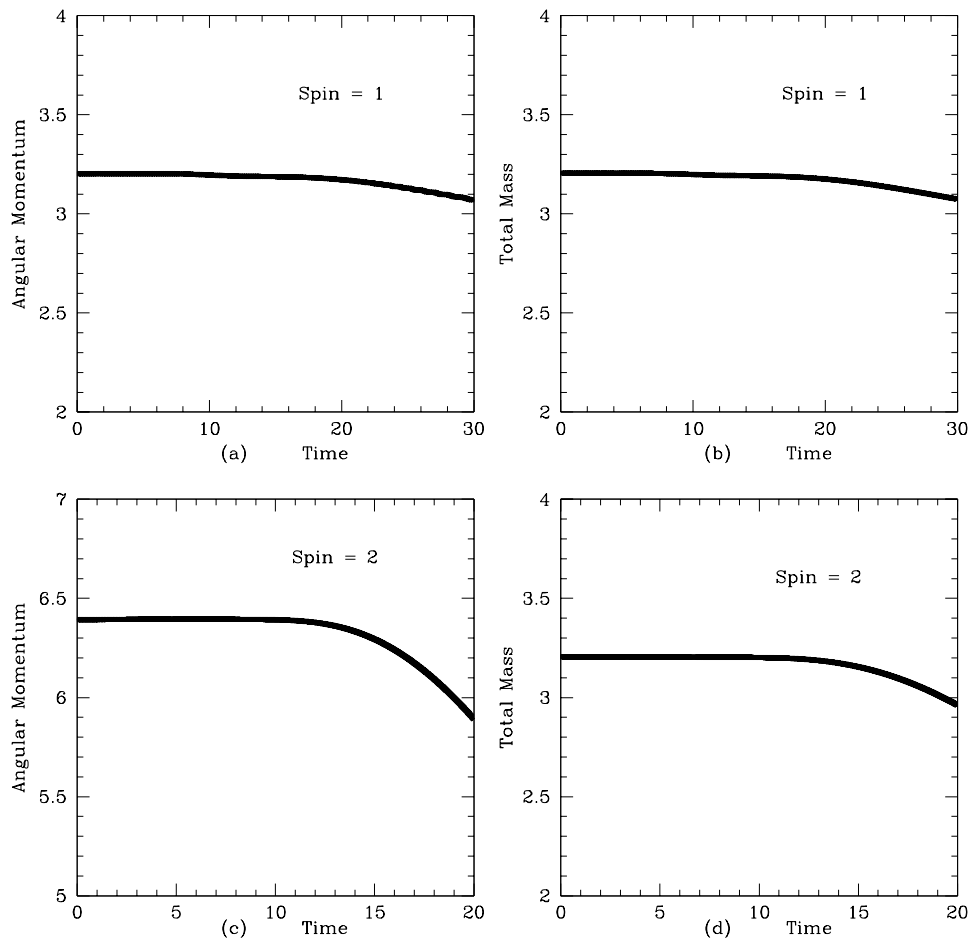
Figure 4.18: This figure shows time evolutions of a spinning boson star with a spin $S = 1$ (a),(b) and $S = 2$ (c), (d). For (a) & (b), $\Delta x = \Delta y \simeq 0.083$, $\Delta t \simeq 0.04167$, and the computational domain is $[-32, 32] \times [-32, 32]$. For (c) & (d), $\Delta x = \Delta y \simeq 0.0893$, $\Delta t \simeq 0.02232$, and the computational domain is $[-40, 40] \times [-40, 40]$.
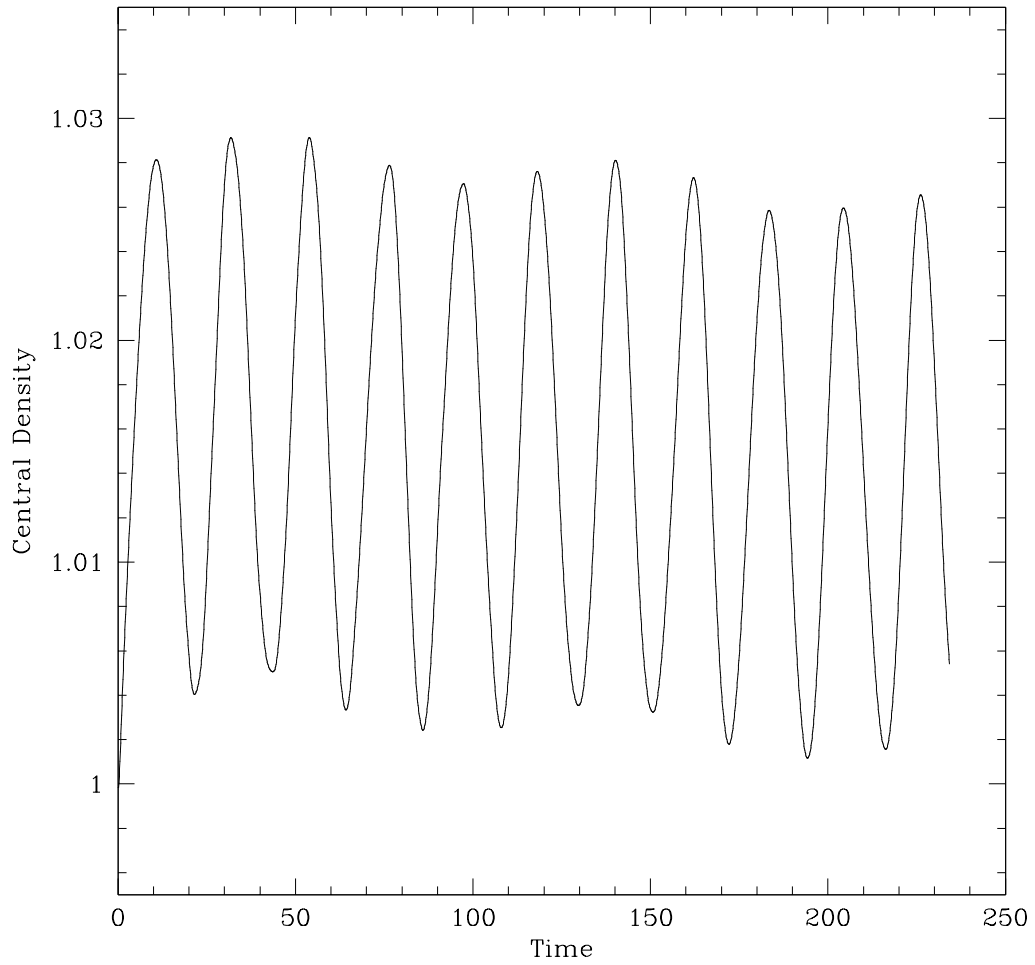
Figure 4.19: Time evolution of a single axisymmetric stationary boson star. For this run, $\Delta\rho = \Delta z = 0.15625$, $\Delta t = 0.0234375$, and the computational domain is $[0, 20] \times [-20, 20]$.
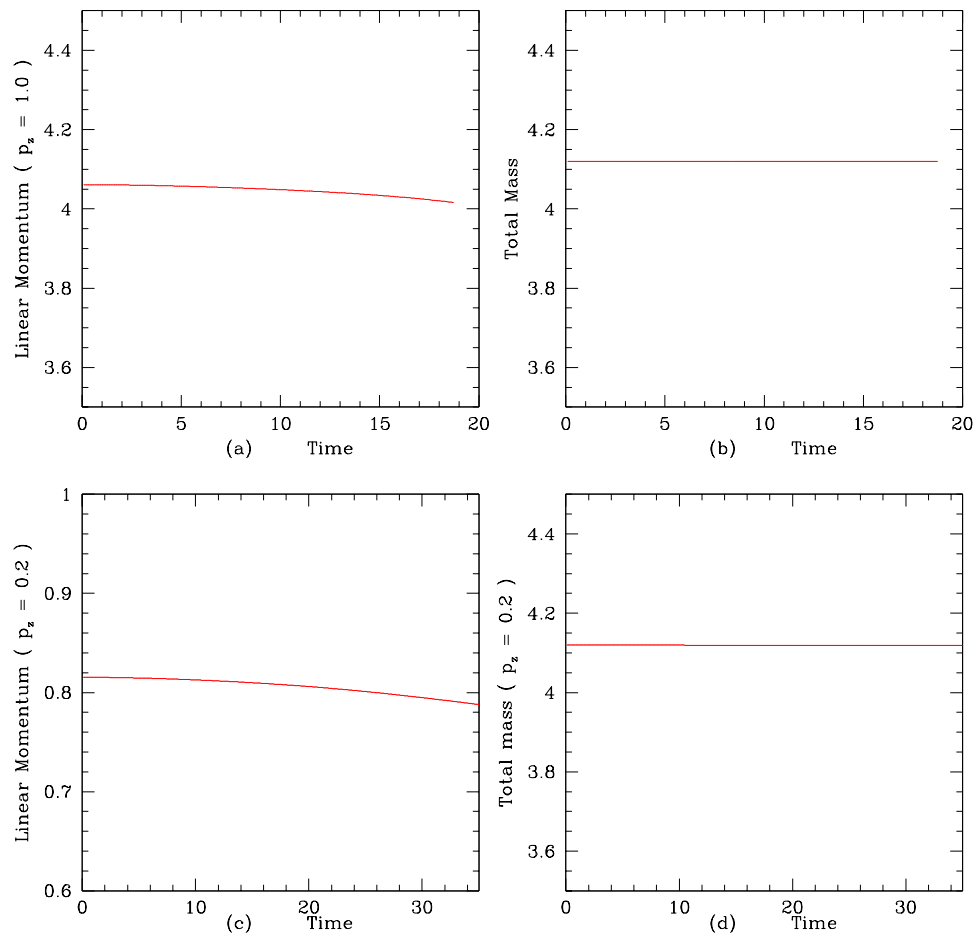
Figure 4.20: Time evolutions of linear momentum and total mass for a boson star moving along the z-axis. For these runs, $\Delta\rho = \Delta z = 0.15625$, $\Delta t = 0.0234375$, and the computational domain is $[0, 30] \times [-30, 30]$.
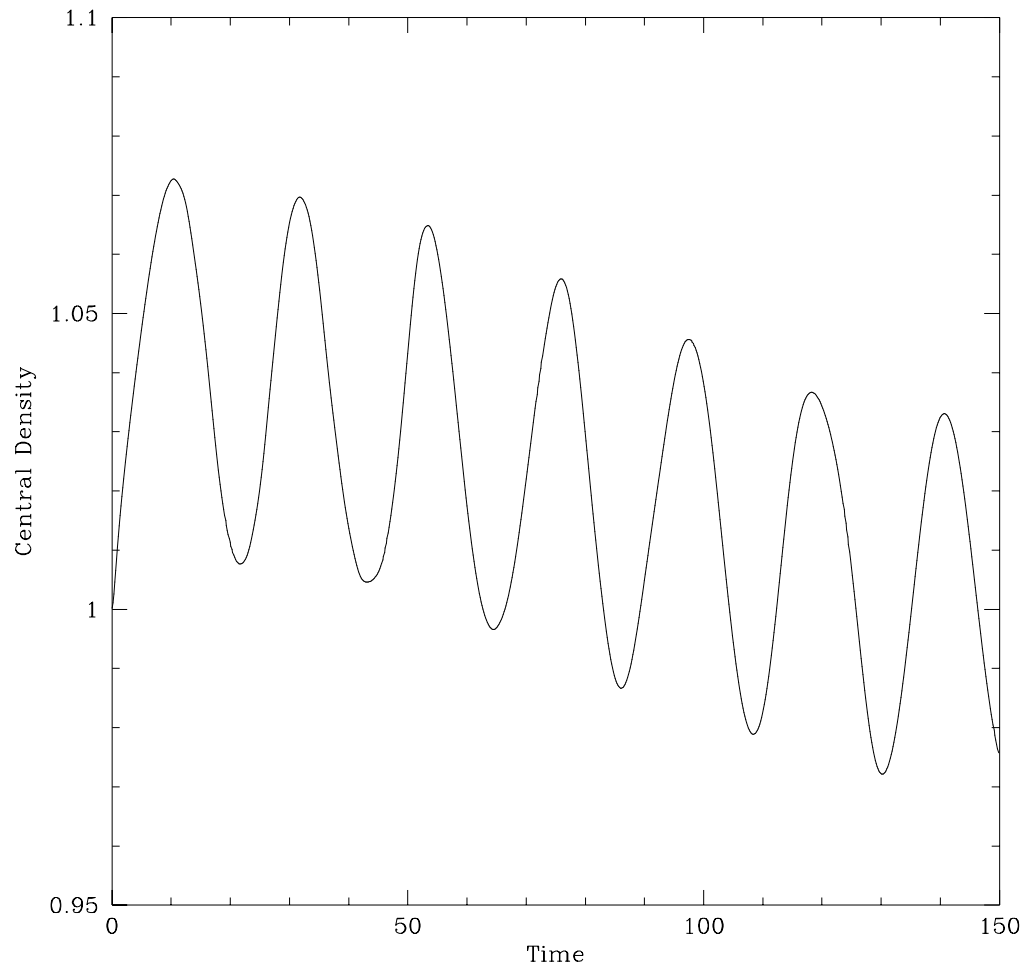
Figure 4.21: This figure shows a central density, ϕ_0^2, of a 3D stationary boson star as a function of time.
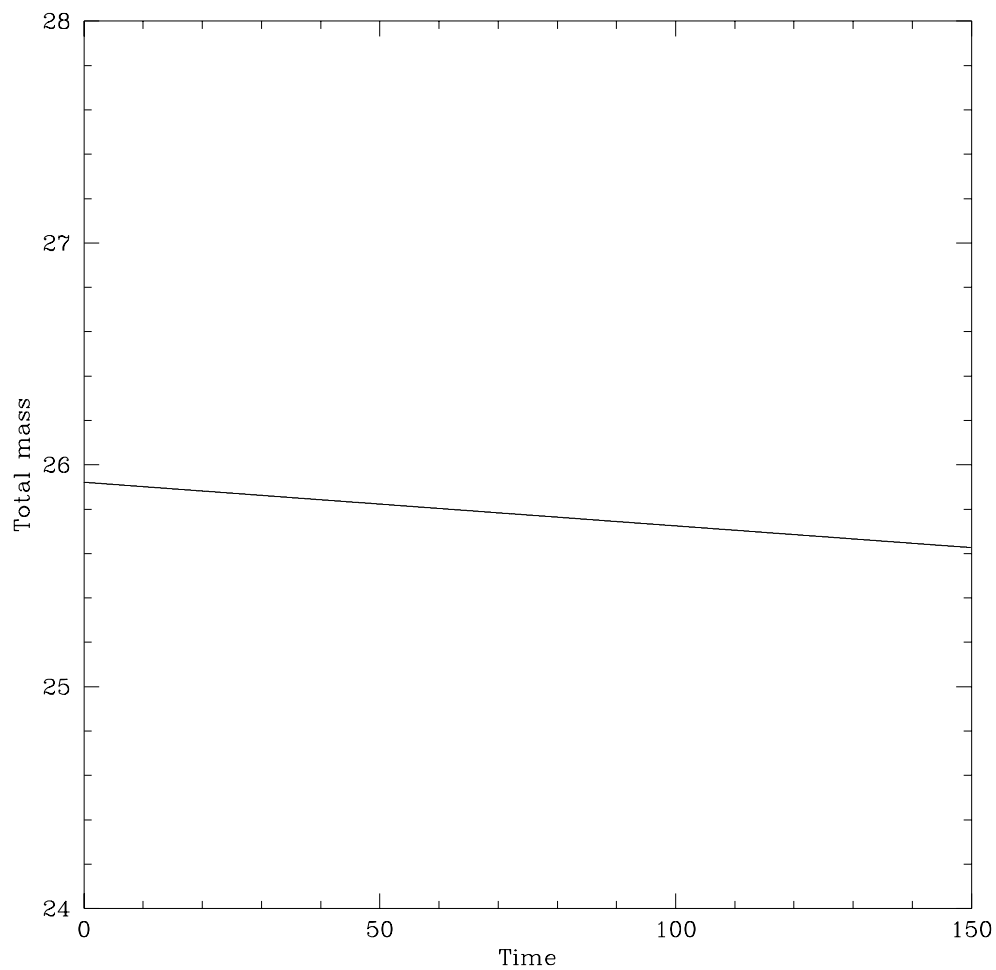
Figure 4.22: This figure shows the total mass of a 3D stationary boson star as a function of time from the run described in Fig. 4.21.
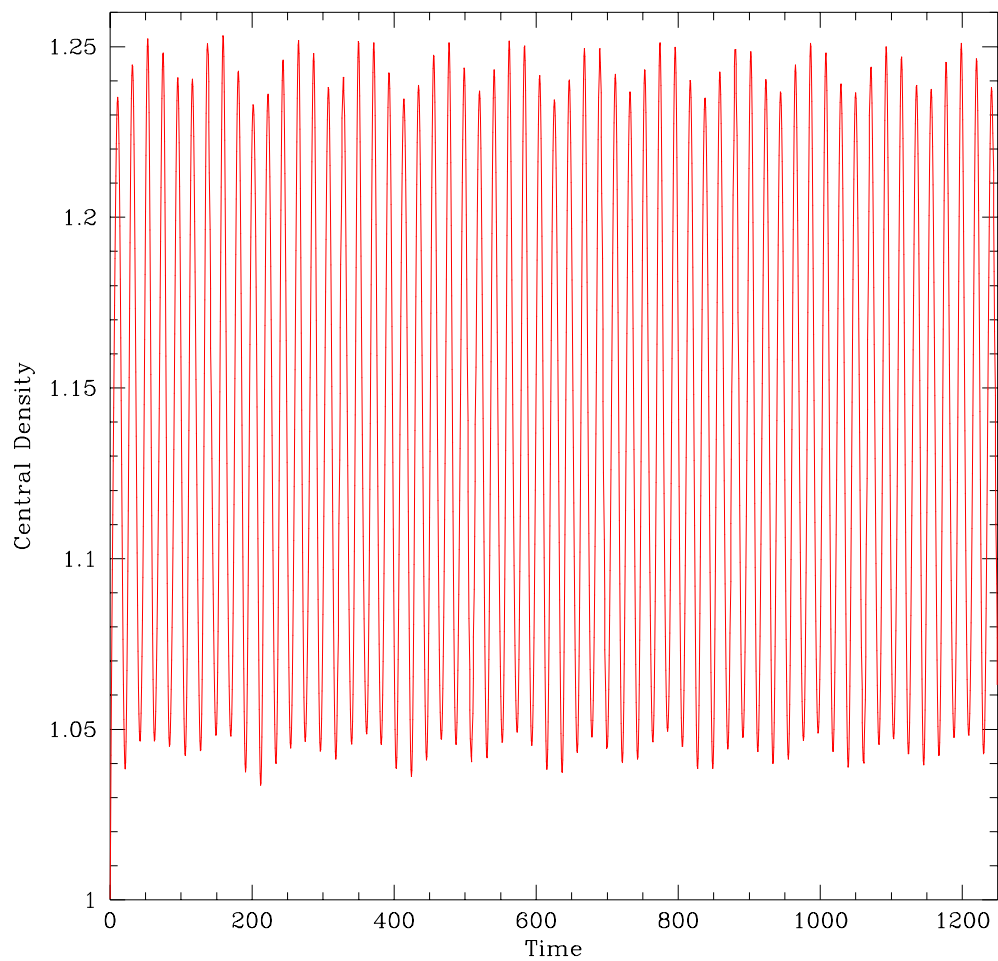
Figure 4.23: This figure shows a long time evolution of a single stationary boson star. For this run, $\Delta x = \Delta y = \Delta z = 0.5$, $\Delta t = 0.125$, and the computational domain is $[-16, 16] \times [-16, 16] \times [-16, 16]$.
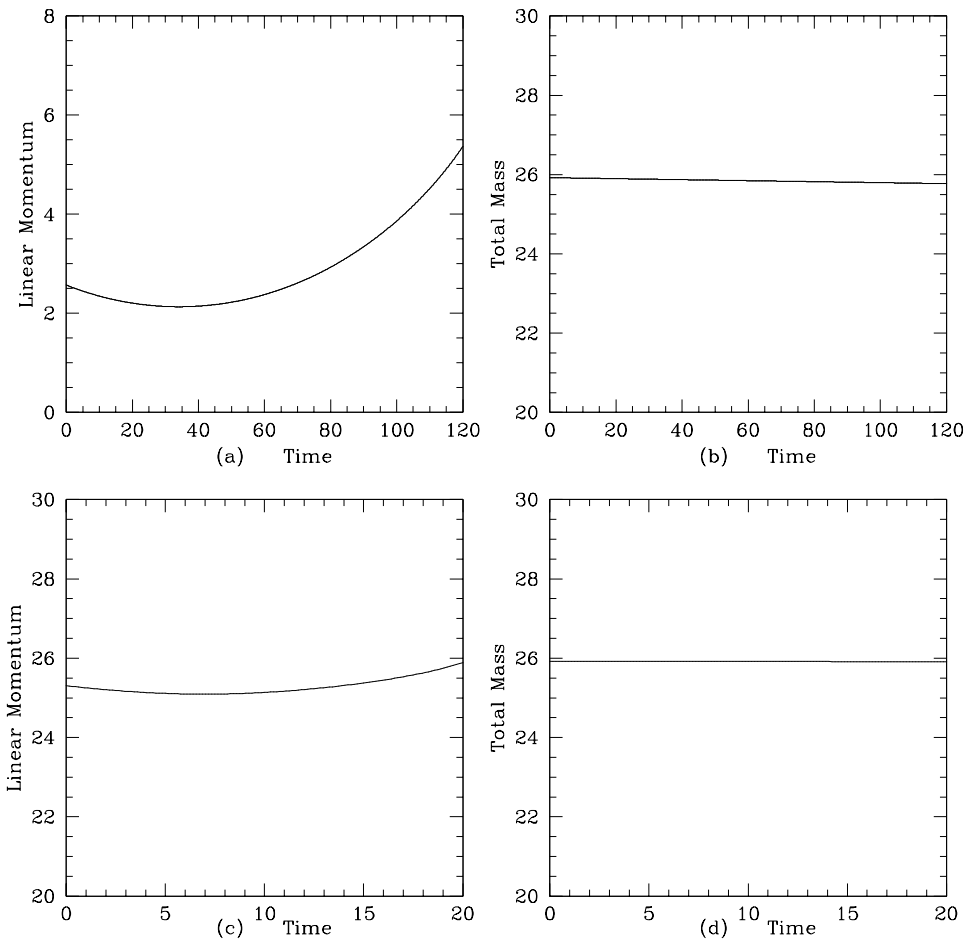
Figure 4.24: This figure shows the linear momenta, (a) & (c), and the total mass, (b) & (d) as a function of time for a 3D moving boson star with initial momenta $v_x = 0.1$ for (a) & (b) and $v_x = 1.0$ for (c) & (d). Total mass is conserved well over the course of the evolution. For these runs, $\Delta x = \Delta y = \Delta z = 0.3125$, $\Delta t = 0.15625$, and the computational domain is $[-20, 20] \times [-10, 10] \times [-10, 10]$.
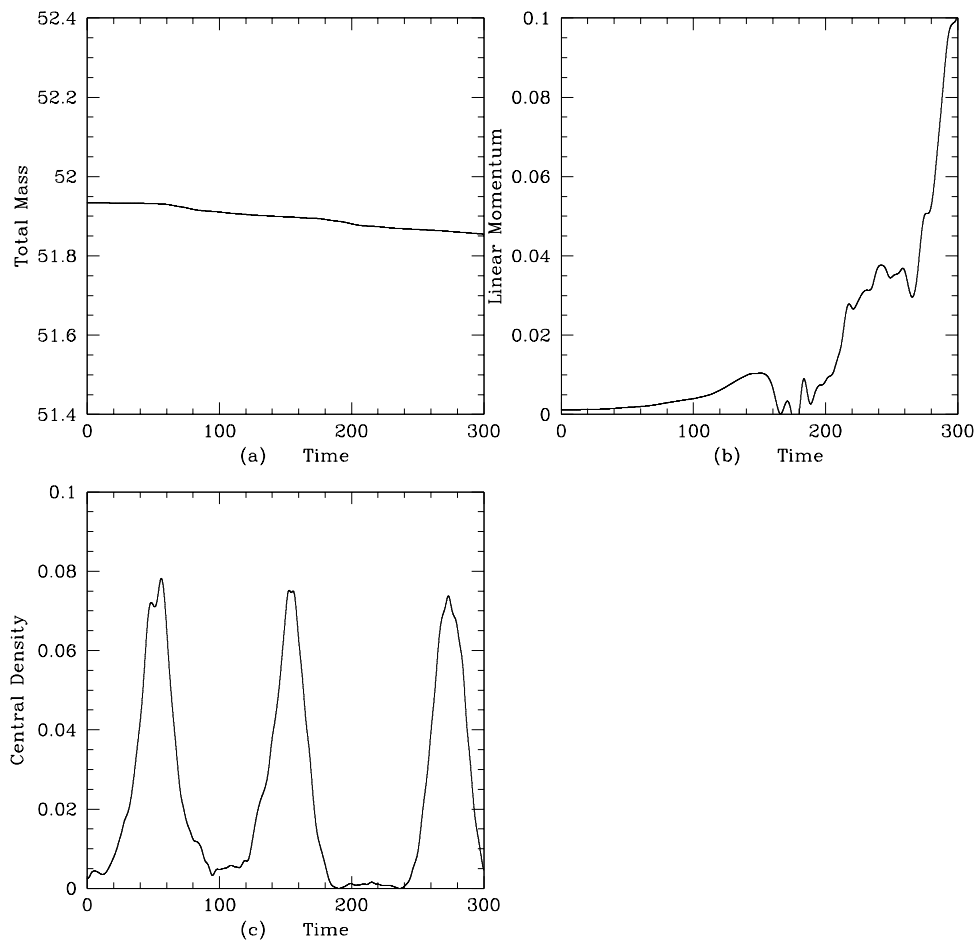
Figure 4.25: This figure shows (a) total mass, (b) linear momentum, in x-direction and (c) central density, ϕ_0^2, for a 3D binary boson star coalescence. The stars are initially located at $(x_1, y_1, z_1) = (-5.25, 0, 0)$ and $(x_2, y_2, z_2) = (5.25, 0, 0)$ with linear momenta $p_1 = (0, 0.3, 0)$ and $p_2 = (0, -0.3, 0)$, respectively. Computational parameters are $\Delta x = \Delta y = \Delta z = 0.4$, $\Delta t = 0.1$, and the computational domain is $[-16, 16] \times [-16, 16] \times [-16, 16]$.
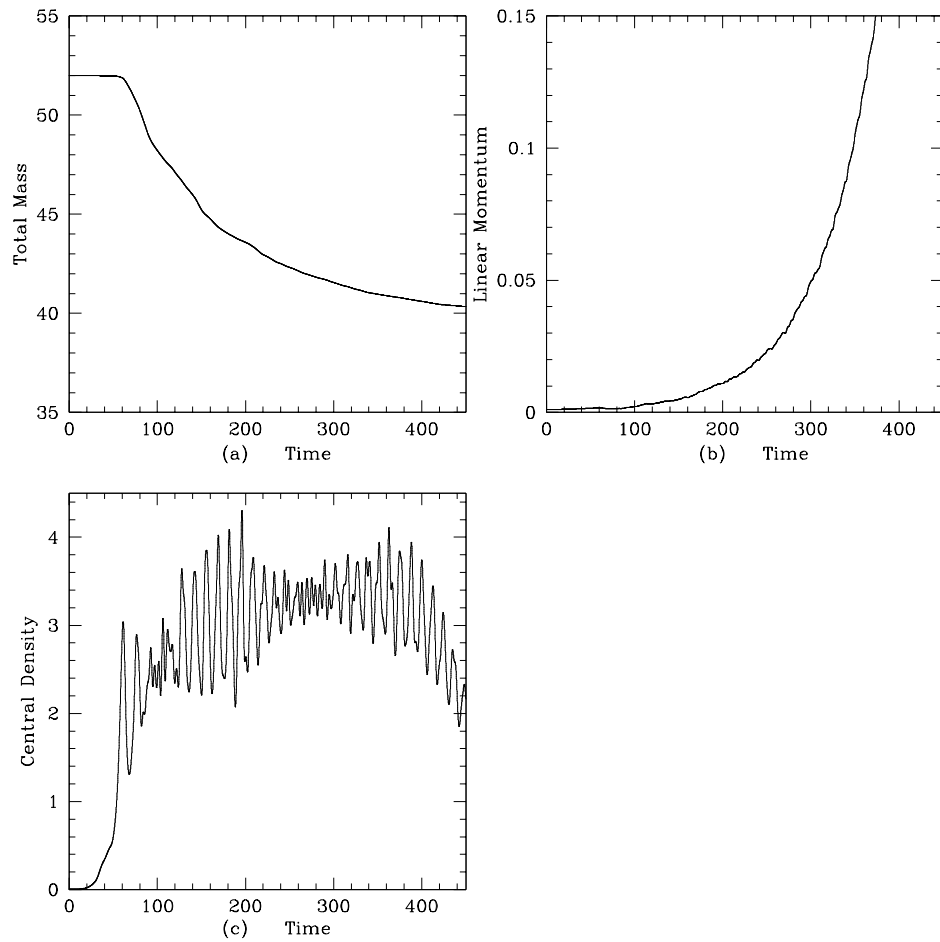
Figure 4.26: This figure shows (a) total mass, (b) linear momentum in x-direction, and (c) central density, ϕ_0^2, for a 3D binary boson star merger. The stars are located initially at $(x_1, y_1, z_1) = (-5.0, 0, 0)$ and $(x_2, y_2, z_2) = (5.0, 0, 0)$ with linear momenta $p_1 = (0, 0.3, 0)$ and $p_2 = (0, -0.3, 0)$, respectively. $\Delta x = \Delta y = \Delta z = 0.4$, $\Delta t = 0.1$, and the computational domain is $[-16, 16] \times [-16, 16] \times [-16, 16]$.

Chapter 5

Boson Stars in General Relativity

5.1 Introduction

As mentioned in the introduction to the Chapter 4, even though there have been no elementary scalar fields observed in nature to date, a resurgence of interest from particle physics and quantum cosmology has provided renewed motivation for the study of the physics of scalar fields in the context of general relativity. I can think of examples from Higgs bosons [48], inflatons, bosonic dark matter, etc [25].

Boson stars provide also provide an excellent numerical laboratory to study strong gravitational fields. Here it should be noted that most current work in 3D numerical relativity involves black hole spacetimes. However, the singularity residing inside the event horizon of a black hole spacetime presents tremendous challenges for simulation. To date, there have been two strategies to deal with these physical singularities. The "old" way to avoid a singularity is to use singularity-avoiding slicing conditions which may penetrate or asymptote to apparent or event horizons. Most previous calculations in numerical relativity have used this strategy. For example, the maximal slicing condition slows down the evolution around the physical singularity, and prevents the spacelike hypersurfaces from intersecting the singularity. But "freezing out" the evolution around the singularity eventually introduces coordinate singularities, and thus long-term evolution of black hole spacetimes with such conditions is essentially fruitless. The "new" way to deal with a singularity is to "excise" the blackhole interiors since, by definition, the blackhole interior can not influence the exterior [49]. This technique has been used in the study of blackhole-scalar field interactions in spherical symmetry [50] and Einstein-Yang-Mills collapse [51] producing new results which were unattainable with the old strategy. In 3D, stable evolution has been achieved in characteristic evolution of a single blackhole spacetime with excising techniques. [52]. However, since boson stars are, by definition, nonsingular compact objects, I can at least avoid problems arising from the horizon boundary as long as no black hole forms.

Boson stars may have lesser astrophysical importance than black holes and neutron stars at the moment as sources of gravitational radiation, but they may be used as

model systems to study the detailed nature of gravitational waveforms. For example, Wilson, Mathews and Marronetti recently claimed that their simulation of binary neutron stars using an approximation to full GR shows that the individual neutron stars collapse to black holes prior to merger [54, 55, 56, 57]. Their claim has been disputed by several researchers utilizing a variety of approximate analytical and numerical techniques [58, 59, 60], and the results remain controversial in the astrophysics community [61]. Therefore, it would be very interesting to study the equivalent problem in a fully relativistic boson star code.

Boson stars also provide an excellent system to implement and evaluate various coordinate conditions in the context of 3D numerical relativity, as well as for the development of multi-dimensional AMR techniques.

The first significant work on boson stars was due to Ruffini and Bonazzola, and came out in 1969 [8]. They calculated equilibrium states of both Newtonian and relativistic boson stars. In 1986, Colpi *et al* [9] studied boson stars with $\lambda\phi^4$ self-interaction, and showed that the self-interacting stars could have a mass comparable to neutron stars. The first published study of the dynamics of relativistic boson stars was due to Suen and Seidel [14] in 1990. These authors computed dynamical evolutions of perturbed boson stars in spherical symmetric in order to study their stability. Here I am trying to accomplish dynamical evolutions of 3D boson stars by using a fully general 3D numerical relativity code.

5.2   Equation of Motion

General-relativistic boson stars are described by the Einstein-Klein-Gordon equation:

$$g^{\mu\nu}\phi_{;\mu\nu} - m^2\phi = 0 \tag{5.1}$$

$$G^{\mu\nu} = R^{\mu\nu} - \frac{1}{2}g^{\mu\nu}R = 8\pi G T^{\mu\nu} \tag{5.2}$$

where the stress energy tensor $T^{\mu\nu}$ for a massive complex scalar field is given by

$$T^{\mu\nu} = \frac{1}{2}(\phi^{*,\mu}\phi^{,\nu} + \phi^{,\mu}\phi^{*,\nu}) - \frac{1}{2}g^{\mu\nu}(\phi^*_{,\lambda}\phi^{,\lambda} + m^2|\phi|^2) \tag{5.3}$$

To evolve the geometric variables, I use the ADM code developed collaboratively by the Binary Black Hole Grand Challenge Alliance [62]; to this code I have added my own routines for the Klein-Gordon equation. This ADM-scalar code uses a Cartesian-like coordinate system, (t, x, y, z).

The "3+1" equations of motion for the geometric variables are

$$\partial_t g_{ij} = -2\alpha K_{ij} + D_i\beta_j + D_j\beta_i \tag{5.4}$$

$$\partial_t K_{ij} = -D_i D_j\alpha + \alpha(R_{ij} + K K_{ij} - 2K_{il}K^l{}_j) + \mathcal{L}_\beta K_{ij}$$
$$-8\pi\alpha(S_{ij} - \frac{1}{2}g_{ij}(S - \rho)) \tag{5.5}$$

where

$$\rho = \alpha^2 \phi^{*,t}\phi^{,t} + \frac{1}{2}(\phi^*_{,\lambda}\phi^{,\lambda} + m^2|\phi|^2) \tag{5.6}$$

$$j^i = \frac{\alpha}{2}(\phi^{*,t}\phi^{,i} + \phi^{,t}\phi^{*,i} - g^{ti}(\phi^*_{,\lambda}\phi^{,\lambda} + m^2|\phi|^2)) \tag{5.7}$$

$$S_{ij} = \frac{1}{2}(\phi^*_{,i}\phi_{,j} + \phi_{,i}\phi^*_{,j}) - \frac{1}{2}g_{ij}(\phi^*_{,\lambda}\phi^{,\lambda} + m^2|\phi|^2) \tag{5.8}$$

$$\text{tr}S = -\frac{3}{2}\phi^*_{,t}\phi^{,t} - \frac{1}{2}\phi^*_{,i}\phi^{,i} - \frac{3}{2}(m^2|\phi|^2) \tag{5.9}$$

Introducing auxiliary scalar field variables, Φ_i, Π, defined by

$$\Phi_i = \frac{\partial\phi}{\partial x_i} \tag{5.10}$$

$$\Pi = \frac{\sqrt{h}}{\alpha}(\partial_t - \beta^i\partial_i)\phi \tag{5.11}$$

the equation of motion for the scalar field can be written in the first-order-in-time form:

$$\Pi_{,t} - \beta^i\Pi_{,i} = \beta^i_{,i}\Pi + (\alpha\sqrt{h}h^{ij}\Phi_j)_{,i} - \alpha\sqrt{h}m^2\phi \tag{5.12}$$

$$\Phi_{i,t} - \beta^j\Phi_{j,i} = (\frac{\alpha}{\sqrt{h}}\Pi)_{,i} + \beta^j_{,i}\Phi_j \tag{5.13}$$

$$\phi_{,t} - \beta^i\phi_{,i} = \frac{\alpha}{\sqrt{h}}\Pi \tag{5.14}$$

Eqns. (5.4), (5.5), (5.12), (5.13), and (5.14) are evolved with an iterative Crank-Nicholson scheme as outlined in Section (3.1). It usually took 4-5 CN iterations to drive the residuals down to 10^{-8} for a single stationary star run.

5.3   Initial Value Problem

In this Section, I will briefly review initial value problems in 3D and describe how to set up a single stationary boson star initial data in spherical symmetry.

In the "3+1" formalism, there are 12 dynamical variables, $\{g_{ij}, K_{ij}\}$ and 4 constraint equations, $G_{\mu 0} = 8\pi T_{\mu 0}$—the constraints do not involve second time derivatives of g_{ij}. The initial value problem consists of determining which 8 out of 12 variables are freely specifiable and solving for the remaining 4 variables by solving 4 constraint equations.

In principle, (and often in practice), it is possible to specify any 8 variables. However, York's prescription for the initial value problem [28] does have the nice property that we know that it leads to an elliptic set of equations for which proofs of existence of a unique solution exist.

In York's approach, the freely specified data on the initial hypersurface is $\hat{g}_{ij}$ the conformal metric and E^*_{ij} the transverse-traceless part of the extrinsic curvature tensor. $\hat{g}_{ij}$

and E^*_{ij} are related to g_{ij} and K_{ij} by:

$$
\begin{aligned}
g_{ij} &= \psi^4 \hat{g}_{ij} & (5.15) \\
K^{ij} &= \psi^{-10} \hat{K}^{ij} \\
&= \psi^{-10} \hat{E}^{ij} + \frac{1}{3}\psi^{-4}\mathrm{tr}K\hat{g}^{ij} \\
&= \psi^{-10}[\hat{E}^{*ij} + (\hat{l}W)^{ij}] + \frac{1}{3}\psi^{-4}\mathrm{tr}K\hat{g}^{ij} & (5.16)
\end{aligned}
$$

where

$$
(\hat{l}W)^{ij} \equiv \hat{\nabla}^i W^j + \hat{\nabla}^j W^i - \frac{2}{3}\hat{g}^{ij}\hat{\nabla}_k W^k \tag{5.17}
$$

The conformal factor ψ and W^i satisfy the transformed constraint equations,

$$
8\hat{\Delta}\psi = \hat{R}\psi + \frac{2}{3}\psi^5(\mathrm{tr}K)^2 - \psi^{-7}\hat{E}_{ij}\hat{E}^{ij} - 16\pi\hat{\rho}\psi^{-3} \tag{5.18}
$$

$$
(\hat{\Delta}_l W)^i = \frac{2}{3}\psi^6\hat{\nabla}^i\mathrm{tr}K + 8\pi\hat{j}^i - \hat{\nabla}_j\hat{E}^{*ij} \tag{5.19}
$$

where $\hat{\Delta}$ is the Laplacian operator computed using the conformal metric and $(\hat{\Delta}_l W)^i \equiv \hat{\nabla}_j(lW)^{ij} = (\hat{\Delta}W)^i + \frac{1}{3}\hat{\nabla}^i(\hat{\nabla}_j W^j) + \hat{R}^i_j W^j$, where $(\hat{\Delta}W)^i \equiv \hat{\nabla}^j\hat{\nabla}_j W^i$. $\hat{R}_{ij}$ is the Ricci tensor associated with $\hat{g}_{ij}$ and $\hat{R} = \hat{g}^{ij}\hat{R}_{ij}$.

York also suggests that matter terms in a conformal form be related to physical ones by

$$
\rho = \psi^{-8}\hat{\rho} \tag{5.20}
$$

$$
j^i = \psi^{-10}\hat{j}^i \tag{5.21}
$$

This ensures that, for all $\psi > 0$, certain energy conditions will be satisfied by the physical matter variables, if they are satisfied by the conformal variables [28].

However, I have not found it necessary to conformally transform my matter variables. Instead, I propose the following method to set up an initially moving boson star. First, I will assume the initial slice is maximal, $\mathrm{tr}K = 0$, and will specify $\hat{g}_{ij} = \delta_{ij}$ and $E^*_{ij} = 0$. Then the constraint equations become

$$
8\hat{\Delta}\psi = -\psi^{-7}(\hat{l}W)_{ij}(\hat{l}W)^{ij} - 16\pi\hat{\rho}\psi^{-3} \tag{5.22}
$$

$$
(\hat{\Delta}_l W)^i = 8\pi\hat{j}^i \tag{5.23}
$$

For the Klein-Gordon field, I will multiply the stationary ϕ_{st} by $e^{ip\cdot x}$ where p is the initial momentum. I will then compute the physical ρ and j_i from the boosted field, $\phi_p = \phi_{st}e^{ip\cdot x}$. I can then calculate ψ and W^i by solving the Hamiltonian and momentum constraint equations, using the *physical* ρ and j_i. Therefore, using Eqns. (5.20) and (5.21), I will solve

$$
8\hat{\Delta}\psi = -\psi^{-7}(\hat{l}W)_{ij}(\hat{l}W)^{ij} - 16\pi\rho\psi^5 \tag{5.24}
$$

$$
(\hat{\Delta}_l W)^i = 8\pi j^i\psi^{10} \tag{5.25}
$$

Eqns. (5.23) and (5.23) can be further simplified:

$$(\hat{l}W)^{ij}(\hat{l}W)_{ij} = 2(\partial_i W^j)(\partial_i W^j) + 2(\partial_i W^j)(\partial_j W^i) - \frac{4}{3}(\partial_i W^i)(\partial_j W^j) \qquad (5.26)$$

$$(\hat{\Delta}_l W)^i = \partial_j \partial_j W_i + \frac{1}{3}\partial_i(\partial_j W_j) \qquad (5.27)$$

where lower and upper indices are the same because of conformal flatness, $\hat{g}_{ij} = \delta_{ij}$. Finally, I obtain,

$$4\partial_i^2 \psi + \psi^{-7}((\partial_i W^j)(\partial_i W^j) + (\partial_i W^j)(\partial_j W^i) - \frac{2}{3}(\partial_i W^i)^2) + 8\pi\rho\psi^5 = 0 \qquad (5.28)$$

$$\partial_j \partial_j W_i + \frac{1}{3}\partial_i(\partial_j W_j) - 8\pi\psi^{10}j^i = 0 \qquad (5.29)$$

I plan to implement and solve eqns. (5.28) and (5.29) using the multigrid (MG) method.

For a *distant* binary star system, I will use a similar prescription. I will add solutions for distinct stars assuming that the matter distributions for each star is sufficiently compact and well-separated from other stars.

Now, I will discuss how to set up a single stationary, spherically-symmetric ground-state boson star. The most general "3+1" metric in spherical symmetry is given by

$$ds^2 = (-\alpha^2 + a^2\beta^2)dt^2 + 2a^2\beta dt dr + a^2 dr^2 + b^2 r^2 d\Omega^2 \qquad (5.30)$$

I adopt York's conformal formalism and assume zero shift at all times, $\beta^i \equiv 0$. My base metric is flat, $\hat{g}_{ij} = \delta_{ij}$. Then I have a metric of the following form:

$$ds^2 = -\alpha(r)^2 dt^2 + \psi(r)^4(dr^2 + r^2 d\Omega^2) \qquad (5.31)$$

Making the following *ansatz* for the scalar field (consistent with staticity of the geometry)

$$\phi_{st}(r,t) = \phi(r)e^{-i\omega t} \qquad (5.32)$$

the equations of motion reduce to the following set of ODEs. Here $\{\psi, \Psi, \phi, \Phi, \alpha, A\}$ are functions of r only:

$$\psi' \equiv \Psi \qquad (5.33)$$

$$\Psi' = -\frac{2}{r}\Psi - 8\pi\frac{1}{8}(\psi\Phi^2 + \psi^5(\frac{\omega^2}{\alpha^2} + m^2)\phi^2) \qquad (5.34)$$

$$\phi' \equiv \Phi \qquad (5.35)$$

$$\Phi' = -(\frac{2}{r} + \frac{A}{\alpha} + \frac{2\Psi}{\psi})\Phi + \psi^4(m^2 - \frac{\omega^2}{\alpha^2})\phi \qquad (5.36)$$

$$\alpha' \equiv A \qquad (5.37)$$

$$A' = -(\frac{2}{r} + \frac{2\psi'}{\psi})A + 4\pi\psi^4\alpha(\frac{2\omega^2}{\alpha^2} - m^2)\phi^2 \qquad (5.38)$$

This set of ODEs forms a one-parameter family of *eigenvalue* problems. A convenient family parameter (analogous to central density for fluid stars) is the central field value $\phi(0) \equiv \phi_0$. For each ϕ_0, a regular solution of Eqns. (5.33) - (5.38) only exists for a specific $\omega = \omega_{\phi_0}$, which, I recall, is the intrinsic oscillation frequency of the complex Klein-Gordon field.

Typical profiles for $\phi(r)$, $\psi(r)$, and $\alpha(r)$ are shown in Fig. 5.1. The ADM mass M_{ADM} is defined at spatial infinity and given by, for example,

$$M_{\mathrm{ADM}} = -\frac{1}{2\pi} \int_S \nabla \psi(r) \cdot dS = -\frac{1}{2\pi} \int_V \nabla^2 \psi(r) dV \qquad (5.39)$$

and ψ is asymptotically given by

$$\psi(r) \simeq 1 + \frac{M_{\mathrm{ADM}}}{2r} + O(\frac{1}{r^2}) \qquad (5.40)$$

A plot of the ADM mass of a boson star, $M_{\mathrm{ADM}}(\phi_0)$ is shown in Fig. 5.2. Note that M_{ADM} reaches the maximum value, $M_{ADM} \sim 0.64$ at $\phi_0 = \phi_{\mathrm{M}} \simeq 0.08$. The curve in the Fig. 5.2 is in excellent agreement with the results in the literature [9, 14]. It is well known from the dynamical study of perturbed boson stars [14] that boson stars with $\phi_0 < \phi_{\mathrm{M}}$ are stable against weak perturbations, but stars with $\phi_0 > \phi_{\mathrm{M}}$ are unstable against them. In the evolutions displayed below, the initial data has been chosen well into the stable branch.

A plot of the ADM mass, $M_{\mathrm{ADM}}(\omega_{\phi_0})$, is shown in Fig. 5.3.

5.4 Coordinate Conditions

General relativity allows us the freedom to choose any coordinates to describe dynamics (general covariance). As discussed in Sec.2.3, in the "3+1" formalism, This coordinate freedom manifests itself in the lapse function, α, and shift vector, β^i. Careful choices of coordinate systems will be crucial for stable evolutions of black hole/neutron star/boson star spacetimes.

In this Section, I describe the maximal slicing and K-driver conditions.

The maximal slicing condition is one of most the commonly used prescriptions for fixing the lapse function, principally because maximal slicing condition has a property of "singularity avoidance" [63].

The maximal slicing condition maximizes the three volume of each of the spacelike hypersurfaces, as can be seen from the following analysis. Given a 3-volume V,

$$V = \int \sqrt{-^3g} d^3x \qquad (5.41)$$

the condition for maximal slicing is given by maximizing the 3-volume:

$$\delta V = 0 \qquad (5.42)$$

$$\delta \sqrt{-^3g} = 0 \qquad (5.43)$$

Assuming $\beta^i = 0$, I have, from the evolution equation for g_{ij},

$$K_{ij} = -\frac{1}{2\alpha}g_{ij,t} \tag{5.44}$$

Taking a trace, I get,

$$K = -\frac{1}{2\alpha}g^{ij}g_{ij,t} \tag{5.45}$$

$$\tag{5.46}$$

Now, using the identity,

$$\delta\sqrt{-g} = \frac{1}{2}\sqrt{-g}g^{\mu\nu}\delta g_{\mu\nu} \tag{5.47}$$

$$\tag{5.48}$$

I get,

$$-2\alpha K\delta t = g^{ij}\delta g_{ij} = 2\frac{\delta\sqrt{-^3g}}{\sqrt{-^3g}} \tag{5.49}$$

$$\tag{5.50}$$

Then, I get the maximal slicing condition,

$$\delta\sqrt{-^3g} = 0 \rightarrow K = g^{ij}K_{ij} = 0 \tag{5.51}$$

I impose the maximal slicing condition at all times by first choosing initial data such that

$$K(\vec{x}, 0) = 0 \tag{5.52}$$

and then imposing

$$\frac{\partial K(\vec{x}, t)}{\partial t} = 0 \tag{5.53}$$

By taking the trace of Eqn. (5.5) and using Hamiltonian constraint equation, Eqn. (2.21), we have

$$\partial_t K = -D^i D_i \alpha + \alpha(-K_{il}K^{li}) + 4\pi\alpha(S + \rho) + g^{ij}\mathcal{L}_\beta K_{ij} + (\partial_t g^{ij})K_{ij} \tag{5.54}$$

Using $K = 0$, $\partial_t K$, the maximal slicing condition becomes:

$$D^i D_i \alpha - \alpha(K_{ij}K^{ij} + 4\pi(S + \rho)) = 0 \tag{5.55}$$

Now, since

$$D^i D_i \alpha = g^{ij}\partial_i\partial_j\alpha - g^{ij}\Gamma^k_{ij}\partial_k\alpha \tag{5.56}$$

I must solve the following elliptic equation:

$$g^{ij}\partial_i\partial_j\alpha - g^{ij}\Gamma^k_{ij}\partial_k\alpha - \alpha(K_{ij}K^{ij} + 4\pi(S + \rho)) = 0 \tag{5.57}$$

The maximal solver was implemented using the multigrid (MG) technique and Robin boundary conditions. I first test the maximal solver with a slightly perturbed flat spacetime. Here I study an evolution of flat space with zero shift and an initial lapse which is close to, but not exactly, unity

$$\alpha(t = 0) = 1.0 + 0.001\exp[-(x^2 + y^2 + z^2)] \tag{5.58}$$

I evolve the initial data $g_{ij} = \delta_{ij}$ and $K_{ij} = 0$ forward with this lapse for just the first timestep, with the lapse subsequently determined by Eqn (5.57). Fig. 5.4 (a) shows time evolutions of the lapse, α. The lapse returns to unity almost after the first timestep, as it should. From this, one might expect a "healthy" evolution, i.e., g_{ij} and K_{ij} stabilize to the initial flat data. However, Fig. 5.4 (b) shows the evolution of a typical metric function, g_{xx} along the y axis. A "dip" in g_{xx} is developing—eventually this dip becomes too sharp to be resolved.

The reason for this development is attributed to the fact that the maximal condition I use does not actively reforce the condition $K = 0$. Rather, my maximal slicing condition imposes the condition,

$$\frac{\partial K}{\partial t} = 0 \tag{5.59}$$

That is, if α is perturbed at any time, making K_{ij} (and K) non-zero, the slicing condition Eqn. (5.57) cannot put K_{ij} (and K) back to zero. Rather, it preserves the perturbed K_{ij} (and K) throughout the evolution, as it should.

This phenomena of a secular drift in the flat spacetime model is very much problematic for the actual evolution of a full 3D GR systems involving highly nonlinear and dynamical fields.

The authors of the paper [64] have suggested the so-called "K-driver" slicing condition to cure this problem. This condition is designed to *drive* K back to zero when it is perturbed away from it. Consider the equation

$$\frac{\partial K}{\partial t} + cK = 0 \tag{5.60}$$

where c is a positive number of one's choice. If c is a constant in time, K is driven to zero in an exponential manner, $K \sim e^{-ct}$. By controlling c, one has control over the stability of the slicing. Eqn. 5.60 leads to a different elliptic equation for the lapse:

$$g^{ij}\partial_i\partial_j\alpha - g^{ij}\Gamma^k_{ij}\partial_k\alpha - \alpha(K_{ij}K^{ij} + 4\pi(S + \rho)) = cK \tag{5.61}$$

Fig. 5.5 shows results from the "perturbed flat-space" problem solved using the K-driver slicing condition. The secular drift observed previously is under control and K is actively driven to zero.

Although I use a zero shift condition $\beta^i = 0$ in this chapter, I will need to use more sophisticated conditions for binary problems. I will also discuss the effect of the K-driver coordinate condition for GR boson star runs in Section 5.6.

5.5 Boundary Conditions

In this Section, I discuss outer boundary conditions.

In a Cauchy problem such as that encountered in the 3+1 ADM formalism, one cannot compactify spatial grids. Thus, one has to put the boundary of the grids at some *finite* distance. Even though there are no physical boundary conditions at the boundary, one has to use some kind of boundary conditions which best represent the physical situation and minimizes unphysical effects.

I apply an outgoing wave condition [33] to update the Klein-Gordon fields at the boundary. Assuming the edge of computational grid lies far from the center of stars, I use the outgoing wave condition for flat massless scalar fields as a zeroth approximation. More sophisticated conditions will be tried later. This so-called massless Sommerfeld condition will work the best when the edge of the grid represents an almost flat spacetime. The boundary condition is given by

$$(r\phi)_{,t} + (r\phi)_{,r} = 0 \tag{5.62}$$

$$r\phi_{,t} + \phi + r\phi_{,r} = 0 \tag{5.63}$$

for sufficiently large r in a spherical coordinate system. In a Cartesian coordinate system,

$$x\phi_{,t} + \frac{x}{r}\phi + r\phi_{,x} = 0 \tag{5.64}$$

$$y\phi_{,t} + \frac{y}{r}\phi + r\phi_{,y} = 0 \tag{5.65}$$

$$z\phi_{,t} + \frac{z}{r}\phi + r\phi_{,z} = 0 \tag{5.66}$$

I use analogous formulae for Π since $\phi_{,t} \sim \Pi$ far away from the stars.

$$\phi_{,t} \sim \Pi \tag{5.67}$$

$$x\Pi_{,t} + \frac{x}{r}\Pi + r\Pi_{,x} = 0 \tag{5.68}$$

$$y\Pi_{,t} + \frac{y}{r}\Pi + r\Pi_{,y} = 0 \tag{5.69}$$

$$z\Pi_{,t} + \frac{z}{r}\Pi + r\Pi_{,z} = 0 \tag{5.70}$$

For spatial derivatives, the expressions get a little bit complicated. For example, the conditions for Φ_x are given by:

$$x\Phi_{x,t} + r\Phi_{x,x} + \frac{2x}{r}\Phi_x + \Pi + (\frac{1}{r} - \frac{x^2}{r^3})\phi = 0 \tag{5.71}$$

$$y\Phi_{x,t} + r\Phi_{x,y} - \frac{2xy}{r^3}\phi + \frac{y}{r}\Phi_x - \frac{xy}{r^2}\Pi = 0 \tag{5.72}$$

$$z\Phi_{x,t} + r\Phi_{x,z} - \frac{2xz}{r^3}\phi + \frac{z}{r}\Phi_x - \frac{xz}{r^2}\Pi = 0 \tag{5.73}$$

One can get expressions for Φ_y and Φ_z by the cyclic permutation, $x \to y \to z$.

To finite-difference the above equations I use backward-time-one-sided-space stencils. For a single stationary star initial data, this condition gives a stable evolution. Testing with more general initial data such as that for binary star coalescence will be carried out in the future.

From my short experience with full 3D GR simulations, I learned that finding a stable outer boundary condition (OBC) for geometry variables, namely, the metric, g_{ij}, and the extrinsic curvature, K_{ij} is a highly nontrivial task [65].

Many different OBCs for 3D "3+1" general relativity have been suggested and tested (mostly for simple model problems). Some techniques show promising test results and hold out hope for a stable evolution in a realistic full 3D evolution, others are still plagued by instability [65]. Here I test two OBCs: the Sommerfeld condition given above, and a blending boundary condition [66, 67].

The (standard) interpolated Sommerfeld boundary condition computes K_{ij} at the boundary by enforcing the condition:

$$(\partial_t + \partial_r + \frac{a}{r})K_{ij} = 0 \tag{5.74}$$

where a is the falloff power of r, i.e., $K_{ij} \sim r^{-a}$. I used $a = 2$ for all my calculations.

The basic idea of a blending boundary condition is to blend the numerical solution with another one in a finite volume rather than only on the surface. (Note that sponge filters [37], long known to the numerical relativity community operate in the same spirit.) I have used a simple-minded Dirichlet blending condition: all components of K_{ij} are smoothly blended to the flat spacetime. For example, for the last n grid points where n is usually larger than 4, I set the extrinsic curvature to a linear combination of the evolved value and a fixed (Dirichlet) boundary value. Thus:

$$K_{ij} = (1 - a(r))K_{ij,\text{computed}} + a(r)K_{ij,\text{fixed}} \tag{5.75}$$

where $a = 0$ in the interior inside n grid points from the boundary and goes smoothly to 1 in the boundary layer. $K_{ij,\text{fixed}}$ is set to zero.

In the current ADM implementation,

$$a(r) = (\frac{r - R_0}{r_{\max} - R_0})^q \tag{5.76}$$

for $R_0 < r < r_{\max}$, where $R_0 = r_{\max} - n \times h$ and n is the number of blending zones. It is found from the blackhole runs that $q = 1$ is optimal for such small domains.

In the future, I am going to test perturbative boundary conditions [65] such as a pure perturbative OBC, a perturbative sommerfeld OBC, and a perturbative blending OBC. The perturbative OBCs is proposed to perform a stable evolution around outer boundaries and to simultaneously provide for extraction of gravitational waveforms.

5.6 Evolution: Stationary Stars

In this Section, I show some of the preliminary evolutions of a single stationary boson star. The code is currently unstable and the sources of this instability are not clear at this point. My current suspicion is that the outer boundary module for the extrinsic curvature may give rise to some troubles, but more careful test runs are needed to figure out the exact cause(s) of instability. Note that for all the runs I present here, the Klein-Gordon field remains smooth and compact throughout the evolutions and the MG solver for the maximal slicing condition generates a smooth lapse function.

Fig. 5.6 shows a typical profile of the lapse, α, for a single stationary star run. It remains stable for a long time, but starts to collapse at late times due to an instability arising from other geometrical variables.

Fig. 5.7 shows time evolutions of the maximum of $|\phi^2|$ and g_{xx} for Sommerfeld and blending OBCs using the maximal slicing condition. The code crashes eventually for the Sommerfeld OBC run when K develops a "W" shape instability around the center of the star, Fig. 5.9. The blending OBC run crashes when the extrinsic curvature components develop steep gradients around the blending region and the central interior region (see Fig. 5.8)—in particular, $\det(g_{ij})$ becomes negative!

The results of both runs reveal that the maximal slicing condition does *not* put K back to zero (as expected). Moreover, as observed previously in [64], *all* components of K_{ij} grow without bound, quickly causing the code to crash.

Following [64], I then tried a K-driver run with $c = 0.2$. A blending OBC (8 blending zones) was used. Fig. 5.10 shows a time evolution of the maximum of $|\rho| = |\phi|^2$ which slowly increases as long as the code runs. Fig. 5.11 shows a time evolution of the maximum of $|g_{xx}|$. A typical profile of K_{xx} is shown in Fig. 5.12.

Results for a Sommerfeld OBC run is shown in Fig. 5.13, 5.14, and 5.15.

The results for K-driver runs with $c = 0.2$ do not produce stable evolutions, but as c is increased, the results become much better, Fig. 5.16. For a K-driver run with $c = 1.0$, the boson star oscillates with a characteristic frequency, $\omega \sim 0.994146$ until $t \sim 140$ and then it slowly dissipates, Fig. 5.16 (c). g_{ij} oscillates approximately with a light crossing time, $t \sim 60$, Fig. 5.16 (d).

Very long time stable evolution is yet to be demonstrated, but study along this line will be continued.

Once I stabilize a single boson star, the next step is to move a single star with linear momentum and to spin a single star. This is a first step towards a simulation of binary boson star coalescences.
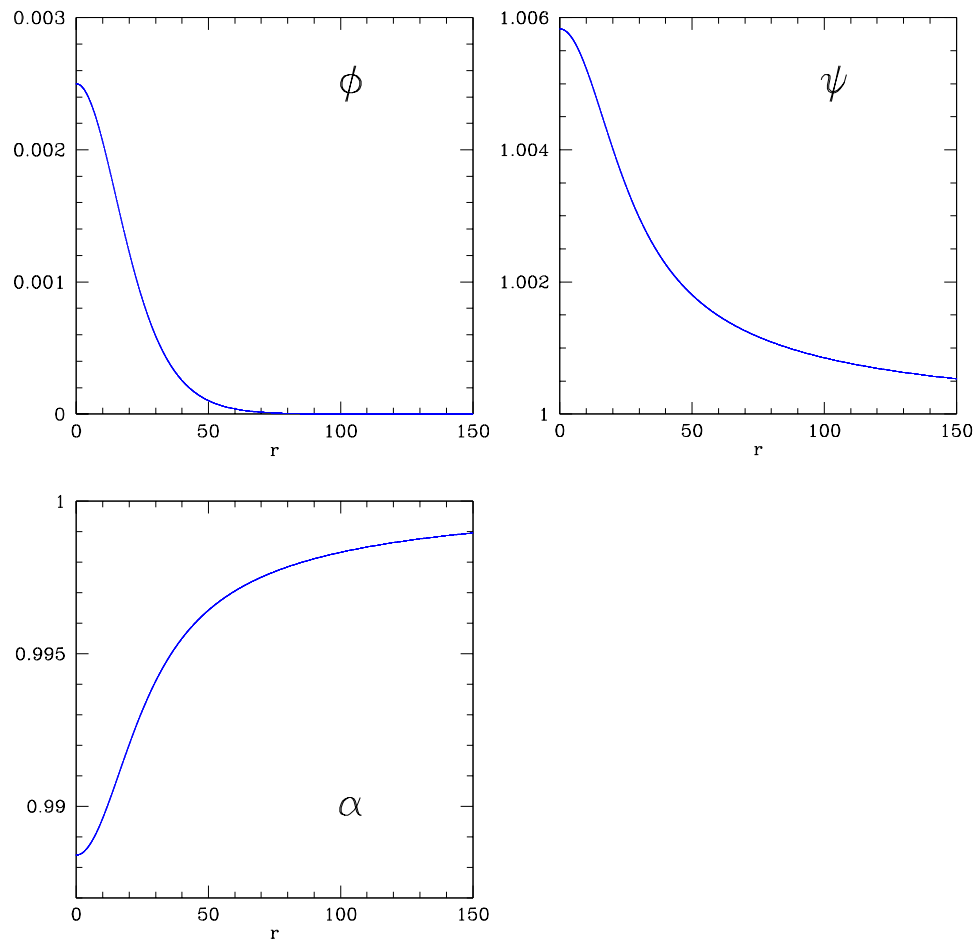
Figure 5.1: This figure shows $\phi(r)$, $\psi(r)$, and $V(r)$, as a function of r for a general relativistic stationary boson star. For this data set, $\phi(r = 0) = 0.0025$ and, $\omega = 0.994146$.
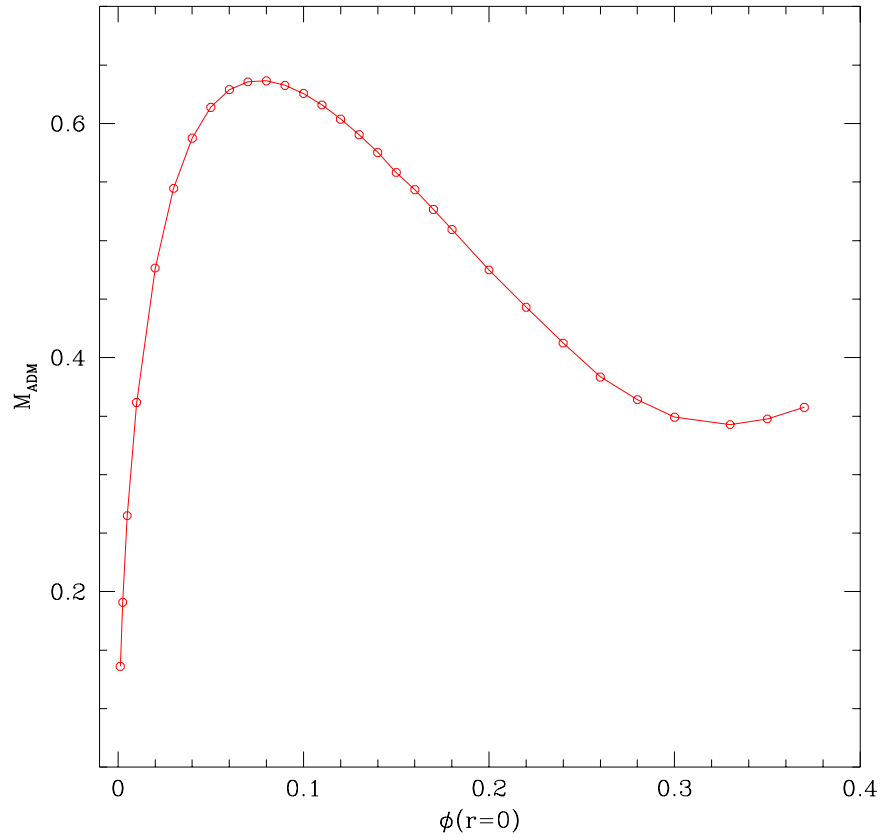
Figure 5.2: ADM mass (in units M_{PI}^2/m) of the ground-state boson stars as a function of ϕ_0, the square root of the central density. The maximum mass $M_c \sim 0.64$ occurs at $\phi_0 \sim 0.08$.
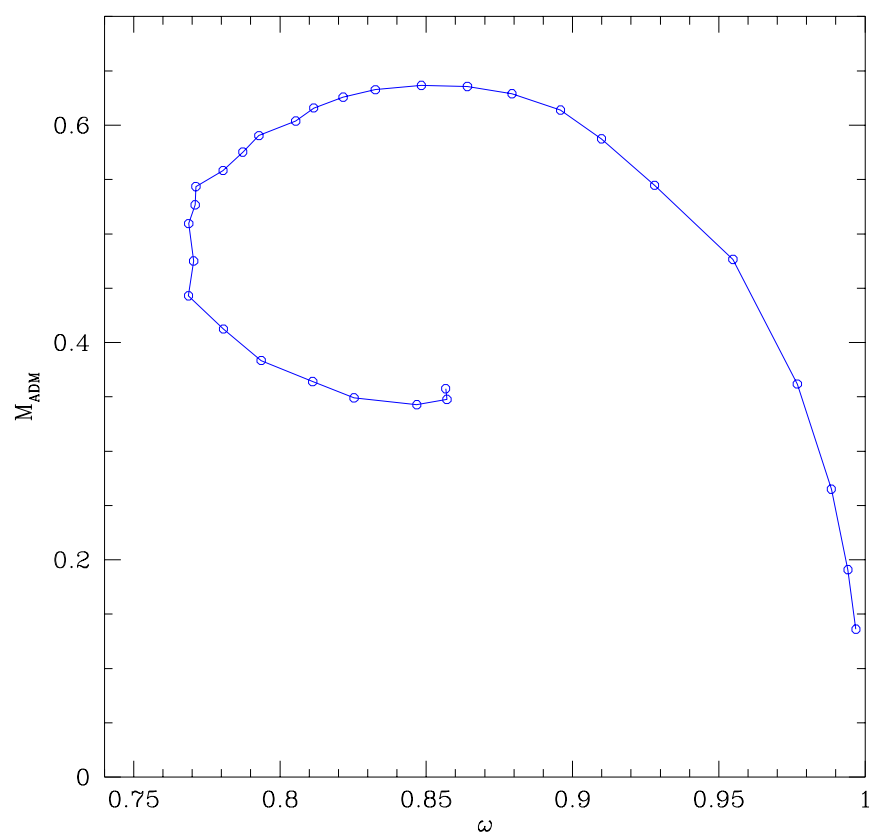
Figure 5.3: ADM mass, M_{ADM} vs. energy eigenvalue, ω for a single stationary star.
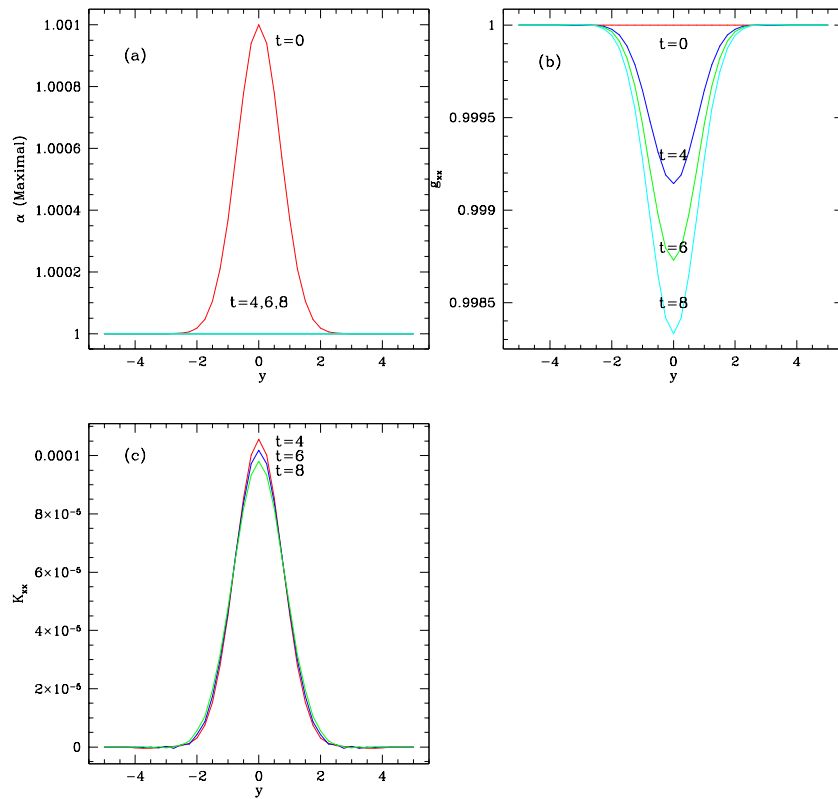
Figure 5.4: (a) The lapse at various times is shown. The initial lapse ($t = 0$) is put in by hand. Subsequent values are computed using the maximal MG solver. (b) g_{xx} at various times is shown. The maximal result shows a secular drift. (c) K_{xx} at various times is shown. The value of K_{xx} reaches a non-zero profile with maximal slicing and does not go back to zero. $\Delta x = \Delta y = \Delta z = 0.25$, $\Delta t = 0.05$ and the computational domain is $[-5, 5] \times [-5, 5] \times [-5, 5]$.
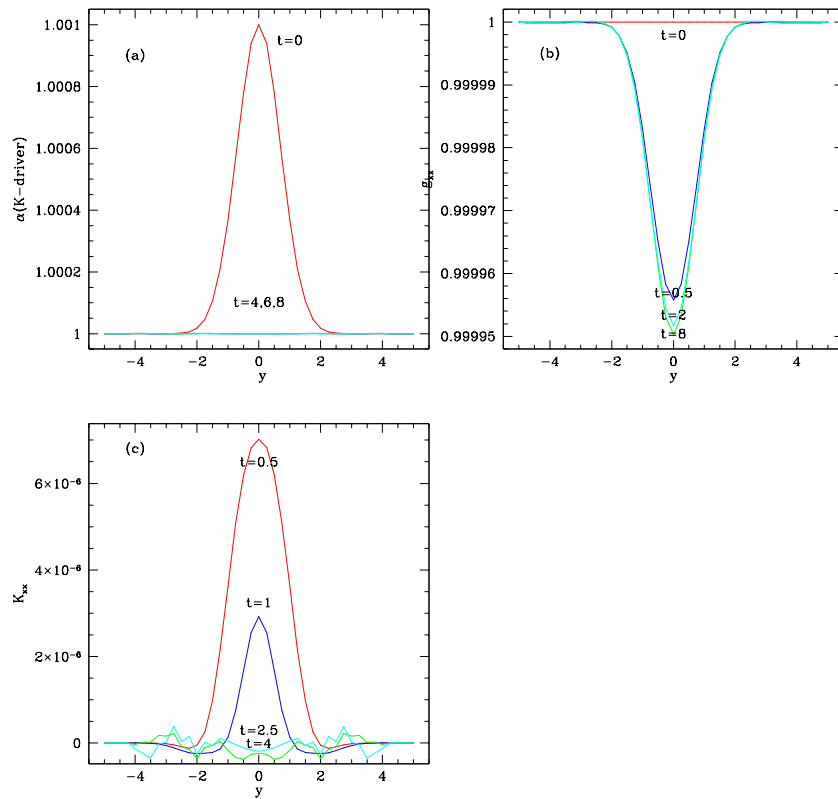
Figure 5.5: (a) The lapse at various times is shown. The initial lapse ($t = 0$) is specified arbitrarily. The lapse function is subsequently computed using the K-driver MG solver. (b) g_{xx} at various times is shown. The K-driver result shows a stable evolution. (c) K_{xx} at various times is shown. The K-driver condition actively enforces $K = 0$. $\Delta x = \Delta y = \Delta z = 0.25$, $\Delta t = 0.05$ and the computational domain is $[-5, 5] \times [-5, 5] \times [-5, 5]$.
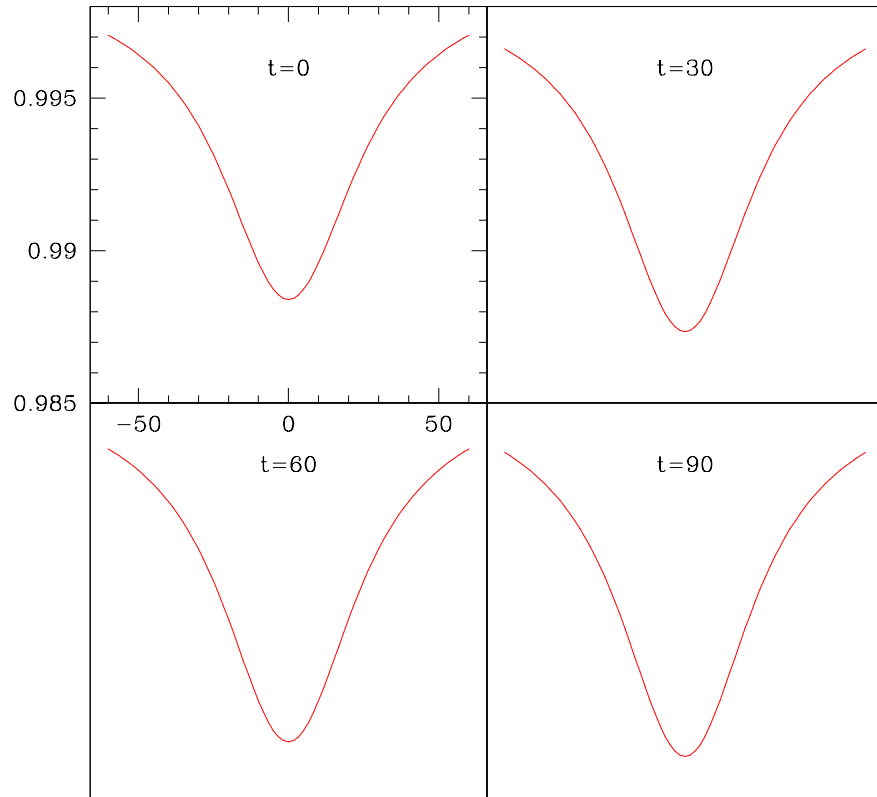
Figure 5.6: This figure shows profile of the lapse function, α, at various times along the y-axis for the maximal slicing condition. The lapse starts to collapse at later times due to instabilities in K_{ij}. $\Delta x = \Delta y = \Delta z = 1.667$, $\Delta t = 0.1667$ and the computational domain is $[-60, 60] \times [-60, 60] \times [-60, 60]$.
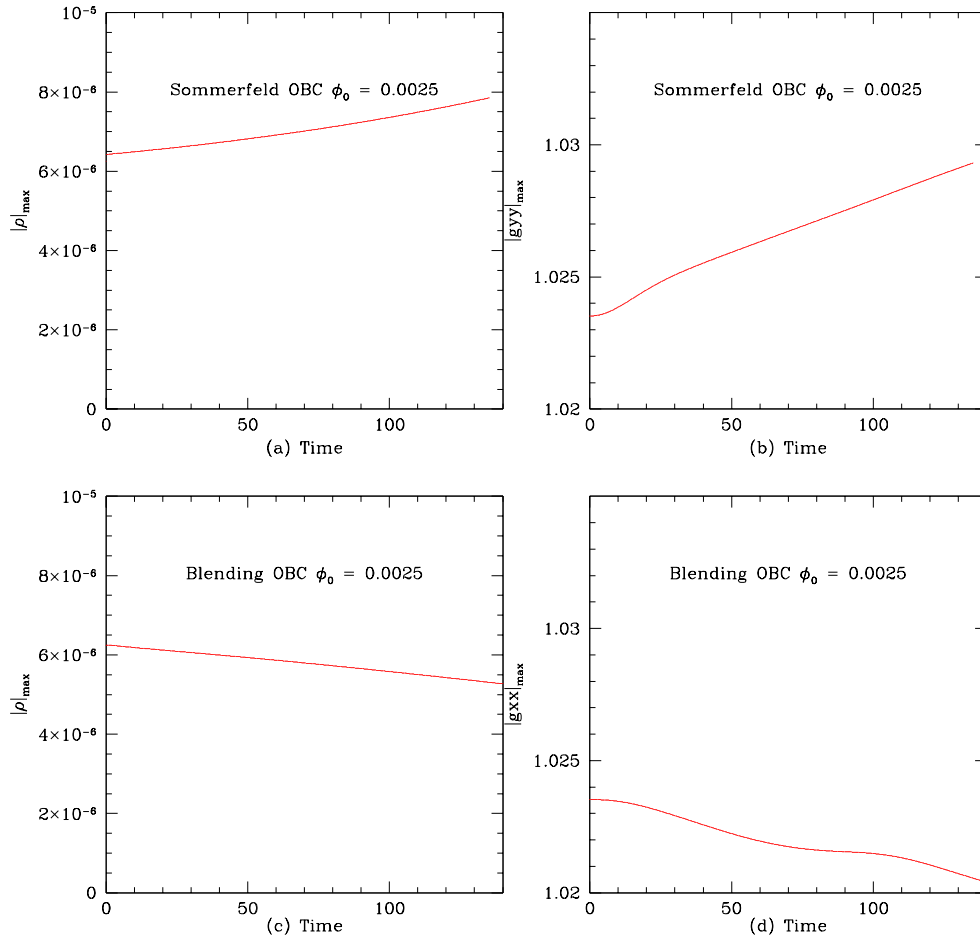
Figure 5.7: This figure shows the maxima of $|\phi^2| = |\rho|$ and g_{xx} as a function of time for a Sommerfeld OBC (a), (b) and an 8-zone blending OBC (c), (d). The maximal slicing condition, $K = 0$, is used. $\Delta x = \Delta y = \Delta z = 1.667$, $\Delta t = 0.1667$ and the computational domain is $[-60, 60] \times [-60, 60] \times [-60, 60]$.
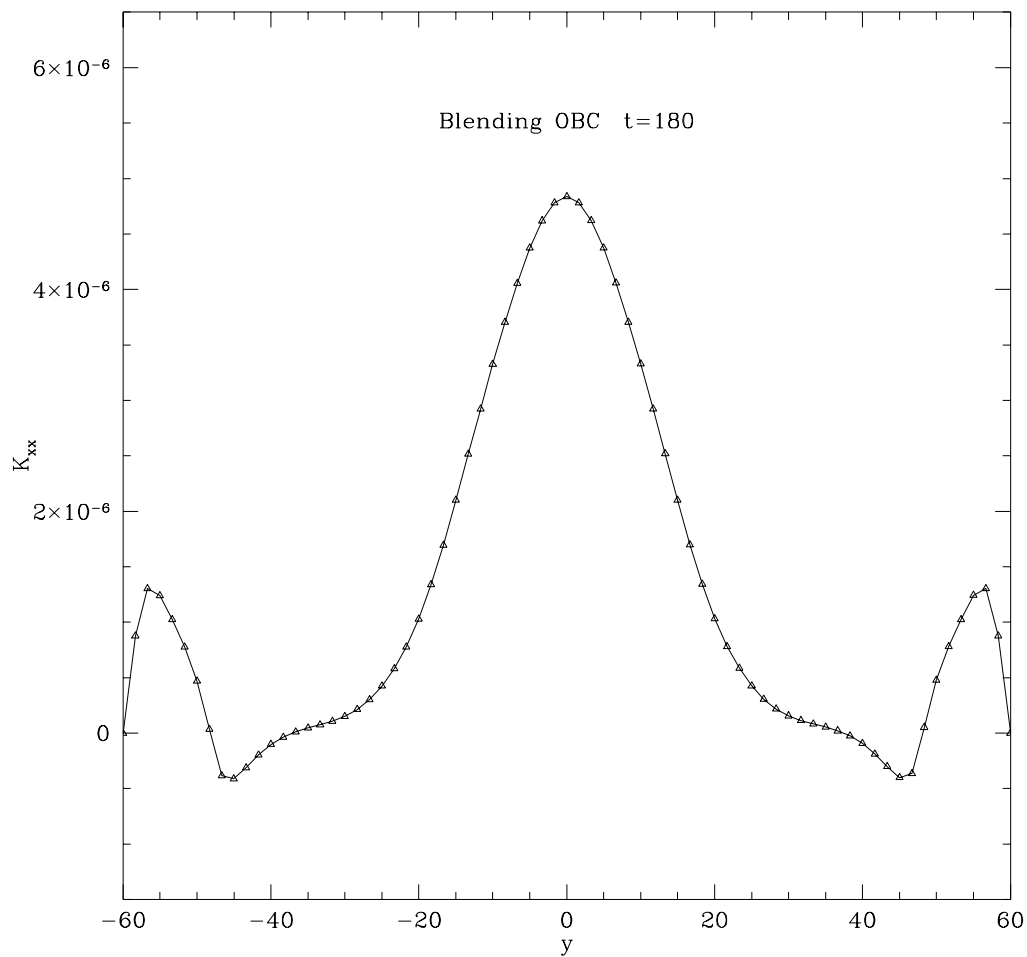
Figure 5.8: This figure shows K_{xx} along the y-axis at $t = 180$ for the blending OBC from the run described in Fig. 5.7.
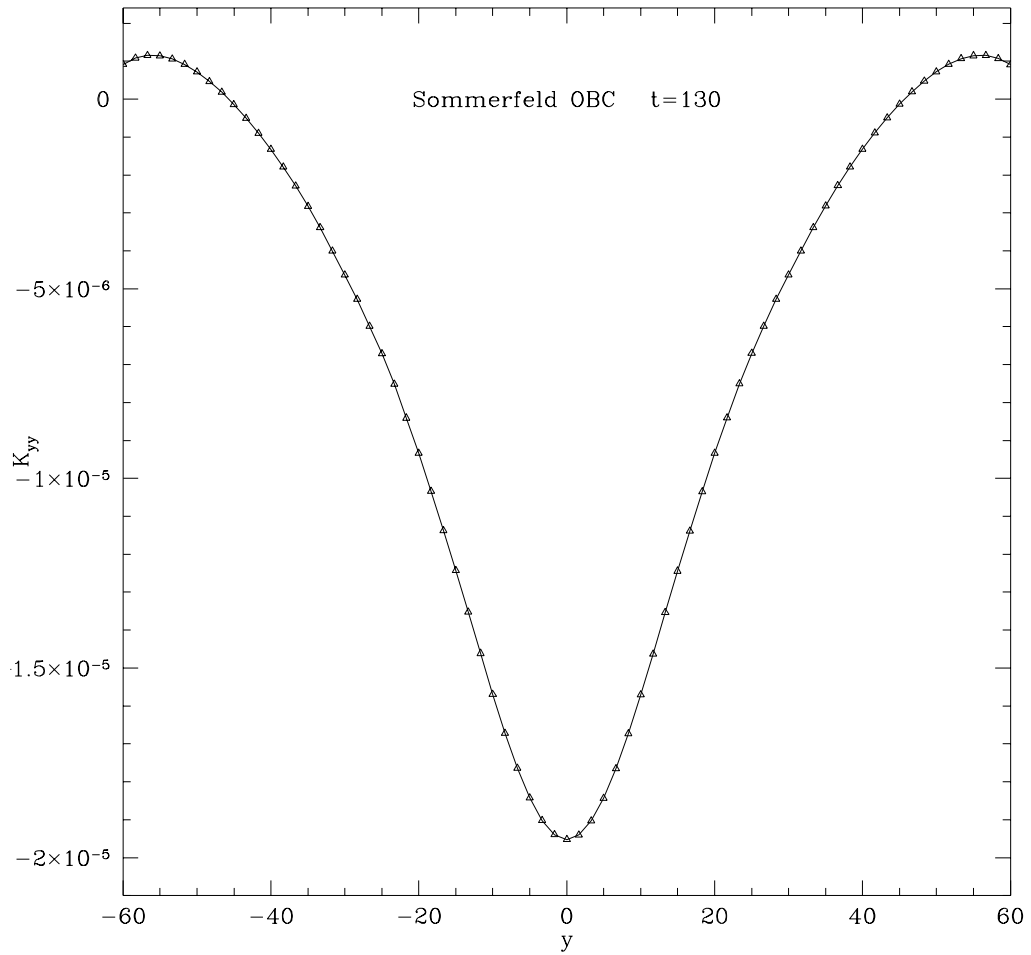
Figure 5.9: This figure shows K_{yy} along the y-axis at $t = 130$ for the Sommerfeld OBC from the run described in Fig. 5.7.
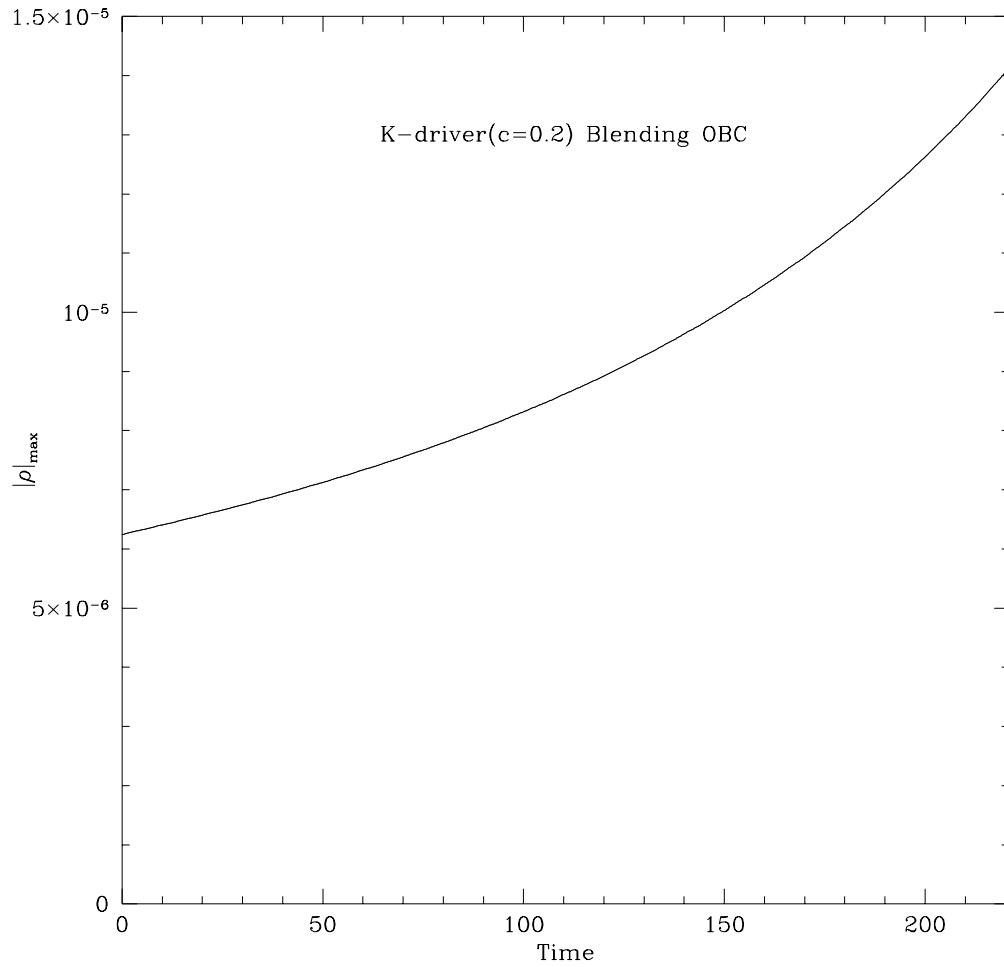
Figure 5.10: This figure shows the maximum of $|\rho| = |\phi|^2$ as a function of time using the K-driver coordinate condition with $c = 0.2$, and an 8-zone blending OBC. $\Delta x = \Delta y = \Delta z = 2.22$, $\Delta t = 0.222$, and the computational domain is $[-80, 80] \times [-80, 80] \times [-80, 80]$.
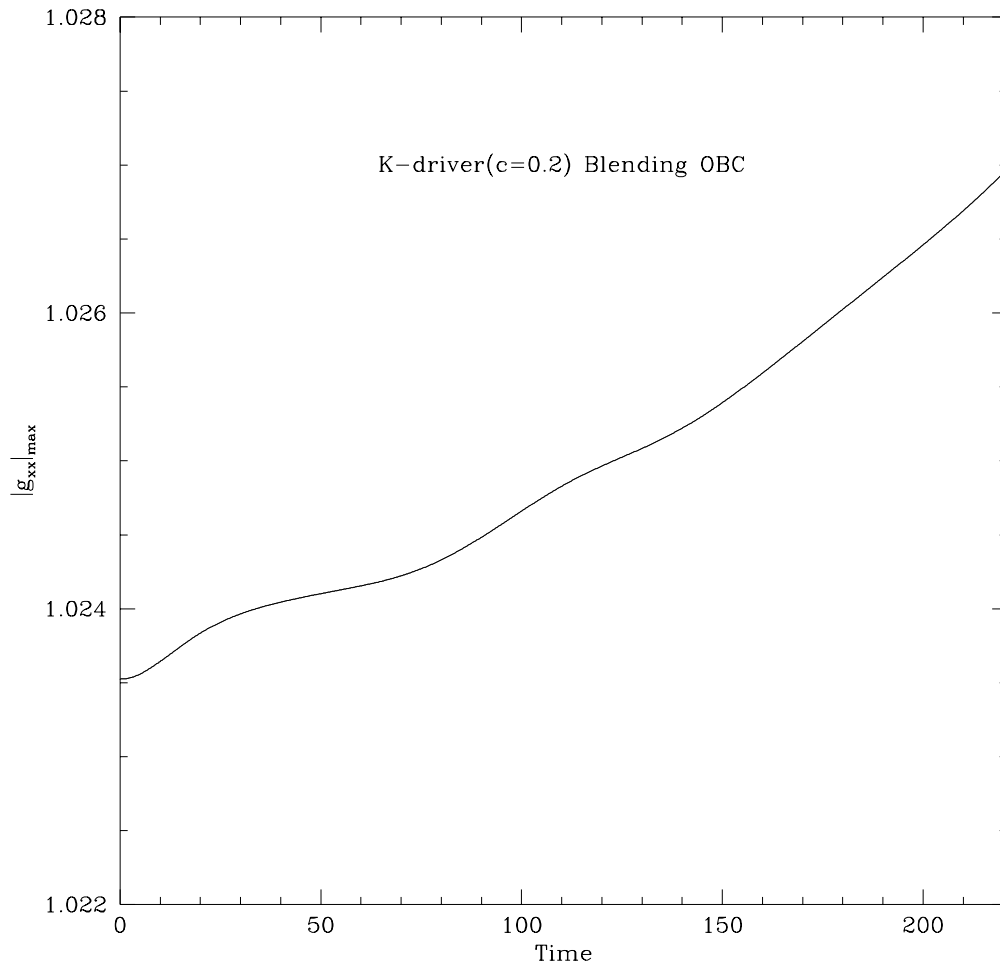
Figure 5.11: This figure shows the maximum of $|g_{xx}|$ as a function of time from the run described in Fig. 5.10.
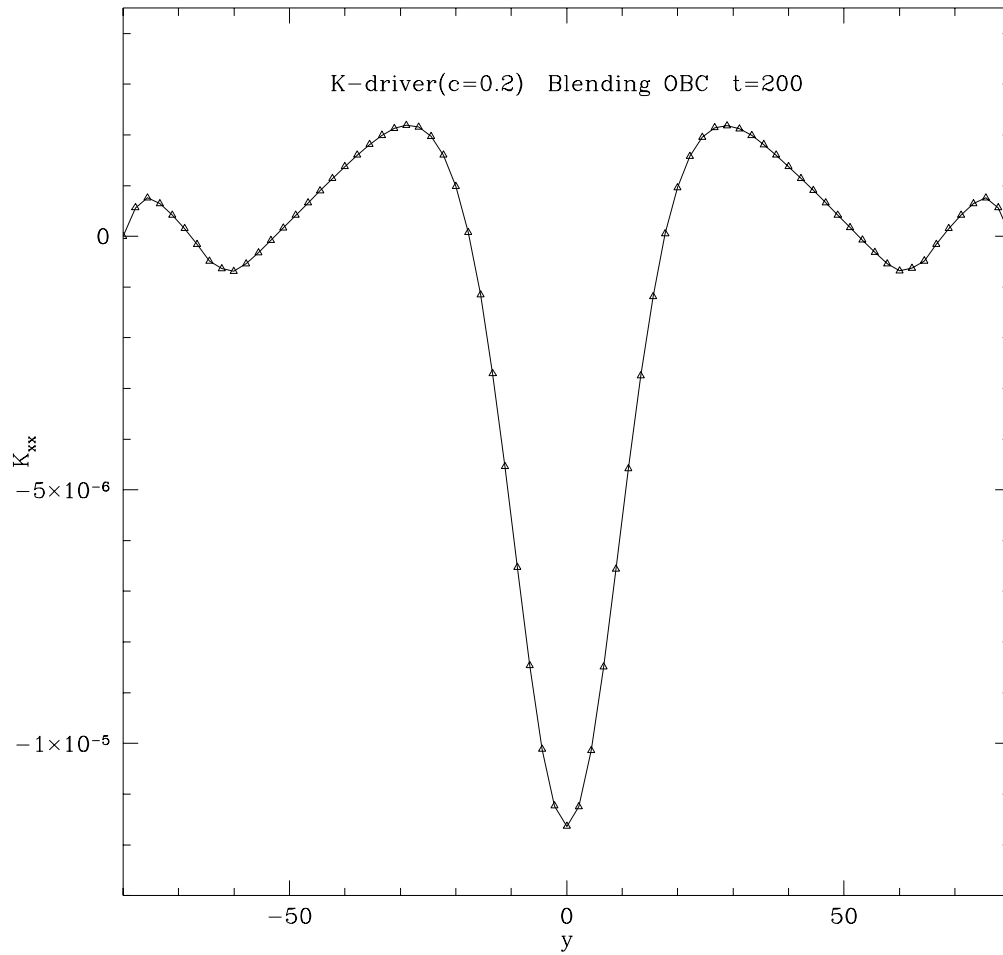
Figure 5.12: This figure shows K_{xx} along the y-axis at $t = 200$ from the run described in Fig. 5.10.
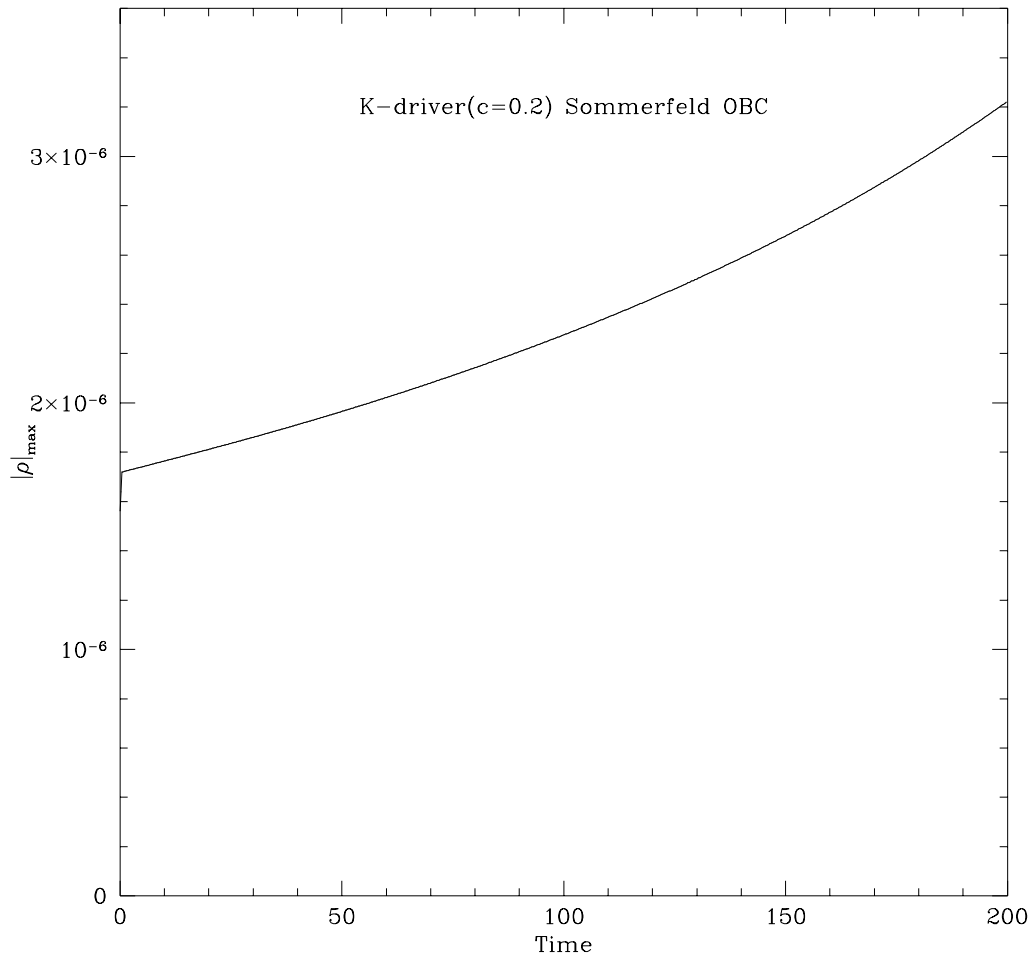
Figure 5.13: This figure shows the maximum of $|\rho| = |\phi|^2$ as a function of time using the K-driver coordinate condition with $c = 0.2$, and a Sommerfeld OBC. $\Delta x = \Delta y = \Delta z = 2.22$, $\Delta t = 0.222$, and the computational domain is $[-80, 80] \times [-80, 80] \times [-80, 80]$.
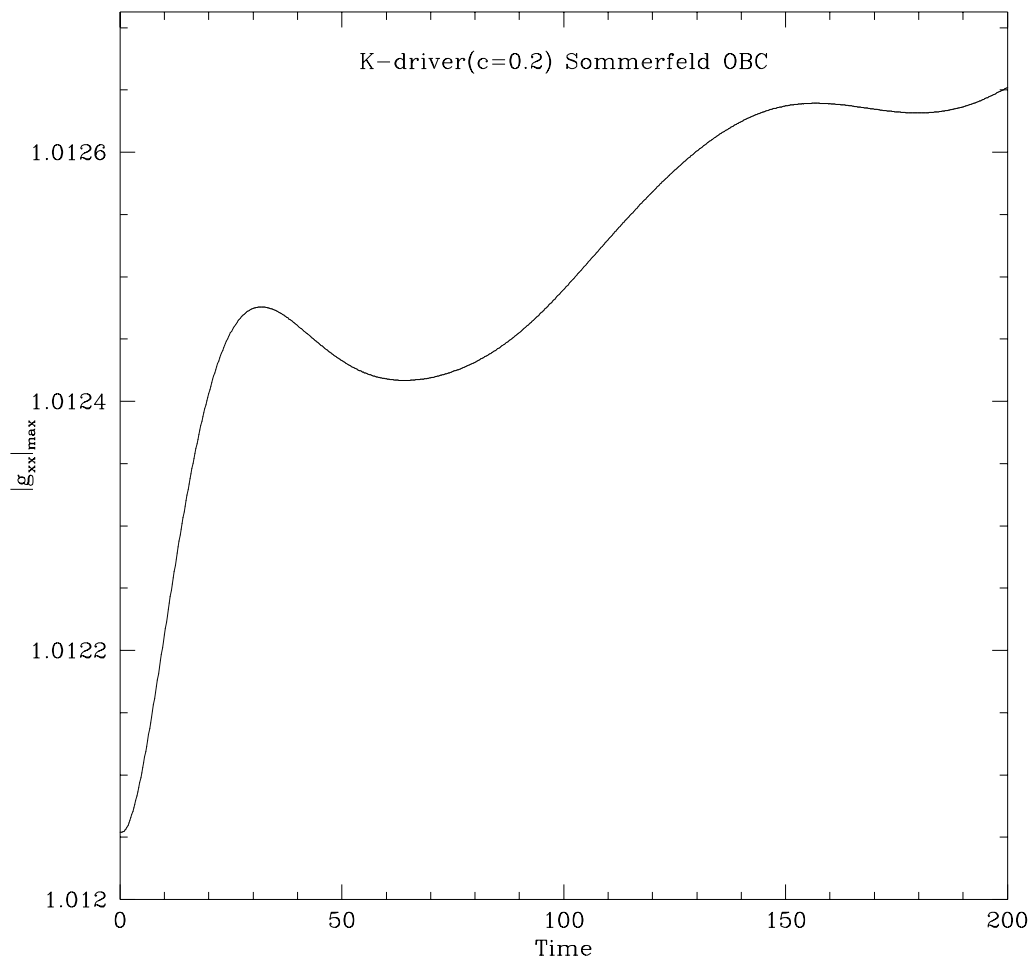
Figure 5.14: This figure shows the maximum of $|g_{xx}|$ as a function of time from the run described in Fig. 5.13.
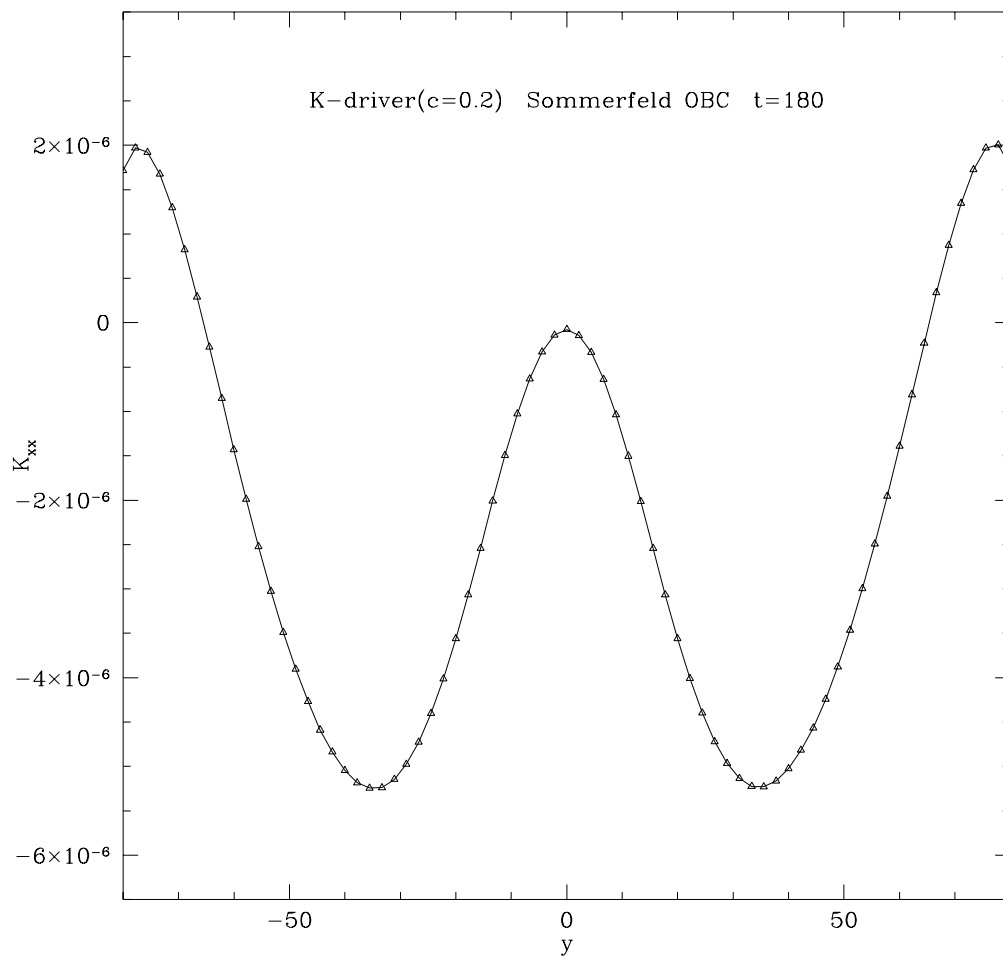
Figure 5.15: This figure shows K_{xx} along the y-axis at $t = 180$ from the run described in Fig. 5.13.
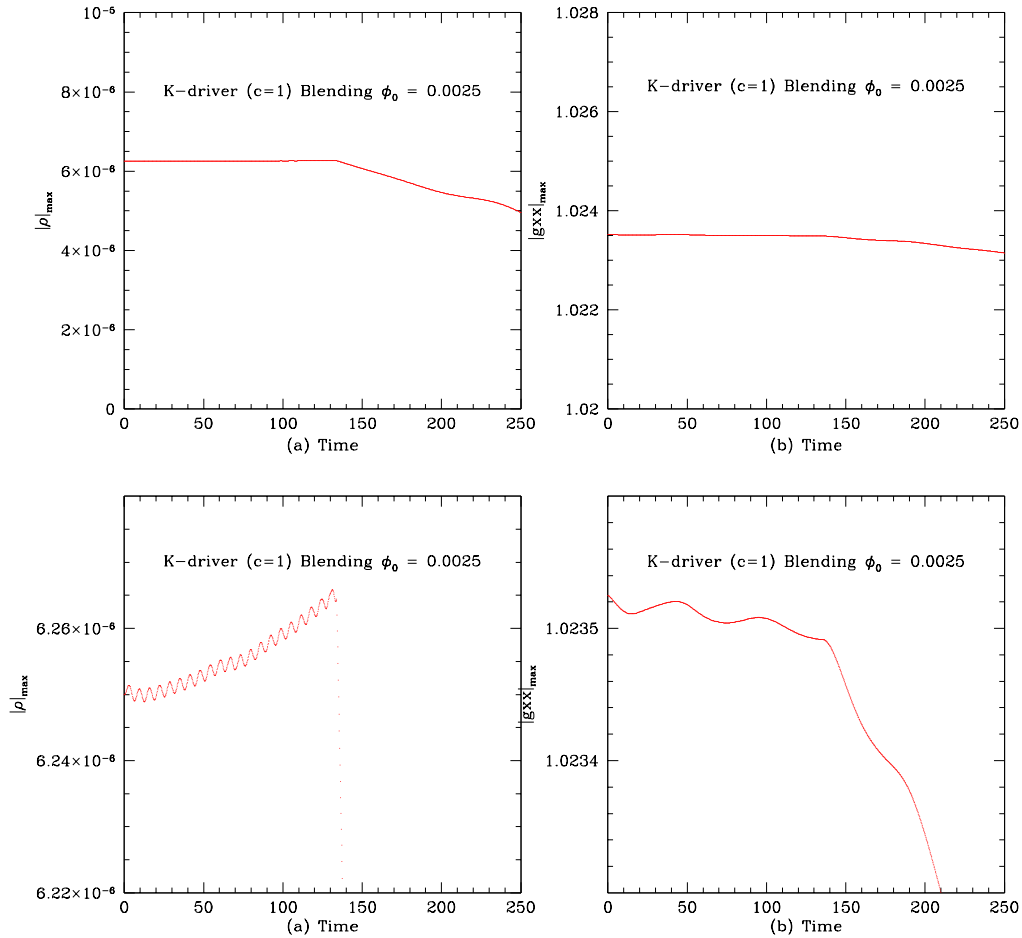
Figure 5.16: Maxima of $|\rho| = |\phi|^2$ (a) & (c) and $|g_{xx}|$ (b) & (d) as a function of time using the K-driver coordinate condition with $c = 1.0$, and an 8-zone blending OBC. $\Delta x = \Delta y = \Delta z = 1.67$, $\Delta t = 0.167$, and the computational domain is $[-60, 60] \times [-60, 60] \times [-60, 60]$ (c) shows a more detailed view in which the intrinsic oscillation of ϕ can be seen. In (d) the characteristic oscillation of the star (lower frequency than the intrinsic ϕ oscillation) is also apparent. At early times, this evolution appears considerably more stable than any of the other runs described above. However, the code still crashes rather quickly and the precise causes are still under investigation.

Chapter 6

Bose-Einstein Condensates in an Optical Lattice

In this chapter, I calculate the quantum motion of a Bose-Einstein condensate in an optical lattice generated by a standing wave of laser light. I show how to boost a stationary condensate into motion or stop a moving condensate by manipulating the optical lattice, and how to achieve Bloch oscillations of the condensate in an accelerating optical lattice. I show how atomic interactions affect these processes and discuss conditions for possible experimental realization. This chapter is based on a collaborative work with Qian Niu [68].

6.1 Introduction

Bose-Einstein Condensates (BEC) [69, 70, 71] in dilute atomic gases provide a good opportunity for controlled study and manipulation of their dynamics, which has not been possible for He superfluids. Much work has already been done along this line of research, including the studies of nonlinear response to time-dependent modulations of the trap potential [72], two-species BEC under external perturbations [73, 74, 75, 76], vortex states in trapped condensates [77, 78, 79, 80], and condensates in spatially periodic potentials [81].

In this Chapter, I investigate the possibility of manipulating the condensate by a periodic potential, which may be created by a standing wave of laser light [82]. In particular, I show how to boost a stationary condensate to a finite velocity and study how a moving condensate may be stopped by a stationary potential. I also show how Bloch oscillations of the condensate arise in an accelerating potential. The motion of ultra-cold but non-BEC atoms in accelerating potentials have been studied extensively, and can be understood in a model of non-interacting atoms [83, 84, 85]. Here I am interested in the effect of atomic interactions on the quantum transport of the condensate.

Instead of using trapped gases, I study a model of a free condensate released from a trapping potential after the ground state BEC is achieved. The typical size of a BEC wavepacket is of order 10 μm, which expands with a typical time scale of 10 ms. The wavelength of our standing wave will be much smaller than this size, and the proposed experimental processes are also of much shorter duration than the expansion time. It is

then reasonable to model the condensate dynamics as a one dimensional problem, where the system varies in the direction of the standing wave and is uniform in the perpendicular directions. Another case of interest is a BEC strongly confined in a long cigar shape [86, 87]. The density profile in the transverse directions is held fixed by the trap while the motion along the longitudinal direction can be considered free. When the standing wave of the laser light is applied along the longitudinal direction, it suffices to consider only that direction, with the caution that the effective scattering length between the particles is renormalized by a factor of half due to the transverse confinement [88]. In both cases I can model the motion as a one-dimensional problem and take the initial state to be uniform before the standing wave is turned on.

6.2   Quantum Transport in Optical Lattices

Quantum transport phenomena such as Bloch oscillations and Landau-Zener tunneling have been studied theoretically in condensed matter physics since the early 1930s, but have not been observed in a crystalline solid because scattering by impurities, phonons, and effects of other particles preventing the completion of even a single period of Bloch oscillation. Another problem is that the natural lattice spacing ($\leq$ 1nm) is very small requiring enormous electric fields to obtain the substantial tilt of the potential needed for small Bloch periods. The Bloch period is $\tau_B = h/(Fd)$, where h is Planck's constant, d is the lattice spacing, and F is the force on the particle.

The situation becomes much more favorable in clean superlattices. The lattice constant of these structures can be $\sim$ 10nm, yielding a much shorter Bloch period under the same electric field. In the late 1980s, Wannier-Stark ladders were seen in superlattices, evidence for Bloch oscillations was seen, and the observation of Zener breakdown was reported. There results represent an important breakthrough in the study of quantum transport of electrons. But dissipation and elastic scattering by impurities are still a central problem limiting the coherent evolution required of quantum transport.

However, with the recent development of laser techniques, new systems have emerged to study Bloch oscillations, Wannier-Stark ladders, and Landau-Zener tunneling. These systems use atoms instead of electrons and a periodic light field instead of the periodic crystalline potential. The advantages of this approach are precise initial state preparation, and final detection, negligible dissipation or defects and the possibility for time-resolved measurements of quantum transport.

The light field is created by a laser standing wave made of two counterpropagating, equal-intensity waves. When they have exactly the same frequency, the potential is stationary. The light intensity along the standing wave is of the form $I_0 \sin^2(kx)$, where $k = (2\pi/\lambda)$,

λ is the optical wavelength. For a sufficient large detuning between the laser and the atomic frequency, the atoms remain in the ground state and simply experience a potential $V(x)$ that is proportional to the intensity.

I adopt this new approach based on the optical lattice and carried out numerical simulations to study the quantum transport phenomena.

6.3 Nonlinear Schrödinger Equation

My study of the BEC dynamics will be based on the nonlinear Schrödinger equation. The equation has been successfully applied to the calculation of stable BEC states, the expansion of BEC, and collective excitations [89, 90, 91, 92, 93, 94, 95]. It can be derived from the mean-field theory, with the atom-atom interaction modeled by a repulsive δ-function potential, and should be very accurate for the dilute, near-zero temperature condensate [96, 97]. Specifically, I consider the following 1D equation,

$$i\hbar\frac{\partial\phi}{\partial t} = -\frac{\hbar^2}{2m}\frac{\partial^2\phi}{\partial x^2} + V_0\cos(2k_L x)\phi + \frac{4\pi\hbar^2 a}{m}|\phi|^2\phi \tag{6.1}$$

where m is the atomic mass, k_L is the wave vector of the laser light, a is the s-wave scattering length between atoms, and V_0 is the magnitude of the potential which is proportional to the light intensity. The normalization of the wave function is such that $|\phi|^2$ represents the number of atoms per unit volume.

I rescale Eqn. (6.1) by introducing dimensionless variables,

$$\tilde{x} = 2k_L x \tag{6.2}$$

$$\tilde{t} = \frac{\hbar}{m}4k_L^2 t \tag{6.3}$$

$$\tilde{\phi} = \frac{\phi}{\sqrt{n_0}} \tag{6.4}$$

$$\tilde{V}_0 = \frac{m}{\hbar^2}(\frac{1}{4k_L^2})V_0 \tag{6.5}$$

$$C = \frac{\pi n_0 a}{k_L^2} \tag{6.6}$$

where n_0 is the density of BEC. Then I obtain the dimensionless equation (replacing $\tilde{x}$ by x, etc.),

$$i\frac{\partial\phi}{\partial t} = -\frac{1}{2}\frac{\partial^2\phi}{\partial x^2} + V_0\cos(x)\phi + C|\phi|^2\phi \tag{6.7}$$

I set $V_0 = 0.1 \sim 0.4$ and calculate the response of the solutions to the external potential for various values of C. As in Ref.[89], I use the Crank-Nicholson method [32, 3] for the numerical solution of Eqn. (6.7). This method preserves the unitarity of the time-evolution, and yields good convergence of the solutions for moderate values of the non-linear coupling strength C ($C \leq 1$ mostly in this work).

6.4   Blocking Condensates

First, I consider how the current of a moving condensate degrades when a stationary periodic potential is turned on. My initial wave function is taken to be $\phi = e^{ik_0 x}$ which has a current k_0. (In the Chapter 6.5, I will show how such a state may be prepared.) The potential is then turned on adiabatically to a strength V_0 in a time t_0 and stays constant afterwards. From the solution, I obtain the condensate current

$$j = (\frac{\hbar}{m})\text{Im}(\phi^* \frac{d\phi}{dx}) \tag{6.8}$$

as shown in Fig. 6.1, where I have taken $k_0 = 1/4$, $V_0 = 0.05$, and $t_0 = 60$.
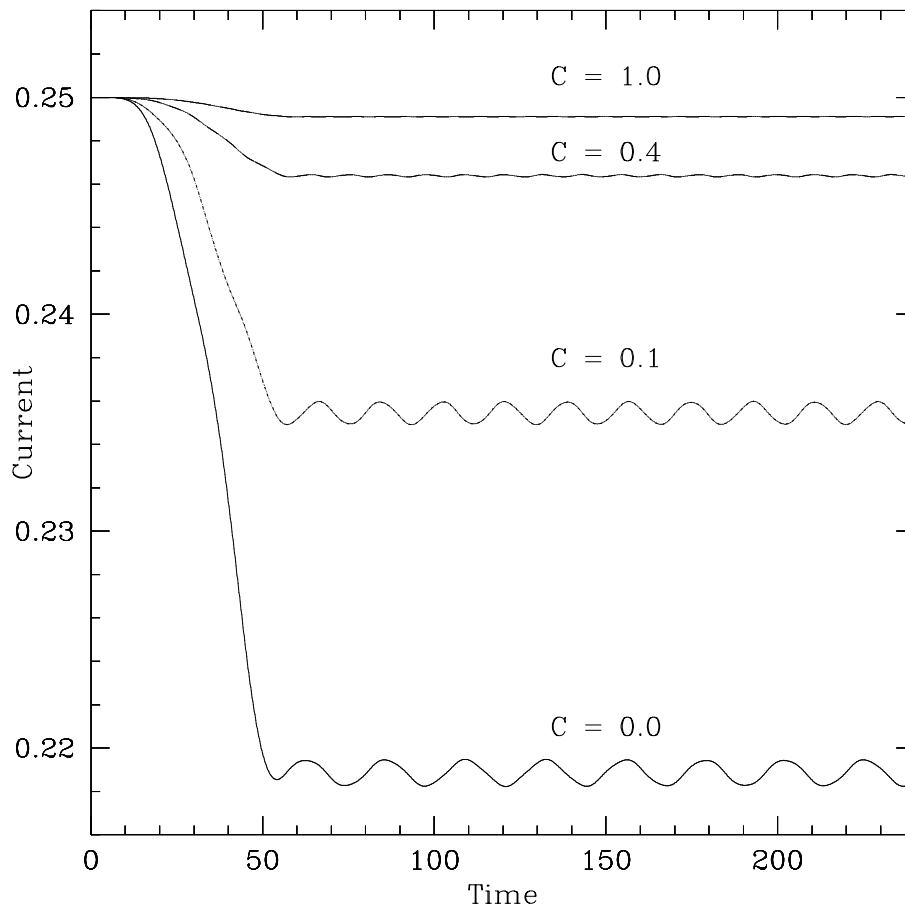
Figure 6.1: Current as a function of time for the wavefunction with initial current $k_0 = 1/4$. $V_0 = 0.1$, and $t_0 = 60$. Results are shown for $C = 0.0$, 0.1, 0.4, and 1.0.

The current decreases as the potential is turned on and settles down to new values

depending on the strength of the atomic interaction C. For small C, the current decreases dramatically, but for $C \geq 1.0$, the current stays almost constant (also see Fig. 6.2(a)). These results show that the ability for the condensate to maintain its current depends crucially on the strength of interaction between the atoms.

This strong dependence is explained by the screening effect. I view our system as an ideal (non-interacting) gas in the effective potential

$$V_0 \cos(x) + C|\phi|^2 \tag{6.9}$$

with the condensate wave function corresponding to the Bloch state in the lowest energy band of the effective potential and with initial wave number k_0. The Bloch wave number is conserved because the potential is periodic and the state lies in the lowest band because k_0 lies in the first Brilloin zone and the potential is turned on adiabatically. The Bloch state has a periodic density profile so that the periodicity of the external potential is preserved in the effective potential. The screening effect arises because the density of atoms tends to be larger in the potential wells and smaller in the barrier regions, so that the second term in the effective potential tends to even out the first term which represents the external potential.

An explicit analytic expression for the effective potential can be calculated using perturbation theory as

$$V_{eff} \cos(x) + \text{const.} \tag{6.10}$$

where

$$V_{eff} = \frac{V_0}{1 + 4C} \tag{6.11}$$

This result is valid as long as the condensate density is nearly uniform, i.e., when $V_{eff} << 1$, which is realized for either a weak external potential or a strong atomic interaction. From this effective potential, I can also calculate the current perturbatively, with the result,

$$j = k_0 - \frac{8k_0 V_{eff}^2}{(4k_0^2 - 1)^2} \tag{6.12}$$

I plot the current and the effective potential as functions of C in Fig. 6.2, where I see that the analytical results agree very well with the numerical data.

The above picture of non-interacting condensate in a screened effective potential also gives an idea of the time scale for adiabaticity. The relevant energy gap is that between the lowest two bands at the same Bloch wave number, which is about $\Delta E = 1/4$ for $k_0 = 1/4$ in the limit of small V_{eff}. In order to avoid excitations across the gap, I choose our turn-on time of the potential to satisfy the condition,

$$\Delta t_0 > \frac{2\pi}{\Delta E} = 8\pi \tag{6.13}$$

Tiny oscillations of the current in Fig. 6.1 are due to residual non-adiabatic excitations, as is evident from the fact that their oscillation frequency coincides with ΔE. These oscillations becomes even smaller if I use a longer turn-on time.

6.5   Boosting Condensates

In this Section, I show how a stationary condensate can be boosted to a finite velocity. I first turn on a stationary potential adiabatically to a strength of 0.1, then accelerate the potential to a final velocity of v_f. The induced current (the average velocity) of the condensate is shown in Fig. 6.3 for $v_f = 0.2$ and for various values of atomic interaction C.

For $C = 0$, the condensate follows the motion of the potential, acquiring the same velocity as the potential. For nonzero C, the current is lower, implying a leakage of the atoms through the potential. For larger C, very little current is dragged by the potential. These results can again be simply understood in terms of the screen effect of atomic interactions. The insensitivity of the motion of the condensate with strong atomic interaction to an external potential reminds us of the property of a superfluid.

6.6   Bloch Oscillations

In this Section, I show in Fig. 6.4 Bloch oscillations of the condensate when the potential is accelerated at a constant rate a.

The average slope of the current is given by the acceleration, meaning that the condensate follows the potential on average. The oscillatory modulations can be understood by the following arguments. In the co-moving frame, the potential is stationary but the atoms feel an inertial force, which makes the Bloch wave number drifting at a rate of $-a$. If the lowest band of the effective potential has the dispersion $\epsilon(k)$, then the velocity in the co-moving frame is given by $\epsilon'(-at)$. Because of the periodicity of the Bloch band, this velocity has a zero mean and an oscillation period of $1/a$, which agree with the results in the figure.

The size and shape of the modulations (excluding the fast oscillations to be discussed below) in Fig. 6.4 can also be explained in terms of Bloch oscillations in the effective potential [84]. For $C = 0$, the potential of strength $V_0 = 0.4$ is known to produce a narrow band with a cosine energy dispersion, which explains the small and sinusoidal modulations in that case. For large C, the effective potential is weak, and the energy dispersion is parabolic (as $k^2/2$ in the free case) except near the Brilloin zone edge $k = \pm\frac{1}{2}$, where it becomes flat due to Bragg reflection. The acceleration of the condensate in the comoving frame is given by $-a\epsilon''(-at)$, which nearly cancels the acceleration of the potential everywhere, except when k is near the

zone edge. The velocity of the condensate should then follow a stair case curve, with the steps coincide with the occurrence of Bragg reflections. The fast oscillations for the cases of $C = 0.3$ and 0.5 in Fig. 6.4 are due to Landau-Zener tunneling [98] through the gap between the lowest two bands of the effective potential. The critical acceleration for the tunneling is $\pi V_{eff}^2/2$,[83] which is smaller for larger values of C and becomes comparable to the acceleration used in the calculation for the above two cases. A detailed study of Zener tunneling of a BEC will be reported in the future.

6.7 Landau Zener Tunnelings

In this section, I show in Fig. 6.5 that the transition from Bloch oscillations to Landau-Zener Tunnelings for a given acceleration, $a = 0.02$. For $C = 0$ and 0.1, Bloch oscillations are apparent for the $k = 0$ state. As C is increased to 1, the signature for Landau-Zener tunneling appears. The $k = 8$ states, which are at the edge of the first Brilloin zone, shows different oscillation frequencies dominate by interband transitions.

This transition from Bloch oscillations to Landau-Zener tunneling can be also understood by the concept of screening via nonlinear atom-atom interaction.

The LZ tunneling rate across a gap under acceleration a of the potential can be estimated as

$$\gamma = ae^{\frac{a_c}{a}} \tag{6.14}$$

where $a_c = (\pi\Delta^2/K)$ is the critical acceleration, with Δ the half width of the gap and $K = (n/2)$ the wave number of Bragg scattering corresponding to the nth gap. For $V_0 = 0.4$, $a_c = 0.25$. For non-zero C's, the effective potential V_{eff} decreases as $V_{eff} \simeq V/(1 + 4C)$, so does the critical acceleration, $a_c \simeq \frac{\pi}{2}V_{eff}^2$. Applying the screening concept, $a_c \simeq 0.010$ for $C = 1$, so $a = 0.02$ is well over the critical acceleration. Comparing with a non-interacting case, $C = 0.0$, a clear signature of the Landau-Zener tunneling is seen in Fig. 6.6. Here atoms are not dragged by an ever-accelerating optical potential, the current just saturates at around 0.625.

6.8 Experimental Realization and Future Directions

In typical experiments to date, the relevant parameters are given by

$$n_0 = 10^{20}\text{m}^{-3}$$

$$a = 5.4\text{nm}$$

$$k_L = \frac{2\pi}{\lambda} = 8.06 \times 10^6\text{m}^{-1}$$

for Rb [99] and

$$n_0 = 3 \times 10^{21} \text{m}^{-3}$$

$$a = 2.65 \text{nm}$$

$$k_L = 1.07 \times 10^7 \text{m}^{-1}$$

for Na [87]. The strength of atom-atom interaction is given by $C = (\pi n_0 a / k_L^2) = 2.6 \times 10^{-2}$ for Rb and $C = 2.2 \times 10^{-1}$ for Na. Larger values of C may be achieved by a higher density of the condensate, a higher a, and a smaller k_L. All three parameters can be changed independently. A higher density may be achieved by a factor 5 enhancement without rendering the condensate's life time too short for the processes discussed here. a can be tuned as well by a Feshbach resonance [87, 100, 101]. A smaller k_L may be achieved by adjusting the relative angle between the two beams of interfering light without changing the laser frequency. Therefore, the phenomena discussed in this Letter should be observable within the current experimental capability.

Apart from a detailed study of the Landau-Zener tunneling mentioned above, future theoretical investigations are needed to explore other possibilities of the condensate motion such as Wannier-Stark ladders and quantum chaos, which have been observed on cold but non-BEC atoms. Because of the non-linearity due to atomic interactions, spontaneous breaking of translational symmetry of the condensate can occur under certain conditions as is seen in a primitive study of ours. Further improvement of the theoretical framework is also needed to include the effects of thermal and quantum fluctuations.

Note added: During the revision of this thesis, I received a preprint from Anderson and Kasevich, reporting the observation of Bloch oscillations and Zener tunneling of a BEC in a stationary optical lattice under gravity. [102] In the free-falling frame of reference, this experimental system is equivalent to the one described here, and offers a potentially good testing ground for our theoretical predictions.
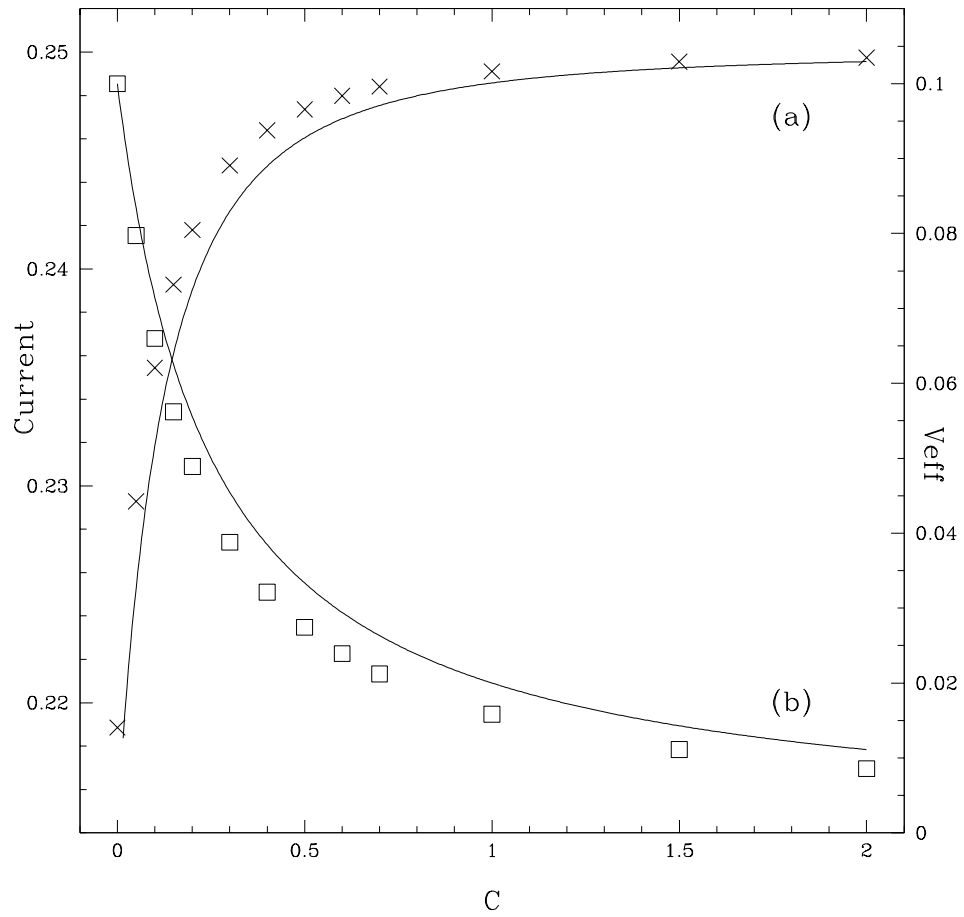
Figure 6.2: Average current (a) and the strength of the effective potential V_{eff} (b) as a function of C after the turn-on of the potential for the runs in Fig. 6.1. Open squares and crosses are numerical results. Solid lines are analytic results.
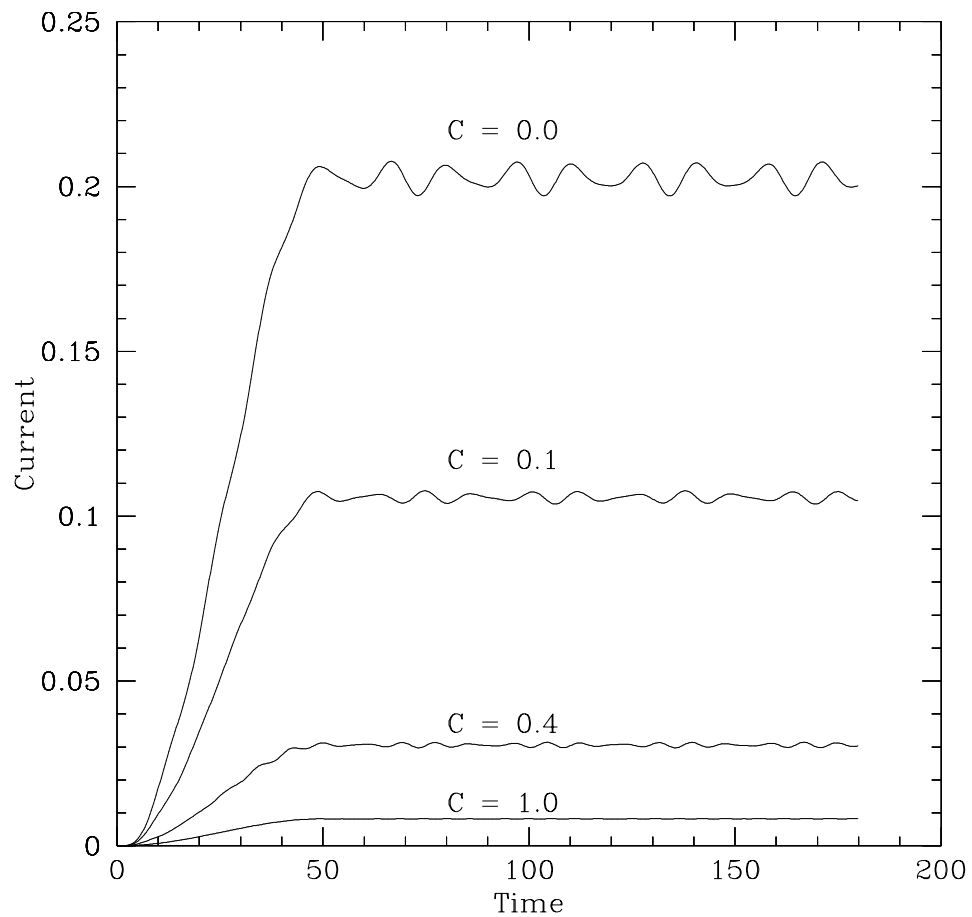
Figure 6.3: Current as a function of time for the wavefunction with zero initial current. V_0 = 0.1 and the acceleration occurs between $t = 0$ and $t = 50$. Results are shown for $C = 0.0$, 0.1, 0.4, and 1.0.
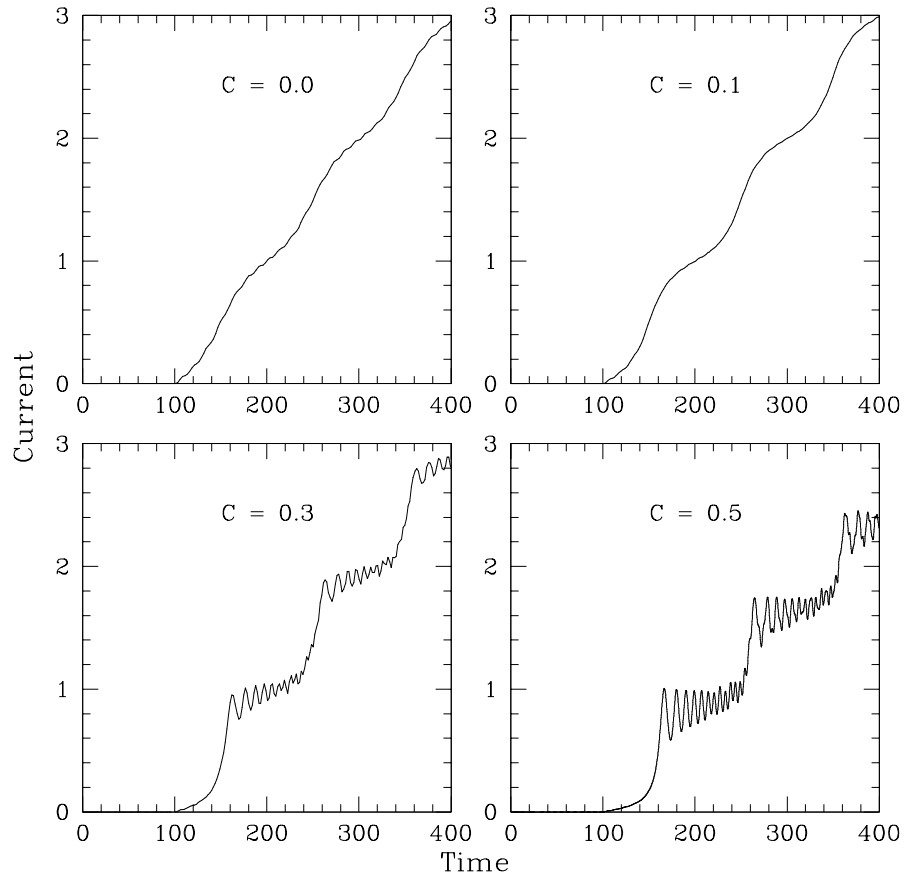
Figure 6.4: Current as a function of time for the wavefunction with zero initial current. Parameters are $V_0 = 0.4$ and $t_0 = 70$. The acceleration is $a = 0.01$ for $t \geq 100$. Results are shown for $C = 0.0$, 0.1, 0.3, and 0.5.
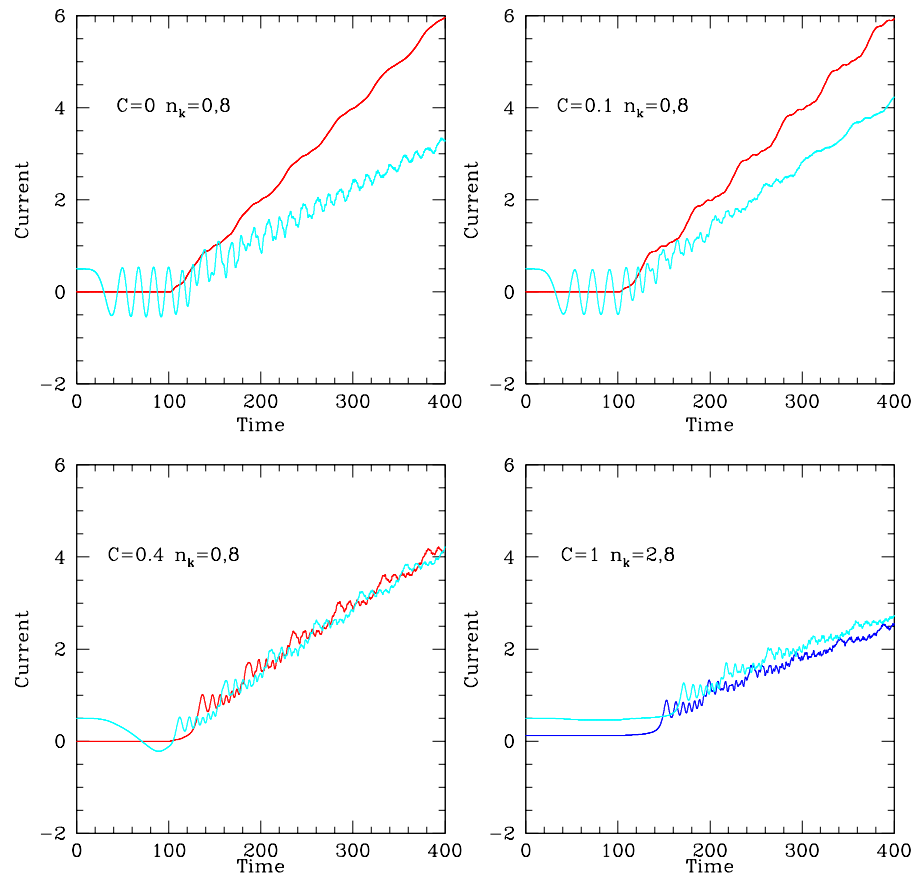
Figure 6.5: Current as a function of time for the wavefunction with initial data $\phi = e^{ikx}$, $k = 0$ through $n_k(\equiv \frac{N}{2})$ where N is a number of period in the calculation. For this set of data, I used $N = 16$, i.e., $n_k = 8$ corresponds to the first Brilloin zone edge. Parameters are $V_0 = 0.4$ and $t_0 = 70$. The acceleration is $a = 0.02$ for $t \geq 100$. Results are shown for $C = 0.0$, 0.1, 0.4, and 1.0.
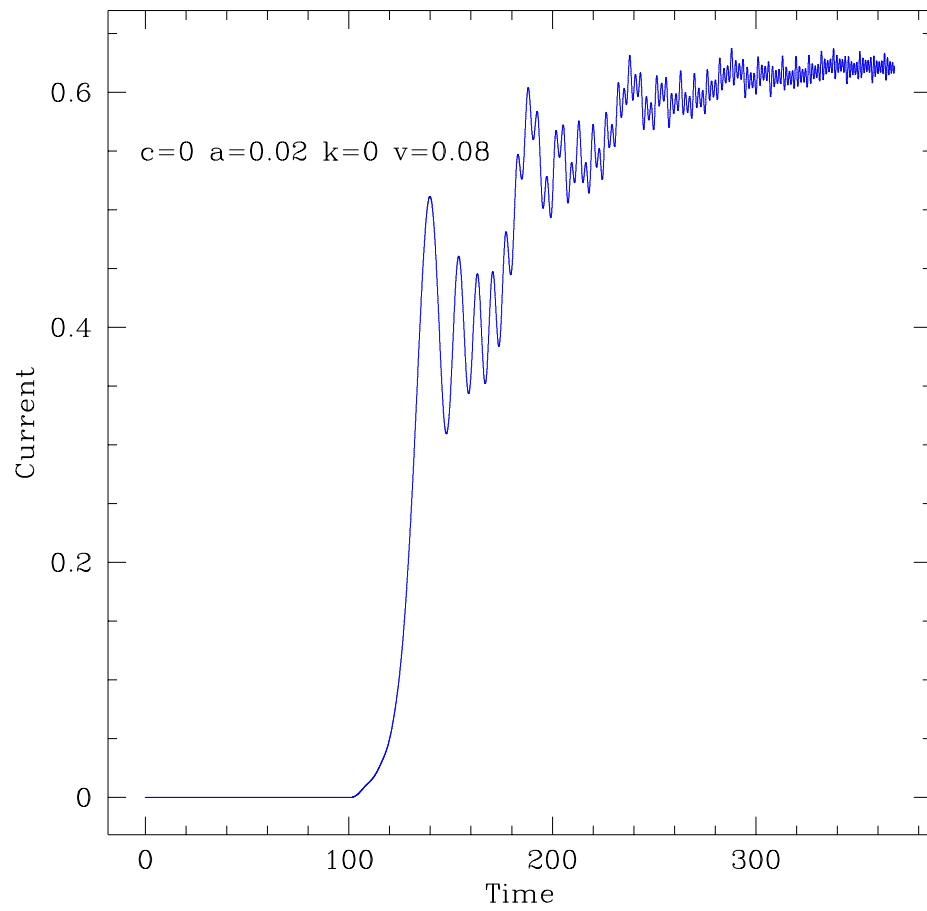
Figure 6.6: Current as a function of time for an initial wavefunction $\phi = e^{ikx}$, with $k = 0$. Parameters are $V_0 = 0.08$, $C = 0.0$ and $t_0 = 70$. The acceleration is $a = 0.02$ for $t \geq 100$.

Chapter 7

Stabilization in a 2D Atomic Model

In this Chapter, I present calculations of stabilization lifetimes for 2D "soft-core" hydrogen driven by a high intensity high frequency laser. I study this effect for both linear and circular laser polarization. In either case, the wavefunction obtains a characteristic form. For linear polarization, the radiative signature of stabilization is shown. I also discuss the dynamical nature of the stabilization. This chapter is based on a collaborative work with Will Chism and Linda Reichl [103].

7.1 Introduction

The advent of lasers capable of producing electric fields on the order of interatomic electric fields has led to the discovery of many unexpected nonperturbative phenomena[104]. One of the more recent effects to gain attention is the *adiabatic stabilization* of atoms in intense, high-frequency laser fields. Stabilization is characterized by a *decrease* of ionization probability in an atom-laser system, as the intensity of the laser is *increased*. This phenomena, originally predicted by Gersten and Mittleman[105], is inherent to the dressed, or Floquet, states of the atom-laser system. These states are time periodic, and hence, are defined only in the limit of adiabatic turn-on. The high-frequency condition is given roughly by $\hbar\omega \geq I_p$, where ω is the laser frequency and I_p is the ionization potential.

Using high frequency Floquet theory (HFFT), Pont, Gavrila, and co-workers[106] presented the first computations indicating stabilization in laser driven hydrogen. For linear polarization, they found that the wavefunction obtains a *dichotomous* form. Pont and Gavrila also calculated lifetimes for atomic hydrogen driven by a high-frequency laser of circular polarization[107], although no waveform analysis was presented. Subsequently, using a finite difference technique, Kulander, Schafer, and Krause calculated the stabilized state lifetimes for ground state (g.s.) hydrogen driven by linearly polarized laser fields[108]. As with the Floquet calculations, this computation employs the non-relativistic Schrödinger equation, treats the interaction in the dipole approximation, and assumes a classical laser field[109]. The field is ramped up to a constant value, after which the probability in the vicinity of the

nucleus obeys a reasonably well defined exponential decay. The lifetime is identified with the inverse of the decay rate. Comparison with lifetimes obtained via HFFT show agreement to within an order of magnitude[110].

Insight into the mechanism for stabilization has been gained by considering the one dimensional classical motion corresponding to linear laser polarization[111]. In the Kramers-Henneberger frame, the electron drifts back and forth between the turning points, being passed multiple times by the atomic core. However, the electron can only be ionized by the longer duration impulses it may receive while it is near the turning points. The turning points occur at $\pm \alpha_o$, where $\alpha_o \equiv F/\omega^2$, and F and ω are the laser field and frequency in atomic units ($\hbar = e = m = 1$). As the field is increased, the excursion is increased, and the electron spends more time away from the turning points. Thus, the lifetime is increased.

These predictions of stabilization were based upon the use of g.s. hydrogen as the initial state, which requires a laser photon energy above $13.7eV$, well beyond present laser capabilities. However, Vos and Gavrila realized that stabilization might be observed with current lasers if circular Rydberg states were used as the initial states[112]. Shortly thereafter, de Boer and co-workers[113, 114] observed the first experimental indication of stabilization using circular Rydberg states of neon. A decrease in total ionization yield with increasing peak laser intensity but constant *fluence* was observed. This disagrees with Fermi's golden rule indicating nonperturbative behavior. Recently, an experiment by van Druten and co-workers has confirmed de Boer's results[115], also ruling out the possibility that the observed stabilization might be due to mechanisms other than adiabatic stabilization.

In this chapter, I investigate stabilization lifetimes and characteristic waveforms in a 2D hydrogen model driven by a high intensity laser. The laser frequencies I consider are well within the predicted stabilization regime. I consider both linear and circular laser polarizations.

7.2   Soft-Core Atomic Model

My model atom is a 2D version of the 1D "soft-core" atom first used by Eberly[116] in studying laser driven hydrogen. This 1D model potential avoids the Coulombic singularity, retains asymptotic Rydberg behavior, and is parity invariant. However, it is only applicable to linear laser polarization. To include arbitrary laser polarizations and to allow transverse diffusion of the wavefunction, I study the 2D version previously considered by Protopapas, Lappas, and Knight[117]. The 2D "soft-core" potential is given by

$$V_{atom} = -\frac{Z}{\sqrt{\alpha^2 + x^2 + y^2}} \qquad (7.1)$$

where Z is the core charge, and α smooths the Coulombic singularity. All quantities are in atomic units (a.u.), unless otherwise noted. The values $Z = 1$, and $\alpha = 0.8$ are chosen so that the ground state has the hydrogen binding energy, -0.5. The laser interaction is

$$V_{int} = g(t)F\left(x\cos(\omega t + \phi) + \epsilon y\sin(\omega t + \phi)\right), \tag{7.2}$$

where $g(t)$ is the laser ramping, and F,ϵ, ω, and ϕ are the laser field, ellipticity, frequency, and initial phase, respectively.

The Schrödinger equation is integrated using the $O(\Delta x^2)$ Crank-Nicholson finite differencing scheme[32, 3]. In order to avoid reflection of the wavefunction at the computational boundaries, I use an imaginary absorbing potential to annihilate any outgoing portion of the wavefunction[118, 37]. The implementation is similar to that used in other multidimensional calculations[108, 109, 117]. The laser interaction is turned on with a sin^2 ramping, with maximum ramping rate proportional to F/n, where n is the number of cycles in the turn-on. For all calculations, I set this ratio to one, *ie.* the laser electric field in a.u. *is* the number of cycles in the turn-on. After the field strength of interest is reached, the intensity is set constant. This is not designed to represent an actual experiment, where atoms would be subject to a pulse of finite duration, but instead is chosen to ensure significant population of the final stabilized state. My method for determination of the stabilized state lifetime is identical to that of Kulander[108]. As the interaction is ramped on, the wavefunction develops an outgoing component. Once this outgoing portion leaves the interaction region, the probability follows a reasonably well defined exponential decay, from which the lifetime is determined.

7.3   Equation of Motion

The quantum mechanical Hamiltonian for the electron interacting with *classical* electromagnetic field is given by

$$H = [\frac{1}{2m}(\frac{\hbar}{i}\nabla - \frac{e}{c}A(\mathbf{r}, t))^2 + e\phi(\mathbf{r}, t) + V(\mathbf{r}, t)] \tag{7.3}$$

where $A(\mathbf{r}, t)$ and $\phi(\mathbf{r}, t)$ are electromagnetic vector and scalar potentials. $V(\mathbf{r}, t)$ represents any other (external) potentials, and m and e are mass and electric charge of the atomic electron. The equation of motion for the electron is simply a Schrödinger equation,

$$i\hbar\frac{\partial\psi}{\partial t} = H\psi \tag{7.4}$$

Several approximations/assumptions are made to the Eqn (7.4): (1) the electromagnetic field is not quantized, (2) transverse gauge is used, i.e., $\phi = 0, \nabla \cdot A(r, t) = 0$, (3) an atomic core potential is smoothed ("soft-core") around the center of the atom to avoid the singularity

problem at the origin, i.e., $V_{atom} = \frac{Z_{eff}}{\sqrt{\alpha^2+r^2}}$ with a core effective charge Z_{eff} and an effective atomic range α, (4) electron is assumed to be spinless, and nonrelativistic, and (5) an electric dipole approximation is made for an atom-laser interaction. Then, the Eqn (7.4) is reduced to

$$i\hbar\frac{\partial\psi}{\partial t} = [\frac{-\hbar^2}{2m}\nabla^2 + \frac{e}{c}\mathbf{r}\cdot\frac{dA}{dt} + V_{atom}]\psi \tag{7.5}$$

where $V_{atom}(x,y) = \frac{Z_{eff}}{\sqrt{\alpha^2+r^2}}$ and the atom-laser interaction part can be rewritten so that $\frac{e}{c}\mathbf{r}\cdot\frac{dA}{dt}$ becomes Eqn. (7.2).

Written in an atomic unit for the numerical experiments, the Schrödinger equation to solve for stabilizations in 2D is given by,

$$i\frac{\partial\psi}{\partial t} = -\frac{1}{2}(\frac{\partial^2\psi}{\partial x^2} + \frac{\partial^2\psi}{\partial y^2}) - \frac{Z}{\sqrt{\alpha^2+x^2+y^2}}\psi + g(t)F\left(x\cos(\omega t + \phi) + \epsilon y\sin(\omega t + \phi)\right)\psi \tag{7.6}$$

Eqn. (7.6) is integrated by the finite difference method using Crank-Nicholson scheme.

The corresponding finite difference equation is given by

$$i\Delta_t^+\psi_{ij}^n = -\frac{1}{2}(\Delta_{xx} + \Delta_{yy})\psi_{ij}^{n+\frac{1}{2}} + (V_{ij}^{n+\frac{1}{2}} - i\nu_{ij}^{n+\frac{1}{2}})\psi_{ij}^{n+\frac{1}{2}} \tag{7.7}$$

where $\psi_{ij}^{n+\frac{1}{2}} = \frac{\psi_{ij}^{n+1}+\psi_{ij}^n}{2}$, and the wavefunction and the potential are descretized by

$$\psi_{ij}^n = \psi(x_i, y_j, t^n) \tag{7.8}$$

$$V_{ij}^n = -\frac{Z}{\sqrt{\alpha^2+x_i^2+y_j^2}} + g(t^n)F(x_i\cos(\omega t^n + \phi) + \epsilon y_j\sin(\omega t^n + \phi)) \tag{7.9}$$

Annihilation boundary condition is implemented via an imaginary potential, ν. ν damps out any outgoing part of the wavefunction.

7.4   Stabilization Lifetime

My primary result is shown in Fig. 7.1.

Here, I plot the lifetime of adiabatically stabilized g.s. hydrogen, as a function of laser field strength, for both linear and circular laser polarization. The laser frequency is $\omega = 1.2$. The circularly polarized case shows a dramatic increase in lifetime as the field is increased, indicating strong stabilization. The linearly polarized case also demonstrates increasing lifetime with increasing field strength. The remaining normalization as a function of time (in laser cycles), from which the lifetimes are determined, are shown in Fig. 7.2 and Fig. 7.3.

As seen in these figures, the probability inside the norm box remains constant initially. This corresponds to the finite amount of time required for any portion of the initial wavefunction to propagate to the edge of the norm box. The remaining normalization then transitions to an exponential decay as the ionization front traverses the norm box boundary. In order to visualize the stabilization dynamics, I show snapshots of typical probability densities for the adiabatically stabilized states in the laboratory frame. In Fig. 7.4 I show the probability density for field strength $F = 10$ and linear laser polarization.

I find the characteristic dichotomous waveform, with probability peaks separated by $\approx 1.3\alpha_o$. This structure oscillates back and forth between the turning points, while undergoing an overall decay. As seen in the snapshot, the peak heights are unequal. Time series analysis reveals that the maximum probability alternates between peaks in step with the oscillation. This indicates that I have populated a superposition of Floquet states during the turn-on[119]. In Fig. 7.5 I show the probability density for $F = 3.75$ and circular laser polarization.

There appears to be a single peak with a tightly wound spiral tail. This structure is similar to that found by Patel, Protopapas, Lappas, and Knight[120], using the same model, laser frequency $\omega = 1.0$, and field strength $F = 15$. However, they find a ring of enhanced probability at the excursion parameter $\alpha_o = 15$. Time series analysis reveals a similar effect for my parameters. The central peak is actually double peaked, with one maxima at the origin, and the other circling about the origin at my excursion parameter $\alpha_o \approx 2.32$. Thus, I find the characteristic stabilized waveform, when the laser polarization is circular, will consist of some probability trapped near the core and some probability trapped near the classical excursion parameter. The relative amounts of population trapping will depend on the laser ramping, field strength, and frequency.

As mentioned previously, full 3D calculations of stabilized g.s. hydrogen lifetimes computed using HFFT[110] and a finite difference technique[108] differ by an order of magnitude. These computations assume linear laser polarization and laser frequency $\omega = 1.0$. For comparison purposes, I have calculated stabilized state lifetimes using my 2D model with identical assumptions. For laser fields $F \approx 1.0 - 4.0$, I find an order of magnitude larger lifetimes than those found in the 3D computations. However, for fields $F \approx 6.0 - 13.5$, the 2D lifetimes agree fairly well with the 3D lifetimes. (see Table 7.1).

The discrepancy could be due to a number of factors inherent to the 2D "soft-core" model, such as the lack of diffusion along the photon direction or the decreased maximum electron acceleration.

Table 7.1: Comparison of stabilized state lifetimes calculated for hydrogen in 3D, with lifetimes calculated using the 2D model. The 3D computations use HFFT[110] and finite differencing[108]. The laser has frequency $\omega = 1.0$ and linear polarization. All quantities are in a.u.

α_o	3D HFFT	3D finite diff.	2D finite diff.
1.2	≈ 7.7	31.8	≈ 56
2.4	≈ 28.7		≈ 83
3.4		47.5	≈ 170
6.75		275.6	≈ 343
13.5		1117.3	≈ 910

7.5   High Harmonic Generation

The radiation of harmonics of the driving field as the electron interacts periodically with the core is now well confirmed signature of stabilization. In Fig. 7.6, I show the dipole radiation spectra for linear laser polarization, as intensity is increased.

For lower field strengths $F \approx 1.0 - 2.0$, there is no significant harmonic production. However, as field strength is increased to near 6.0, I see the onset and increase of third harmonic generation. The lack of even harmonics is due to my relatively slow ramping rate. For field strengths $F \geq 7.0$, I also see the fifth harmonic signature.

7.6   Dynamical Nature of Stabilization

Fig. 7.7 shows the remaining normalization as a function of time (1 laser cycle is $t=5.236$), for linear laser polarizization. The different curve corresponds to the different turn-on cycle, N. For $N \geq 3$, the lifetime is the same, but as N goes down below 2, lifetime estimation decreases.

Fig. 7.8 shows a dipole moment in x-direction, d_x, as a function of time for an instant turn-on, i.e., zero turn-on cycle. The corresponding HHG distribution is in Fig. 7.9. There is a clear signature for the third order harmonics. One can also see the *second* order harmonics due to the non-adiabatic turn-on.
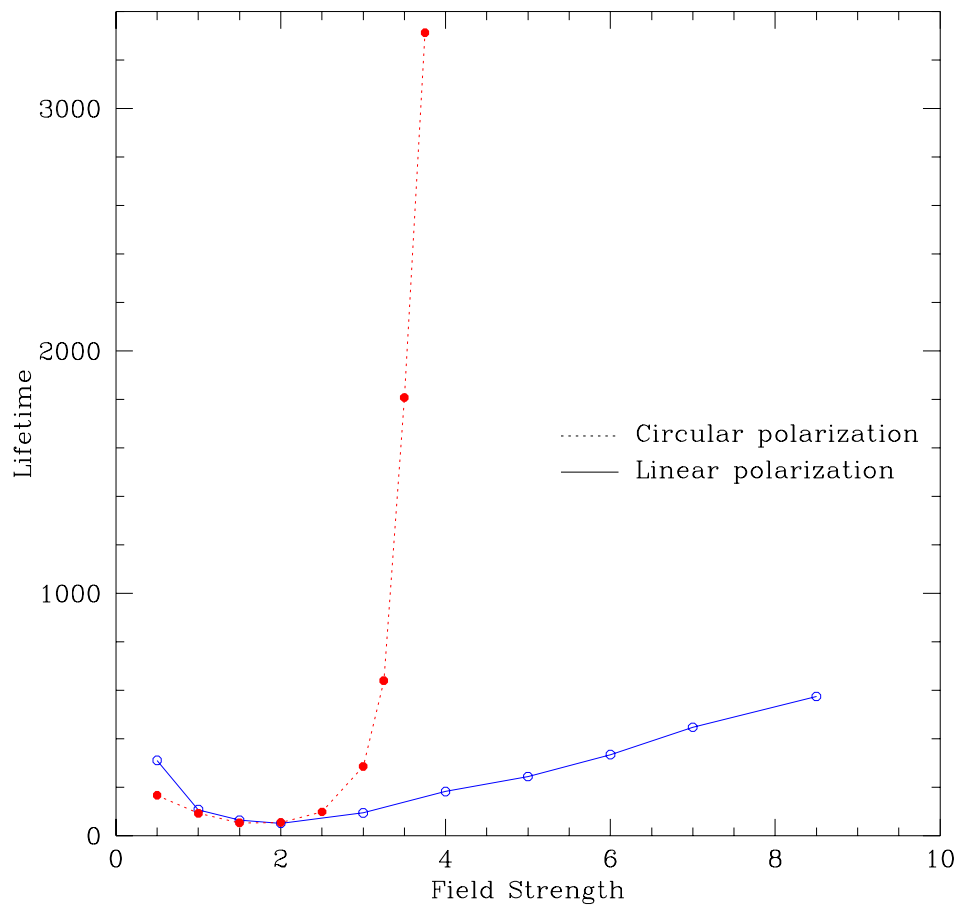
Figure 7.1: Lifetime (a.u.) as a function of laser field strength (a.u.) for adiabatically stabilized 2D hydrogen. The laser frequency is $\omega = 1.2$ a.u. Lifetimes are determined via an exponential fit to the remaining normalization as a function of time, shown in Fig. 7.2 - 7.3.
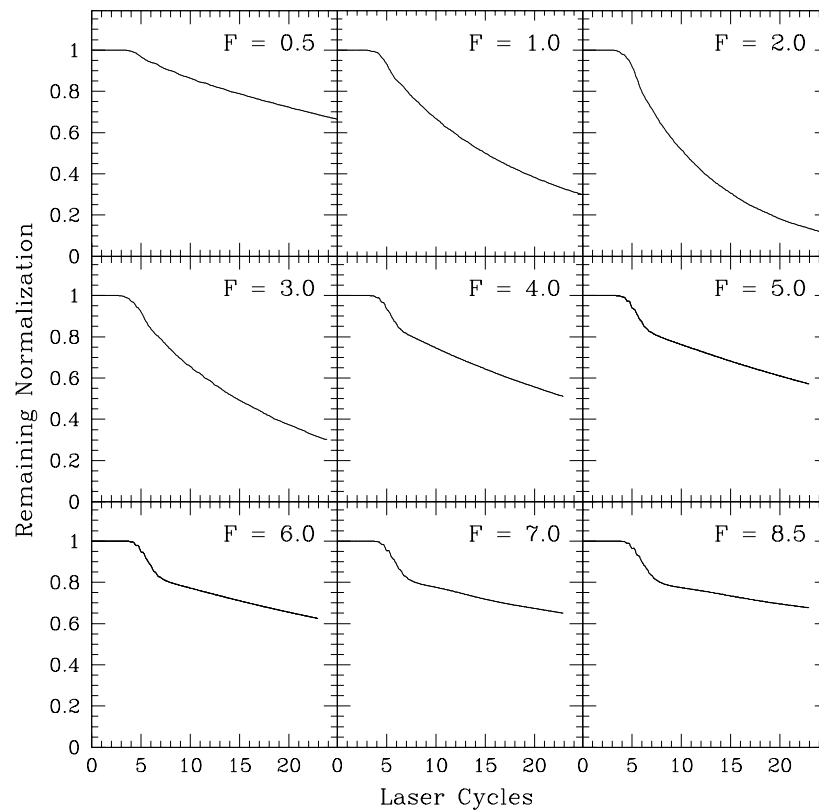
Figure 7.2: Remaining normalization as a function of time (laser cycles), for linear laser polarizization. For final field strength $F \leq 2.0$, there is no apparent stabilization. However, as the final field strength increases above 3.0, transient ionization is suppressed by a slower exponential decay, indicating stabilization.
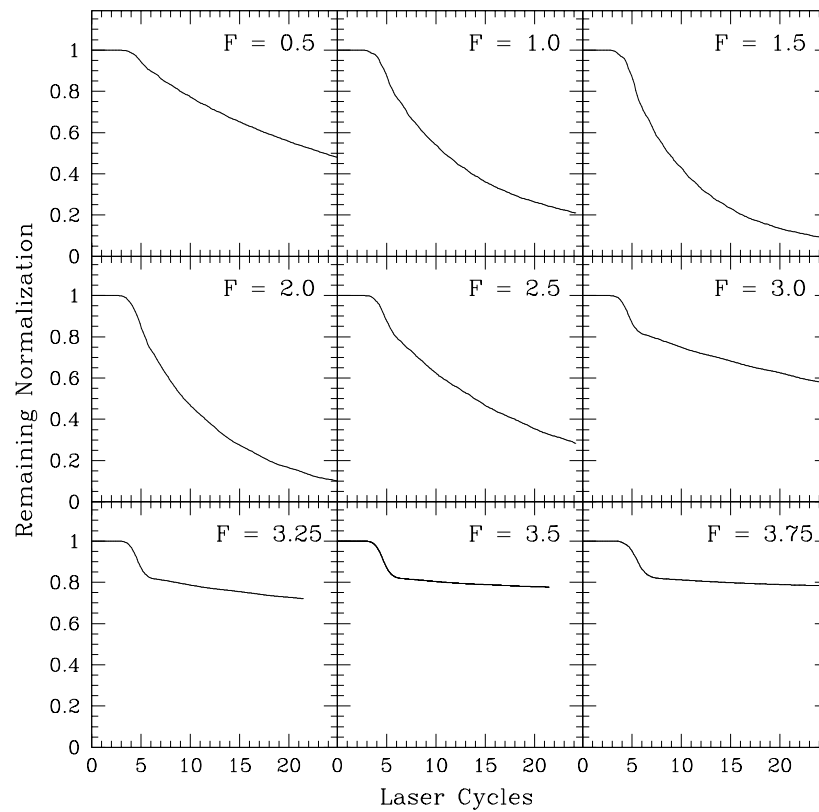
Figure 7.3: Remaining normalization as a function of time (laser cycles), for circular polarization. Again, for final field strength $F \leq 2.0$, there is no apparent stabilization. As final field strength increases above 2.5, the decay rate undergoes a dramatic decrease, characteristic of strong stabilization.
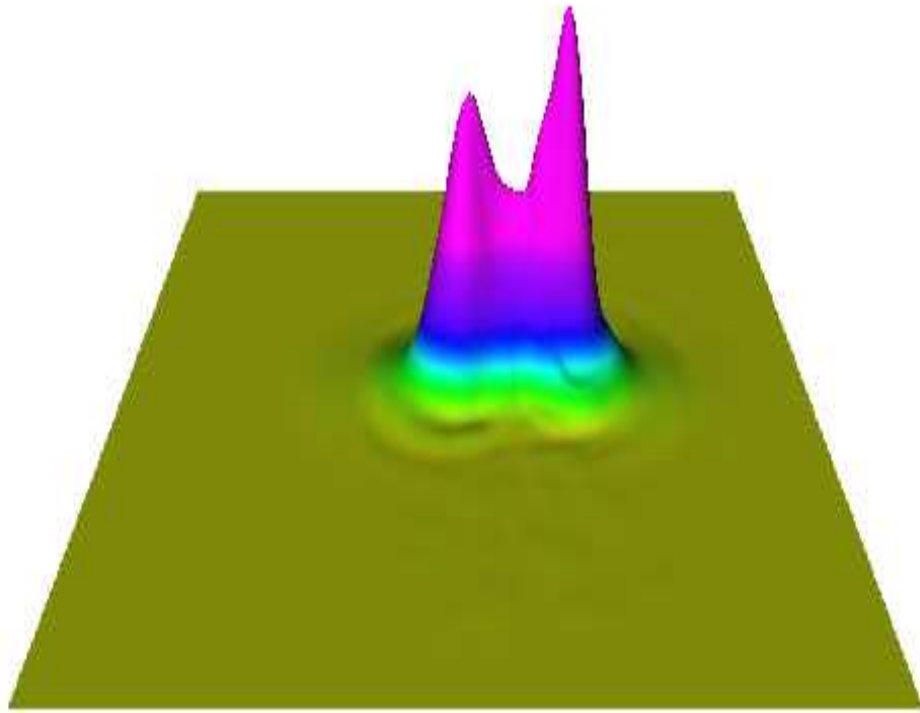
Figure 7.4: Snapshot of the probability density in the laboratory frame for linear laser polarization. The field strength is $F = 10.0$, and the time is $t = 67.5$ a.u., corresponding to approximately 13 laser cycles. The x and y values shown range from -30 to $+30$. We see the dichotomous wavefunction characteristic of stabilization.
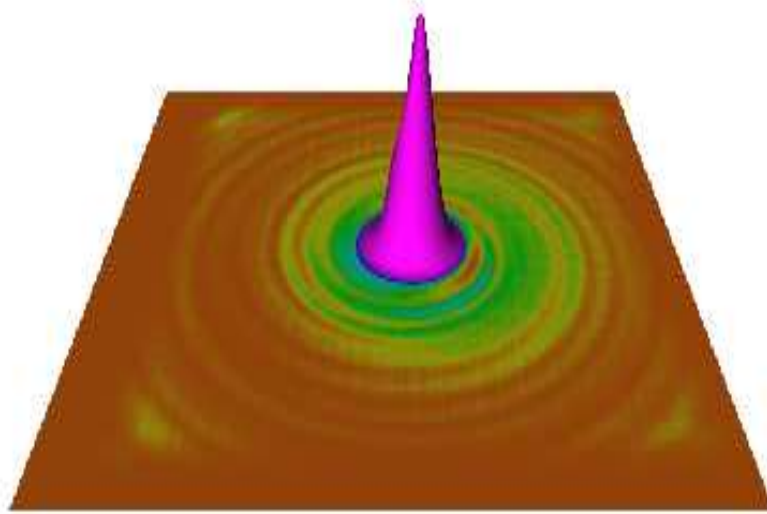
Figure 7.5: Snapshot of the probability density in the laboratory frame for circular polarization. The laser field strength is $F = 3.75$, and the time is $t = 46.875$ a.u., corresponding to approximately 9 laser cycles. The x and y values shown range from -24 to $+24$. Probability is peaked near the origin, with spiral tail.
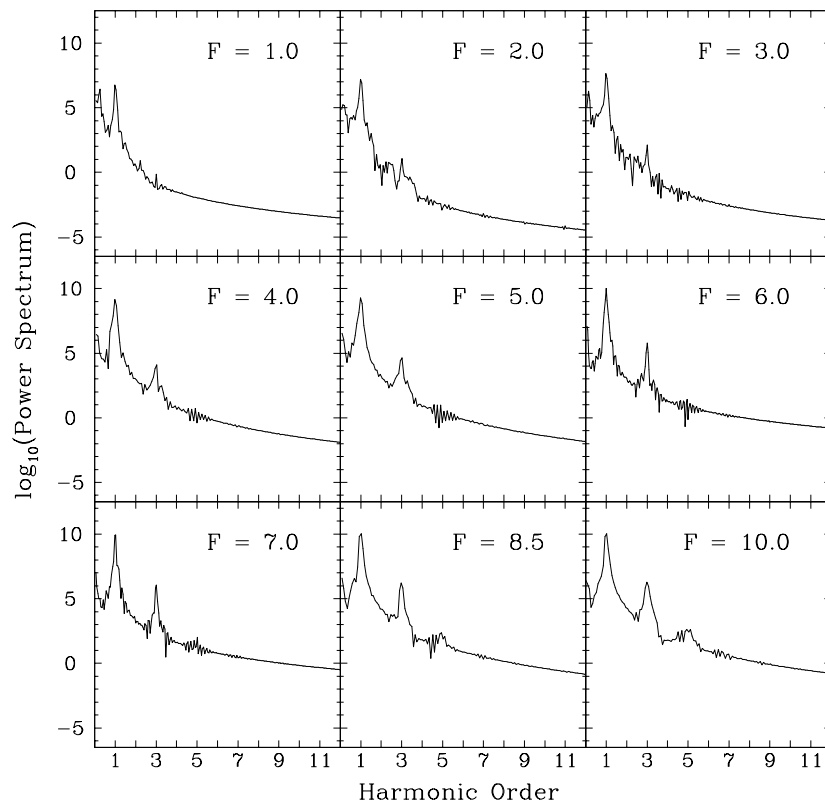
Figure 7.6: Harmonic signature of stabilization. The laser polarization is linear. For field strength $F \approx 1.0$, the dipole radiation spectra shows no significant radiation. However, as field strength is increased to 6.0, we see the onset and increase of the third harmonic generation. For field strengths $F \geq 7.0$, we also see the fifth harmonic signature.
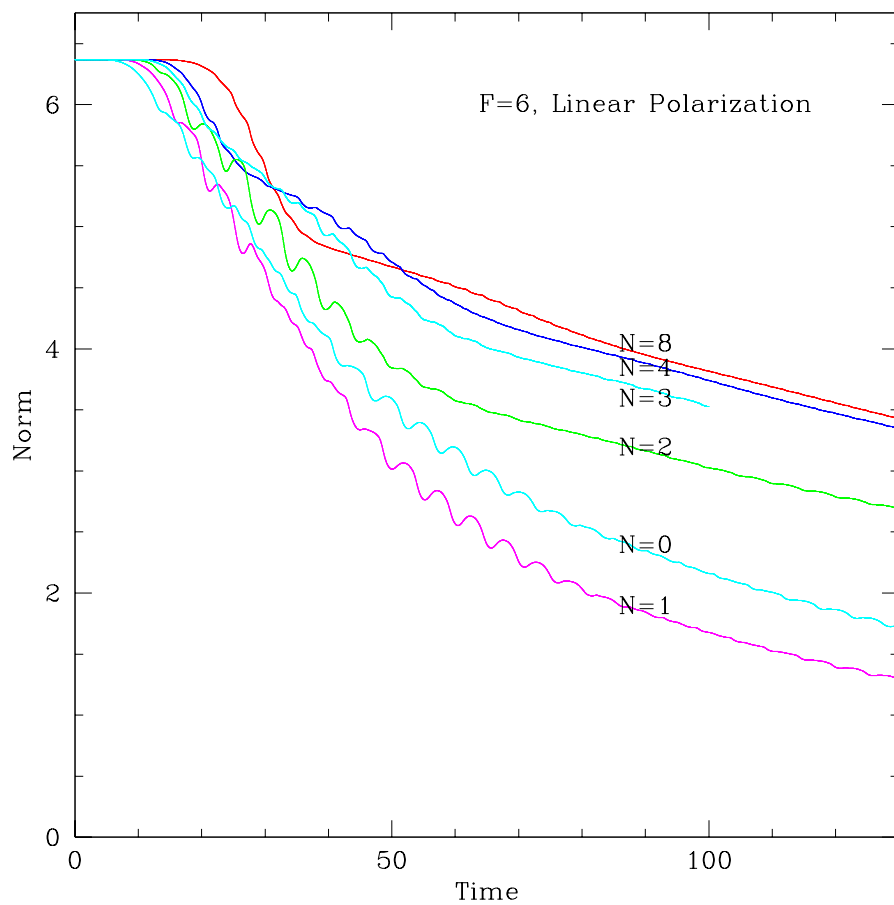
Figure 7.7: This figure shows remaining normalization as a function of time for different turn-on cycles, N. The runs are done with field strength $F = 6$ in linear laser polarization. (1 cycle is t=5.236.)
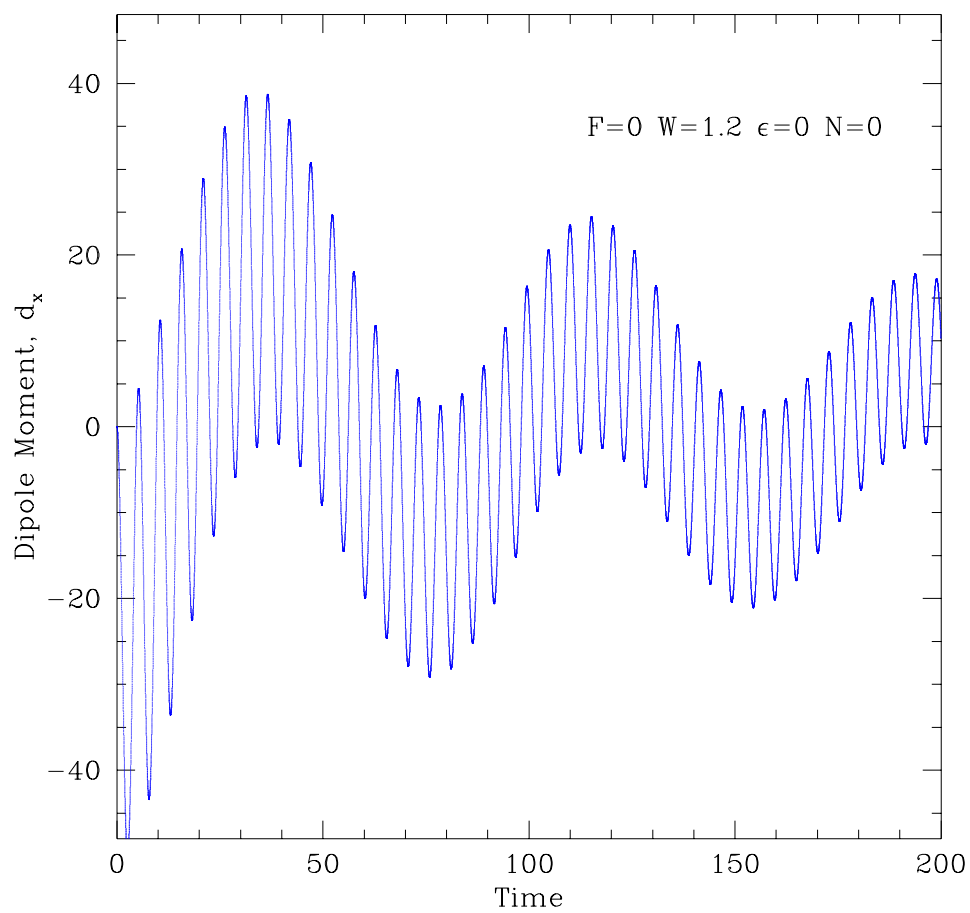
Figure 7.8: This figure shows a dipole moment, d_x, as a function of time. Parameters are $F = 6$, $\omega = 1.2$, and a turn-on cycle, $N = 0$.
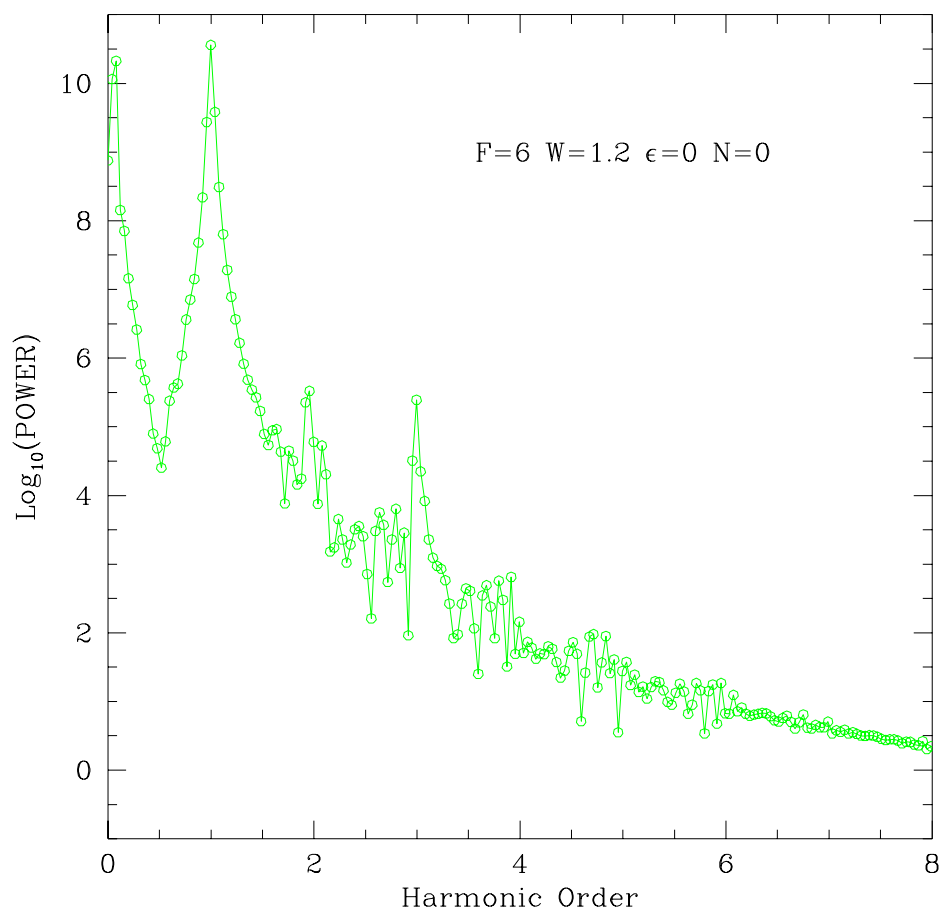
Figure 7.9: This figure shows a high harmonic generation, calculated from the dipole moment data in Fig. 7.8.

Chapter 8

Adaptive Mesh Refinement Techniques

8.1 Introduction

Adaptive mesh refinement (AMR) techniques are crucial for the numerical solutions of problems which have large dynamical ranges. The usual uni-grid approach becomes inefficient when some regions of the computational domain become hard to resolve with a fixed distribution of grid points. If the finer grid is used at the start of calculations, the sharp features may be resolved, but grid points in smoother area might be wasted. Another problem is that in general one does not know *a priori* when and where the high resolution is required during the time evolution of the solutions.

This situation is true not only for numerical relativity but also for other computational physics problems. The basic idea of AMR is to "adapt" the grid structure to the features of the solution, in order to achieve a specified accuracy with minimal use of computational resources.

In this Chapter, I briefly review the Berger and Oliger AMR Scheme [121] for finite difference methods, and discuss some of the issues which arise in AMR applications. I have implemented and tested general algorithms for use in AMR work [122], including 2D and 3D clustering routines and initial regridding procedures.

8.2 Berger and Oliger Scheme

The basic idea of the Berger and Oliger (BO) scheme [121, 123] is to use multiple levels of locally-uniform grids. This scheme allows a different local scale of discretization to be used in different parts of the computational domain, typically in order to keep the local truncation error, τ, below some pre-specified threshold.

Here I adopt the "minimal" Berger and Oliger scheme [124]. The minimal Berger and Oliger scheme uses a single computational coordinate system. It has one globally uniform coarse grid which covers the entire computational domain and an arbitrary number of coordinate-aligned, nested, locally uniform fine grids (arranged in a hierarchical fashion).

Whether or not a fine grid needs to be generated depends on the truncation error estimation. Once the grid points that require refinement are identified, locally uniform fine grids are generated by clustering those grid points into rectangular refinement regions. Grid refinements are done in time as well as in space.

8.3 Local Truncation Error Estimation based on Shadow Hierarchy

I adopt the idea of Local Truncation Error (LTE) Estimation based on the Richardson extrapolation [125] as a refinement criteria. Consider a 2-level update explicit scheme with a finite-difference update operator Q. I use u^n to denote a solution of the original PDEs and $\hat{u}^n$ a finite difference solution. Then, at a given resolution, h, the advanced-time solution $\hat{u}^{n+1}$ is given by:

$$\hat{u}^{n+1} = Q_h \hat{u}^n \tag{8.1}$$

I then assume a Richardson expansion of the finite difference solution for a second order differencing scheme,

$$\hat{u}^n = u^n + h^2 e_2^n + \cdots \tag{8.2}$$

where the error function e_2^n is *independent* of the grid spacing, h. The local truncation error is given by

$$u^{n+1} - Q_h u^n = h^3 \tau_2 + \cdots \tag{8.3}$$

It u is smooth enough, then by taking two time steps with the operator, Q,

$$u^{n+2} - Q_h^2 u^n = 2h^3 \tau_2 + \cdots \tag{8.4}$$

Now, using the same operator as Q but based on grid size of $2h$,

$$u^{n+2} - Q_{2h} u^n = (2h)^3 \tau_2 = 8h^3 \tau_2 + \cdots \tag{8.5}$$

Then, the local truncation error, τ, is estimated by

$$Q_h^2 u^n - Q_{2h} u^n = -6h^3 \tau_2 + \cdots \equiv \tau \tag{8.6}$$

Including only the leading order terms, the local truncation error can be approximately computed using $\hat{u}^n$ at a given time t^n,

$$\tau \simeq Q_h^2 \hat{u}^n - Q_{2h} \hat{u}^n \tag{8.7}$$

Despite some problems, this procedure of estimating the LTE has been quite effective [124]. One does not have to know the exact form of truncation error to apply it, and it is relatively independent of the PDE or the difference methods which are used.

Implementation of this idea can be done straightforwardly. The simplest approach uses a temporary array to save the grid functions at the current level because the current data stored will be destroyed when two time steps are taken on the original grid. After the LTE is calculated, the temporary array is deallocated. One drawback of this approach is a dynamical memory-doubling at the regridding time.

Choptuik [126] has suggested an alternative approach based on the idea of a *shadow hierarchy*. In this new approach, the numerical integration is done on a 2-to-1 coarsened version of the base Berger and Oliger grid hierarchy, as well as on the base hierarchy itself. At regridding times, the truncation error is calculated simply by subtracting the data on the base hierarchy from corresponding values on the shadow hierarchy. This approach also significantly simplifies the code for the local truncation error estimation procedure compared to the memory-doubling approach.

Pseudo code for a typical AMR program using a 2-level differencing scheme and using a shadow hierarchy is shown in Fig. 8.1.

8.4   Regridding Procedure

The regridding procedure consists of several steps [121].

- Local truncation error estimation

- Flagging points needing refinement

- Clustering the flagged points

- Subgrid generation for each cluster

- Initialization of subgrids

The local truncation error estimation has already discussed in the previous section. Now, when it comes to a time for a regridding at the given level, l, the LTE is computed for all level equal to or higher than level l. Once LTE is computed, the regridding is recursively done starting from the finest level to the current level. This way, grids are generated using the most accurate error estimates taken from the finest grid at any given point. This also ensures that grids are properly level-nested.

The first step for a regridding is to identify those grid points at level, l, which need to be in a finer grid at level $l+1$. Using a pre-determined truncation criteria, τ_0, I flag those points $\mathbf{x}$ for which $\tau(\mathbf{x}) \geq \tau_0$. In this step, grid points in level l grids which are interior to grids at level $l+2$ are flagged even if $\tau(\mathbf{x}) < \tau_0$ to assure a properly nested grid structure.

The next step is to cluster flagged points by coordinate-aligned rectangular bounding boxes. The original Berger and Oliger algorithm [121] allows arbitrary alignment of the bounding boxes. Here I follow Berger and Collela [123] and restrict subgrids to those whose boundaries are all aligned with coordinate directions. The clustering routine is the most challenging part of the regridding procedure, particularly for 2/3D calculations. Different clustering algorithms have been suggested and tested and I will them in more detail in the following Section.

Once the clusters are determined, subgrids are allocated and the data for each grid function on the subgrids are initialized. This initialization is done by interpolation from the next coarser grid or transferral from the old grids at the same level which overlap with the newly created subgrids.

I have implemented a consistent initial-time regridding procedure [127]. The original $t = 0$ regridding approach "turns on" refinement, one level at a time during the early stages of an evolution [128]. The new approach ensures that an appropriate level of discretization (again as determined by LTE estimates) is used at the initial time, as well as at all subsequent times.

Regridding at the initial time, $t = 0$, is a little bit different from the regridding at the generic time. This is because there is no pre-existing nested grid structure at $t = 0$. Therefore one has to create a refinement structure from the "bottom up". In other words, the level $l = 1$ grids are generated using truncation error estimates on the $l = 0$ base grid. Then, if necessary level $l = 2$ grids are computed from level $l = 1$ LTE's, level $l = 3$ grids are computed from level $l = 2$ LTE's, etc. I also take advantage of the shadow hierarchy to generate $t = 0$ truncation error estimates, first on the base level, then on as many levels as are necessary to ensure that the initial LTE is below the threshold throughout the computational domain.

The only significant difference between the regridding procedure at the initial time and later times is that, because the shadow hierarchy approach is destructive (at each stage (level) of the regridding, we have to advance the finest-level equations of motion two time-steps), we must reinitialize the $t = 0$ data (and $t = -dt$ data for 3-level schemes) on each final component of the grid hierarchy. This may involve re-reading initial data files, or recomputing some analytic specification of the $t = 0$ data, but it seems a safe assumption that reinitialization will always be possible, and, significantly, the approach does not require additional memory for start-up. In addition, normally the initial data is known to higher accuracy than is anticipated from the evolved data. Therefore the re-initialization by re-reading will at the initial time often result in better data than the data that is generated by interpolations.

The problem of memory doubling arises at the initial time, too. Fortunately, the idea of the shadow hierarchy can be applied to the initial time. The basic idea is that the initialization is done twice on each level by reading in the initial data set. The LTE is computed using the shadow hierarchy and the initial data is read in before and after the LTE estimation. This way, one can avoid memory doubling and inaccurate specification of data from interpolation. Pseudo code for this algorithm is shown in the "Initial Data" part of Fig. 8.1.

8.5   Testing of Clustering Algorithm

Among other things, the success of an AMR program depends on an efficient clustering algorithm. The main problem for any clustering algorithm is to define an optimal set of bounding boxes enclosing all the flagged points. A good clusterer should satisfy the following conditions [129].

- There should be as little unnecessarily refined area as possible.

- There should be as few bounding boxes as possible.

- The bounding boxes should cover all flagged points.

- The algorithm should be fast.

Finding a general and robust method is still an open problem. In fact, the first two requirements compete with each other.

Several different clustering methods have been used in conjunction with the BO algorithm [129]. For example, the *bisection method* checks the efficiency of each rectangle, where the efficiency is defined as the ratio of flagged points to the total number of coarse grid points in the new rectangle. If the efficiency is less than a preselected threshold, the rectangle is bisected along the longest direction of the rectangle to generate two smaller rectangles. The process is repeated recursively on each of the two new rectangles until all generated rectangles satisfy the threshold. A drawback of this method is that it uses no information about the locations of the flagged points so it tends to generate nonoptimal grid structures, and is known to create clusters even if no natural clusters exist. To cure this problem, the bisection step usually is followed by a merging step, wherein neighboring rectangles are merged into larger ones if the result continues to be acceptably efficient. There are various other methods such as the minimal spanning tree algorithm, but many of the older algorithms produced less than optimally efficient grids which tended to overlap too much. Better grids were easily created by hand.

Berger and Rigoutsos [129] suggested a new algorithm based on the idea of signatures [130] and edge detection [131]. In 2D grids, the horizontal and vertical signatures, $H(x)$ and $H(y)$, are defined as

$$H(x) = \int_y f(x, y) dy \qquad (8.8)$$

and

$$H(y) = \int_x f(x, y) dx \qquad (8.9)$$

respectively. $f(x, y)$ represents a flag information, i.e., $f(x, y) = 1$ where (x, y) is flagged, and zero otherwise. This algorithm first looks for chains of 0's or "holes", i.e., x's or y's for which $H(x) = 0$ or $H(y) = 0$ are satisfied. The occurrence of such holes provides obvious choices for splitting the input grid into a number of rectangles. Thus, the main idea of this approach is to to look for zero crossings in the second derivative of a signature (inflection points). The input grid is then partitioned into two grids at the biggest inflection point as is illustrated in Fig. 8.2. This algorithm is applied only to those rectangles that are still inefficient.

I have tested two clustering routines based on Berger and Rigoutsos's algorithm. One is a `FORTRAN 77` implementation by Reid Guenther [132] and the other is a `C++` implementation due to Paul Walker [133]. Both routines were tested within a `DAGH`-based driver code [122].

The tests [134] are done by generating a 3D integer array defining a flag (or characteristic) function (1s and 0s) and calling the clusterers with the flag function as an input. Thus far, the clusterers have been tested with several test-flag arrays which roughly model the flag arrays one anticipates encountering in the evolution of one or two compact objects (black holes, boson stars, etc). These include arrays whose flagged points define one or two spheres or one or two spherical shells. For diagnostic purposes I monitored the overall efficiency, surface-to-volume ratio, total number of real boundary points and total number of interface boundary points. I used Explorer modules [135] to visualize the output and to aid in the analysis.

Figs. 8.3, 8.4 and 8.5 show some of test results: bounding boxes generated by a 3D clusterer for given flagged points denoted by dots.

In general, both clusterers show similar behavior. Efficiencies were almost identical (differences typically less than 10%), but the C++ routine tends to generate more bounding boxes (regions requiring refinement) than the F77 routine. Both routines handled spheres relatively well, but for the spherical shells, both routines generated many boxes (~ 100) with very low efficiency (typically below 15%). It should be noted however, that this problem was

anticipated in the original decision to use the minimal Berger and Oliger algorithm. The basic claim is that, overall, areas requiring refinement in a binary-merger problem will tend to be volume-filling (i.e. 3D rather than 2D). Real evolutions will be required to fully test this hypothesis; in the meantime it appears that the clustering routines may be able to be further improved and I am working towards that goal.

```
MAIN
 Initial Data; Initial regridding
  initialize grid structure; main and shadow hierarchy
  initialize data on main/shadow base grid; l = 0
  WHILE( new level )
   IF( l .ne. L ) THEN
    take 2 steps on main, take a step on shadow, swap pointers
    local truncation error estimation
    IF( new finest level .gt. current level ) THEN
     regrid; clustering
     initialize data on new fine main/shadow grids
    ENDIF
    re-initialize data on current main/shadow grids
    IF( new finest level .ne. L ) then
     take a step forward on main/shadow grid for BC for a fine level
    ENDIF
   ENDIF
  END WHILE
 END Initial Data

 Evolution; time step(l)
  FOR (iter = 1; iter <= niters; iter++)
   FOR (i=0;i<NoIterations;i++)
    IF( regridding time AND l < L )
      local truncation error estimation
      IF( nwflev .gt. curlev ) THEN
        regrid; clustering
      ENDIF
    ENDIF
    take a step on main grids
    interpolate boundary-values as necessary
    IF( mod(lsteps(l),2) .eq. 0) THEN
      update shadow grids from main grids
      take a step on shadow grids
    ENDIF
    IF( l < L ) THEN
      time step(l+1)
    ENDIF
    IF( l >0 AND time-aligned with l-1 ) THEN
      restriction on main/shadow grids
    ENDIF
   END FOR
  END FOR
 END Evolution
END MAIN
```

Figure 8.1: Pseudo code for a general Berger and Oliger AMR program based on the idea of shadow hierarchy.
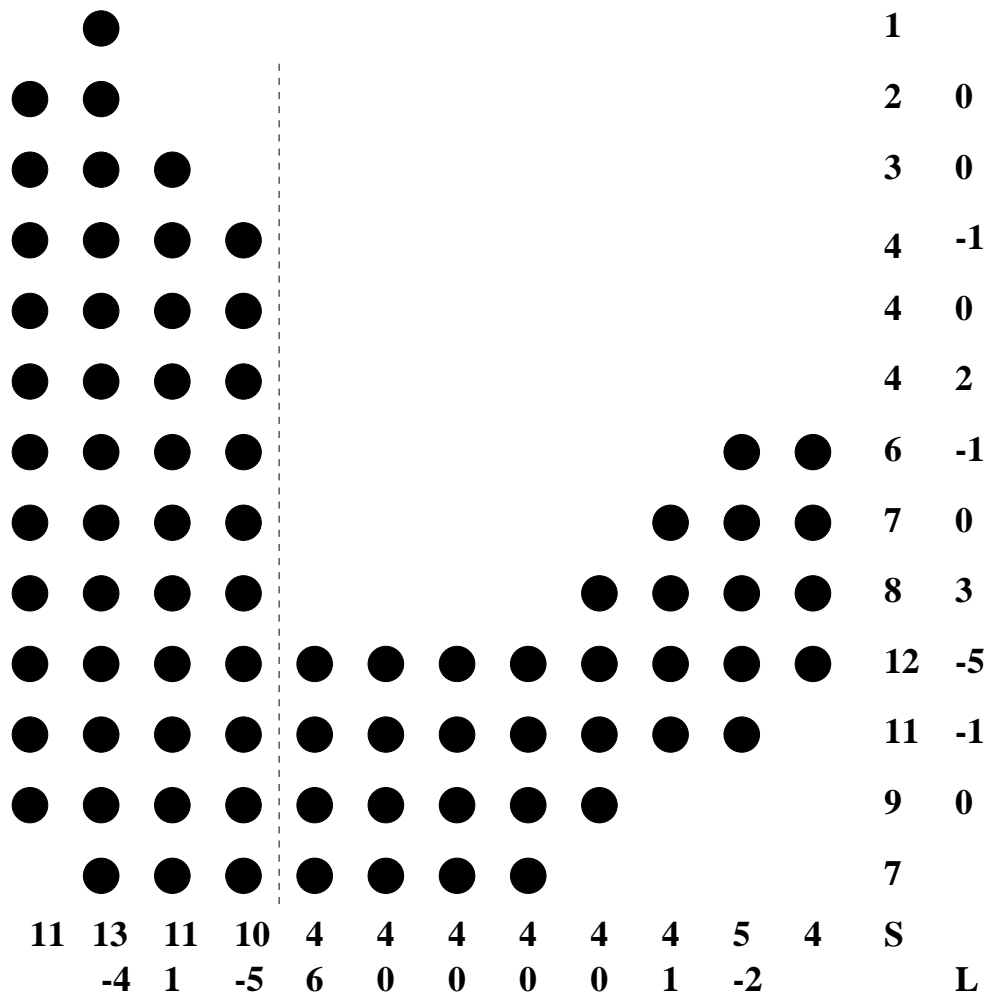
Figure 8.2: Computation of the signature and Laplacian from a given set of flagged points. The Laplacian indicates where to divide the cluster. The rectangle is partitioned at the biggest inflection point.
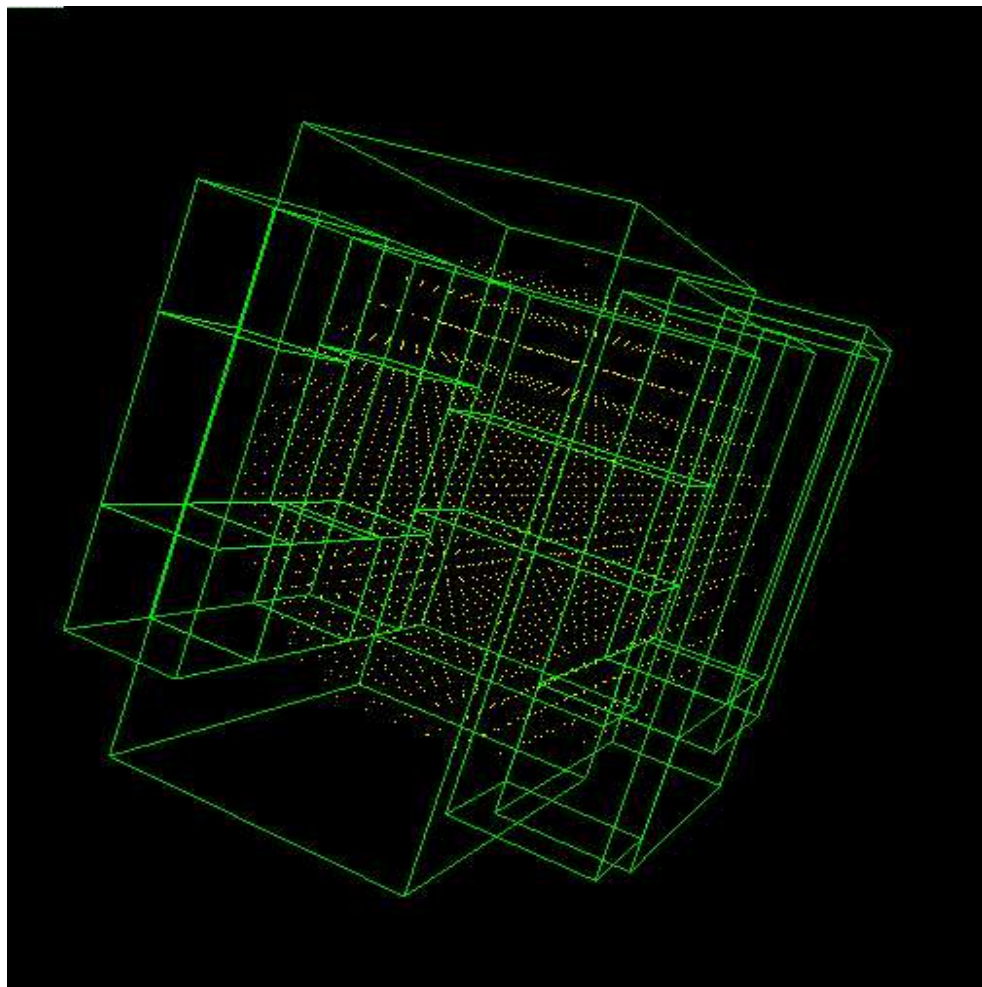
Figure 8.3: Bounding boxes generated by the F77 version of the clusterer. The flagged points make up a single sphere.
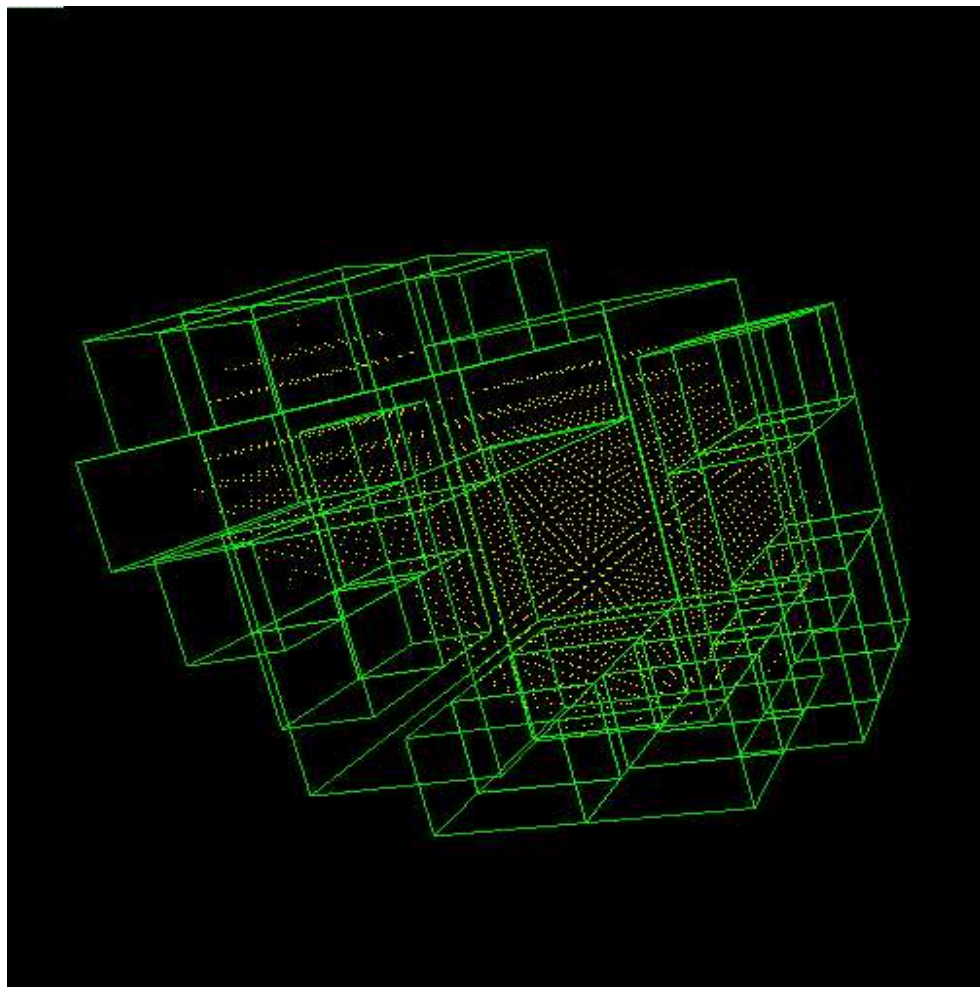
Figure 8.4: Bounding boxes generated by the F77 version of the clusterer. The flagged points make up two overlapping spheres.
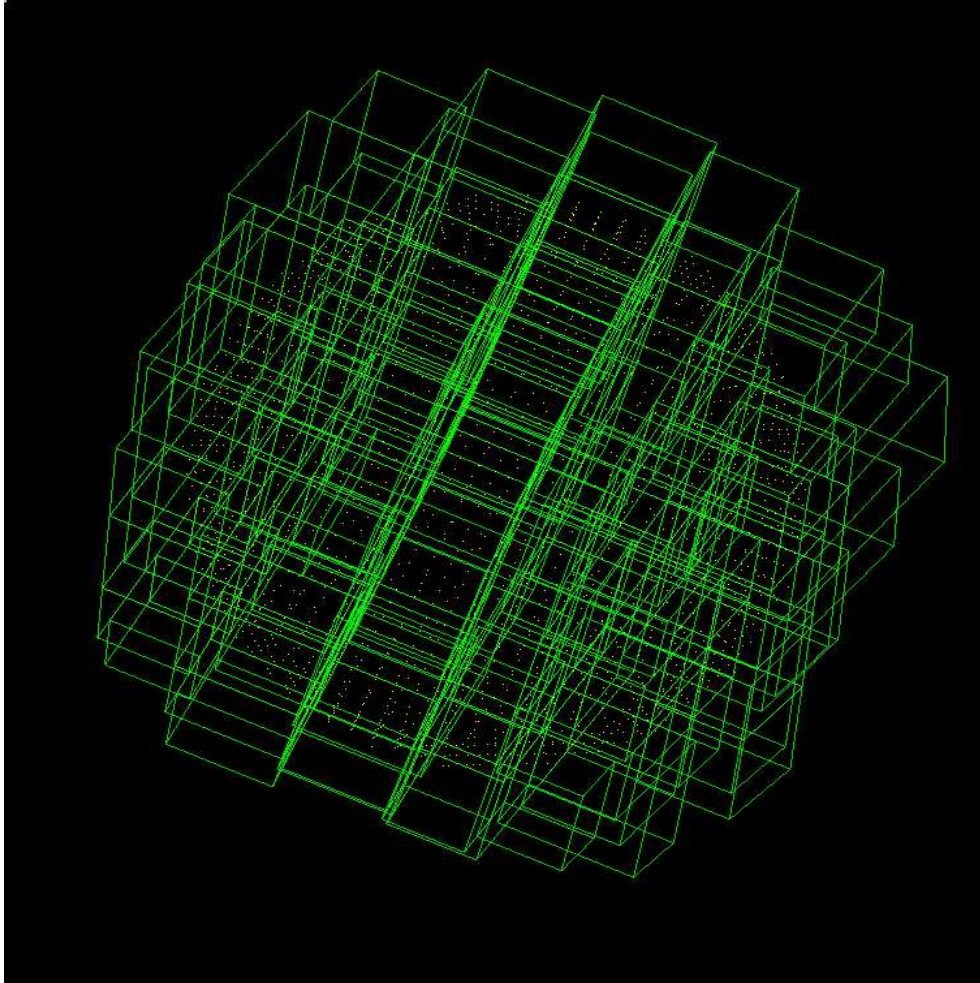
Figure 8.5: Bounding boxes generated by the `C++` version of the clusterer. Here the flagged points make up a single shell.

Chapter 9

Conclusion

In this chapter, I summarize my results and briefly outline possible future research directions.

I have implemented uni-grid Newtonian boson star codes in 2D (axially symmetric, and slab symmetric) and 3D spatial domain. The codes have been thoroughly tested using single stationary stars, moving stars, spinning stars, and binary star systems. Even though I do not anticipate any "new" physics out of the codes, they will continue to serve as test-bed codes against which the full general relativistic boson codes can be compared in weak field limits. They will also provide excellent test problems for any AMR programs. Since the codes are solving the Schrödinger equation, they can also be applied to other research problems which require numerical solutions of the Schrödinger equation. My future goal is to implement an AMR version of one or more of these codes using currently available AMR packages.

I started research on 3D general relativistic boson stars with the hope that by the time the uni-grid code was fully developed, a package would be available which would allow almost automatic parallelization and adaptivity of serial uni-grid codes. At the moment, I am still struggling with stabilizing a single boson star. This is partly due to unstable outer boundary conditions for the geometry variables. The question of coordinate conditions still remain even though the maximal slicing or K-driver condition seems to provide a good lapse condition for single stationary stars. I am going to closely examine the single stationary star runs with various outer boundary conditions. Then once the stable runs are achieved, testing will be done with a moving star. I will also examine shift conditions and work towards stable evolution of binary boson stars. Use of a reliable AMR program will be a crucial part of this research.

The applications of my Schrödinger codes to other physics problems have also proven useful as can be seen from the two examples I studied in this thesis. I showed how to manipulate BECs with an optical lattice and I studied effects of atom-atom interactions on the quantum transport properties of BEC. I also observed Bloch oscillations of BEC in an accelerating optical lattice. The study of interacting ultra-cold atoms or Bose-Einstein condensates will continue to be an intensive area of research in the atomic-molecular-optical and

condensed matter physics communities. Optical lattices provide an excellent vehicle in which to study quantum transport. Some of the concepts are already well-established in condensed matter physics. One exciting thing about BECs/ultra-cold atoms is that theoretical calculations can be directly compared to the experiments. This has not been always possible with solid state systems. I plan to examine Landau-Zener tunneling and Wannier-Stark ladders more closely in the 1D system I studied here and eventually work with a realistic 3D model.

The study of atoms interacting with a very intense laser field has revealed many surprising nonlinear effects. Using 2D model atoms which allow one to study the effects of non-linear polarizations, I was able to demonstrate stabilization of atoms for both linearly and circularly polarized light field. Solving a time-dependent Schrödinger equation makes it possible to study the dynamic nature of stabilization. I will also pursue research in that direction.

Testing and evaluations of each component of an AMR algorithm is crucial and necessary for a validation or a development of a reliable AMR program which should be very useful for my future research. I plan to look at the `paramesh` package developed at NASA [136]. I will also work to develop a 3D parallel multigrid solver.

Bibliography

[1] See, e.g., J. J. Sakurai, *Modern Quantum Mechanics*, Reading, MA: Addison-Wedley, 1985; S. Gasiorowicz, *Quantum Physics*, New York: Wiley (1974).

[2] R. Arnowitt, S. Deser, and C. W. Misner, "The Dynamics of General Relativity", in *Gravitation-An Introduction to Current Research*, L. Witten, ed. New York: Wiley (1962).

[3] A. R. Mitchell and D. F. Griffiths, *The finite difference method in partial differential equations*. Chichester: Wiley (1980).

[4] A. Brandt, Math. Comput. **31**, 333 (1977).

[5] A. Brandt, in *Lecture Notes in Mathematics: Multi Grid Methods*, **960**, W. Hackbusch and U. Trottenberg, eds. New York: Springer Verlag (1982).

[6] M. W. Choptuik and W. G. Unruh, General Relativity and Gravitation **18**, 813 (1986).

[7] D.J. Kaup, Phys. Rev. **172** 1331 (1968).

[8] R. Ruffini and S. Bonazzola, Phys. Rev. **187**, 1767 (1969).

[9] M. Colpi, S. L. Shapiro, and I. Wasserman, Phys. Rev. D **57**, 2485 (1986).

[10] M. Gleiser, Phys. Rev. D **38**, 2376 (1988).

[11] J. A. Frieman, G. B. Gelmini, M. Gleiser, and E. W. Kolb, Phys. Rev. Lett. **60**, 2101 (1988).

[12] M. Gleiser and R. Watkins, Nucl. Phys. **B 319**, 733 (1989).

[13] T. D. Lee and Y. Pang, Nucl. Phys. **B 315**, 477 (1989).

[14] E. Seidel and W.-M. Suen, Phys. Rev. **D 42**, 384 (1990).

[15] A. R. Liddle and M. S. Madsen, Int. J. Mod. Phys. D**1**,101 (1992).

[16] P. Jetzer, Phys. Rep. **220**, 163 (1992).

[17] S. Yoshida and Y. Eriguchi, Phys. Rev. D **56**, 762 (1997).

[18] S. Yoshida and Y. Eriguchi, Phys. Rev. D **55**, 1994 (1997).

[19] F. E. Schunck and A. Liddle, Phys. Lett B **404**, 25 (1997).

[20] F. D. Ryan, Phys. Lev. **D 55**, 6081 (1997).

[21] J. Balakrishna, Edward Seidel and Wai-Mo Suen, gr-qc/9712064.

[22] J. Balakrishna and H.-A. Shinkai, gr-qc/9712065.

[23] D. F. Torres, F. E. Schunck and A. R. Liddle, gr-qc/9803094.

[24] G. L. Comer and H.-A. Shinkai, gr-qc/9708071.

[25] E. W. Mielke and F. E. Schunck, gr-qc/9801063 (1998).

[26] J. W. York, Jr. in *Sources of Gravitational Radiation*, L. L. Smarr, ed. Cambridge, England: Cambridge University Press (1979).

[27] L. L. Smarr, Ph.D. dissertation, University of Texas at Austin (1975).

[28] J. W. York, Jr. and T. Piran, "The Initial Value Problem and Beyond", in *Spacetime and Geometry*, Austin, TX: University of Texas Press (1982).

[29] T. Piran, "Methods of Numerical Relativity", in *Gravitational Radiation*, N. Deruelle and T. Piran, eds. Amsterdam: North-Holland (1983).

[30] T. W. Baumgarte and S. L. Shapiro, gr-qc/9810065.

[31] M. Shibata and T. Nakamura, Phys. Rev. **D 52**, 5428 (1995).

[32] W. H. Press, *et al*, Numerical Recipes: the art of scientific computing. 2nd ed. Cambridge University Press (1992).

[33] M. W. Choptuik, Ph.D. dissertation, University of British Columbia (1986).

[34] M. F. Huq, Personal communication (1997).

[35] S. A. Klasky, Ph.D. dissertation, University of Texas at Austin (1994).

[36] V. A. Baskakov and A. V. Popov, Wave Motion, **14**, 123 (1991).

[37] M. Israeli and S. A. Orszag, J. Comput. Phy. **41**, 115 (1981).

[38] See, e.g., P. J. E. Peebles, *Principles of Physical Cosmology* Princeton: Princeton University Press (1993).

[39] A. Linde, Phys. Lett. **108B**, 389 (1992); A. Albrecht and P. J. Steinhardt, Phys. Rev. Lett. **48**, 1220 (1982); A. Albrecht, P J. Steinhardt, M. S. Turner and F. Wilczek, Phys. Rev. Lett. **48** 1437 (1982).

[40] J. R. Primack, D. Seckel and B. Sadoulet, Annu. Rev. Nucl. Part. Sci. **38**, 751 (1988).

[41] A. Guth, Phys. Rev. **D 23**, 347 (1981).

[42] K. A. Olive, Phys. Rep. **190**, 307 (1990).

[43] R. Friedberg, T. D. Lee, and A. Sirlin, Phys. Rev. **D 13**, 2739 (1976); S. Coleman, Nucl. Phys. **B262**, 263 (1985).

[44] E. Seidel and W.-M. Suen, Phys. Rev. Lett. **66**, 1659 (1991).

[45] E. Seidel and W.-M. Suen, Phys. Rev. Lett. **72**, 2516 (1994).

[46] K. S. Thorne, gr-qc/9706079.

[47] S. Weinberg, *Gravitation and Cosmology*, New York, Wiley (1972).

[48] C. Quigg, *Gauge Theories of the Strong, Weak, and Electromagnetic Interactions*, London: Benjamin/Cummings Publishing (1983).

[49] W. G. Unruh (1982).

[50] R. L. Marsa and M. W. Choptuik, Phys. Rev. **D 54**, 4929 (1996).

[51] M. W. Choptuik, E. W. Hirschmann and R. L. Marsa, in preparation.

[52] The Binary Black Hole Grand Challenge Alliance, Phys. Rev. Lett. **80**, 3915-3918 (1998).

[53] The Binary Black Hole Grand Challenge Alliance, Phys. Rev. Lett. **80**, 2512-2516 (1998).

[54] J. R. Wilson and G. J. Mathews, Phys. Rev. Lett. **75**, 4161 (1995); P. Marronetti, G. J. Mathews, J. R. Wilson, Phys. Rev. **D 58**, 042822 (1998).

[55] J. R. Wilson, G. J. Mathews and P. Marronetti, Phys. Rev. **D 54**, 1317 (1996).

[56] G. J. Mathews and J. R. Wilson, Ap. J. **482**, 929 (1997).

[57] G. J. Mathews, P. Marronetti and J. R. Wilson, Phys. Rev. **D 58**, 043003 (1998).

[58] D. Lai, Phys. Rev. Lett. **76**, 4878 (1996); A. G. Wiseman, Phys. Rev. Lett. **79**, 1189 (1997); P. R. Brady and S. A. Hughes, Phys. Rev. Lett. **79** 1186 (1997), etc.

[59] M. Shibata, T. W. Baumgarte, and S. L. Shapiro, Phys. Rev. **D 58**, 023002 (1998).

[60] K. S. Thorne, Phys. Rev. **D**, to appear; E. E. Flanagan, Phys. Rev. **D**, to appear.

[61] E. E. Flanagan, astro-ph/9811132.

[62] `http://www.npac.syr.edu/projects/bh/`.

[63] L. Smarr and J. W. York, Jr., Phys. Rev. **D 17**, 2529 (1978).

[64] J. Balakrishna, *et al*, Class. Quantum Grav. **13** L135-L142 (1996)

[65] See, e.g., The Binary Black Hole Grand Challenge Alliance, Phys. Rev. Lett. **80**, 1812-1815 (1998).

[66] R. Gomez, M. Hug, L. Rezzolla, A. Abrahams, and M. Rupright, Unpublished notes (1998).

[67] See, .e.g, `http://www.npac.syr.edu/restricted/projects/bh/NewsLetters/Vol_4.2/2.html` or `http://www.npac.syr.edu/restricted/projects/bh/NewsLetters/Vol_4.1/5.html`.

[68] D.-I. Choi and Q. Niu, *submitted to Phys. Rev. Lett.* (1998).

[69] M.H. Anderson *et al.*, Science **269**, 198 (1995).

[70] C.C. Bradley *et al.*, Phys. Rev. Lett. **75**, 1687 (1995).

[71] K.B. Davis *et al.*, Phys. Rev. Lett. **75**, 3969 (1995).

[72] M. Brewczyk, K. Rzążewski, and C. W. Clark, Phys. Rev. A **57**, 448 (1998).

[73] H. Pu and N. P. Bigelow, Phys. Rev. Lett. **80**, 1134 (1998).

[74] J. P. Burke, Jr., J. L. Bohn, B. D. Esry, and C. H. Greene, Phys. Rev. Lett. **80**, 2097 (1998).

[75] C. J. Myatt, *et al.*, Phys. Rev. Lett. **78**, 586 (1997).

[76] T.-L. Ho and V. B. Shenoy, Phys. Rev. Lett. **77**, 3276 (1996).

[77] D.S. Rokhsar, Phys. Rev. Lett. **79**, 2164 (1997).

[78] E. J. Mueller, P. M. Goldbart, and Y. Lyanda-Geller, Phys. Rev. A **57**, R1505 (1998).

[79] K.-P. Marzlin, W. Zhang, and E. M. Wright, Phys. Rev. Lett. **79**, 4728 (1997).

[80] K.-P. Marzlin and Weiping Zhang, cond-mat/9711084.

[81] K. Berg-Sørensen and K. Mølmer(to be published).

[82] M. Raizen, C. Salomon, and Q. Niu, Physics Today July 1997, p.30.

[83] Q. Niu, X.-G. Zhao, G. A. Georgakis, and M. G. Raizen, Phy. Rev. Lett. **76**, 4504 (1996).

[84] M. Ben-Dahan, *et al.*, Phy. Rev. Lett. **76**, 4508 (1996).

[85] S. R. Wilkinson, C. F. Bharucha, K. W. Madison, Qian Niu, and M. G. Raizen, Phy. Rev. Lett. **76**, 4512 (1996).

[86] M.-O. Mewes, *et al.*, Phy. Rev. Lett. **77**, 416 (1996).

[87] S. Inouye, M. R. Andrews, J. Stenger, H.-J. Miesner, D. M. Stamper-Kurn, and W. Ketterle, *submitted*.

[88] V. M. Pérez-García, H. Michinel, and H. Herrero, quant-ph/9803038

[89] P. A. Ruprecht, M. J. Holland, K. Burnett, and M. Edwards, Phys. Rev. A **51**, 4704 (1995).

[90] A. Smerzi and S. Fantoni, Phy. Rev. Lett. **78**, 3589 (1997)

[91] M. Edwards and K. Burnett, Phy. Rev. A **51**, 1382 (1995).

[92] M. Edwards, *et al.*, Phy. Rev. A **53**, R1950 (1996).

[93] M. Edwards, *et al.*, Phy. Rev. Lett. **77**, 1671 (1996).

[94] S. Stringari, Phy. Rev. Lett. **77**, 2360 (1996).

[95] K. G. Singh and D. S. Rokhsar, Phy. Rev. Lett. **77**, 1667 (1996).

[96] V. L. Ginzburg and L. P. Pitaevskii, Zh. Eksp. Teor. Fiz. **34**, 1240 (1958).

[97] E. P. Gross, J. Math. Phys. **4**, 195 (1963).

[98] C. Zener, Proc. R. Soc. London A **137**, 696 (1932).

[99] E. A. Burt, *et al.*, Phy. Rev. Lett. **79**, 337 (1997).

[100] J. M. Vogels, *et al.*, Phy. Rev. A **56**, R1067 (1997).

[101] Ph. Courteille, R. S. Freeland, D. J. Heinzen, F. A. van Abeelen, and B. J. Verhaar, *submitted*.

[102] B. P. Anderson and M. A. Kasevich, Private communication (1998).

[103] D.-I. Choi, W. Chism, and L. E. Reichl, in preparation.

[104] *Atoms in Intense Laser Fields*, edited by M. Gavrila (Academic Press, 1992); K.Burnett, V. C. Reed, and P. L. Knight, J.Phys.B **26**, 561 (1993); M. Protopapas, C. H. Keitel, and P. L. Knight, Rep. Prog. Phys. **60**, 389 (1997).

[105] J. Gersten and M. H. Mittleman, J. Phys. B **9**, 2561 (1976).

[106] M. Pont, N. R. Walet, M. Gavrila, and C. W. McCurdy, Phys. Rev. Lett. **61**, 939 (1988).

[107] M. Pont and M. Gavrila, Phys. Rev. Lett. **65**, 2362 (1990).

[108] K. C. Kulander, K. J. Schafer, and J. L. Krause, Phys. Rev. Lett. **66**, 2601 (1991).

[109] K. C. Kulander, Phys. Rev. A **35**, 445 (1987).

[110] M. Dörr, *et al*, Phys. Rev. A **43**, 3729 (1991).

[111] R. Grobe and C. K. Law, Phys. Rev. A **44**, R4114 (1991).

[112] R. J. Vos and M. Gavrila, Phys. Rev. Lett. **68**, 170 (1992).

[113] M. P. de Boer, *et al*, Phys. Rev. Lett. **71**, 3263 (1993).

[114] M. P. de Boer, *et al*, Phys. Rev. A **50**, 4085 (1994).

[115] N. J. van Druten, *et al*, Phys. Rev. A **55**, 622 (1997).

[116] J. Javanainen, J. H. Eberly, and Q. Su, Phys. Rev. A **38**, 3430 (1988); Q. Su and J. H. Eberly, Phys. Rev. A **43**, 2474 (1991).

[117] M. Protopapas, D. G. Lappas, and P. L. Knight, Phys. Rev. Lett. **79**, 4550 (1997).

[118] R. L. Guenther, Ph.D. dissertation, University of Texas at Austin (1995).

[119] B. Sundaram and R. V. Jensen, Phys. Rev. A **47**, 1415 (1993).

[120] A. Patel, M. Protopapas, D. G. Lappas, and P. L. Knight, Phys. Rev. Lett. Submitted for publication.

[121] M. J. Berger and J. Oliger, J. Comput. Phys. **53**, 484 (1984).

[122] All testings reported in this thesis were carried out with the Binary Black Hole Grand Challenge `DAGH`(Distributed Adaptive Grid Hierarchy) package written by J. C. Browne and M. Parashar.

[123] M. J. Berger and P. Colella, J. Comput. Phys. **82**, 64 (1989).

[124] M. W. Choptuik, Personal communication (1998).

[125] L. F. Richardson, Phil. Trans. Roy. Soc. **210**, 307-357 (1910).

[126] M. W. Choptuik, Unpublished notes, (1995).

[127] D.-I. Choi, Unpublished notes, (1996).

[128] M. Parashar and M. F. Huq, Unpublished notes, (1996).

[129] M. J. Berger and I. Rigoutsos, IEEE Trans. on Systems, Man, and Cybernetics, **21**, 1278 (1991).

[130] D. Ballard and C. Brown, *Computer Vision*, Englewood Cliffs, NJ: Prentice Hall (1982).

[131] D. Marr and and E. Hildreth, "Theory of edge detection", Proc. Royal Soc. London, **207** (1980).

[132] R. L. Guenther, Private codes (1995).

[133] P. Walker, Private codes (1996).

[134] D.-I. Choi, Unpublished notes, (1996).

[135] Modules written by Matt Choptuik for a visualization software Silicon Graphics Inc. `IRIX Explorer`.

[136] The `PARAMESH` package supported by the NASA HPCC Program has been developed by Peter MacNeice, Kevin Olson, Clark Mobarry, Rosalinda de Fainchtein and Charles Packer.

Vita

Dae-Il Choi, the son of Moonhee Chung and Myung Choi, was born in Seoul, Korea on February 23rd, 1970. After graduating from Kyunggi High School of Science in Suwon, Korea in 1988, he entered the Korea Advanced Institute of Science and Technology to study physics. He received a Bachelor of Science in Physics in August of 1992. In September of 1992, he entered The Graduate School at The University of Texas at Austin. He has accepted a Postdoctoral research position in the Department of Physics and Atmospheric Sciences at Drexel University in Philadelphia, PA. This position begins in September 1999.

Permanent address: 113-305 Kubanpo Apt.
                               Banpobondong, Suchogu
                               Seoul, Korea 137-049

This dissertation was typeset with LaTeX[‡] by the author.

[‡]LaTeX is a document preparation system developed by Leslie Lamport as a special version of Donald Knuth's TeX Program.